

Understanding of Corrosion Phenomena: Process, Mechanism, and Method

Guest Editors: Rokuro Nishimura, Tooru Tsuru, Toshiaki Ohtsuka,
Nobuyoshi Hara, En-Hou Han, and Osama Alyousif





Understanding of Corrosion Phenomena: Process, Mechanism, and Method

**Understanding of Corrosion Phenomena:
Process, Mechanism, and Method**

Guest Editors: Rokuro Nishimura, Tooru Tsuru,
Toshiaki Ohtsuka, Nobuyoshi Hara, En-Hou Han,
and Osama Alyousif



Copyright © 2012 Hindawi Publishing Corporation. All rights reserved.

This is a special issue published in "International Journal of Corrosion." All articles are open access articles distributed under the Creative Commons Attribution License, which permits unrestricted use, distribution, and reproduction in any medium, provided the original work is properly cited.

Editorial Board

Raman Singh, Australia
Carmen Andrade, Spain
Ksenija Babic, USA
José Maria Bastidas, Spain
Pier Luigi Bonora, Italy
Marek Danielewski, Poland
Flavio Deflorian, Italy
Omar S. Es-Said, USA
Sebastian Feliu, Spain
Wei Gao, New Zealand

Karl Ulrich Kainer, Germany
W. Ke, China
H. K. Kwon, Japan
Dongyang Y. Li, Canada
Chang-Jian Lin, China
Efsthios I. Meletis, USA
Vesna Mišković-Stanković, Serbia
Rokuro Nishimura, Japan
Michael I. Ojovan, UK
F. J. M. Pérez, Spain

Ramana M. Pidaparti, USA
Willem J. Quadackers, Germany
Aravamudhan Raman, USA
Michael J. Schütze, Germany
Ramazan Solmaz, Turkey
Yanjing Su, China
Jerzy A. Szpunar, Canada
Yu Zuo, China

Contents

Understanding of Corrosion Phenomena: Process, Mechanism, and Method, Rokuro Nishimura, Tooru Tsuru, Toshiaki Ohtsuka, Nobuyoshi Hara, En-Hou Han, and Osama Alyousif
Volume 2012, Article ID 286174, 2 pages

Environmental and Material Influences on the Stress-Corrosion Cracking of Steel in H₂O–CO–CO₂ Solutions, J. W. van der Merwe
Volume 2012, Article ID 414156, 13 pages

The Effect of Applied Stress on Environment-Induced Cracking of Aluminum Alloy 5052-H3 in 0.5 M NaCl Solution, Osama M. Alyousif and Rokuro Nishimura
Volume 2012, Article ID 894875, 5 pages

Improvement of Pitting Corrosion Resistance of Type 316L Stainless Steel by Potentiostatic Removal of Surface MnS Inclusions, Nobuyoshi Hara, Koichi Hirabayashi, Yu Sugawara, and Izumi Muto
Volume 2012, Article ID 482730, 6 pages

The Corrosion Behavior of Ni₃Al/Ni₃V Two-Phase Intermetallic Compounds in Various Acidic Solutions, Gadang Priyotomo, Hideyuki Momono, Sanat Wagle, Kenji Okitsu, Akihiro Iwase, Yasuyuki Kaneno, Rokuro Nishimura, and Takayuki Takasugi
Volume 2012, Article ID 626240, 6 pages

Corrosion Protection of Steels by Conducting Polymer Coating, Toshiaki Ohtsuka
Volume 2012, Article ID 915090, 7 pages

Atomistic Modeling of Corrosion Events at the Interface between a Metal and Its Environment, Christopher D. Taylor
Volume 2012, Article ID 204640, 13 pages

Preliminary Study of Corrosion Status on Bronzes Excavated from Qin Dynasty Tombs at Xinfeng Town in China, Qian-li Fu, Pu-jun Jin, Xue Ling, Shang-xin Zhang, Wei-gang Sun, and Yin Xia
Volume 2012, Article ID 150380, 6 pages

Stress-Corrosion Cracking Property of Aluminum-Magnesium Alloy Processed by Equal-Channel Angular Pressing, Hiroaki Nakano, Satoshi Oue, Seiji Taguchi, Shigeo Kobayashi, and Zenji Horita
Volume 2012, Article ID 543212, 8 pages

Determination of Susceptibility to Intergranular Corrosion of UNS 31803 Type Duplex Stainless Steel by Electrochemical Reactivation Method, Mehmet Emin Arikan, Rafet Arikan, and Mustafa Doruk
Volume 2012, Article ID 651829, 10 pages

Corrosion Behaviour of Heat-Treated Aluminum-Magnesium Alloy in Chloride and EXCO Environments, S. O. Adeosun, O. I. Sekunowo, S. A. Balogun, and V. D. Obiekea
Volume 2012, Article ID 927380, 9 pages

Editorial

Understanding of Corrosion Phenomena: Process, Mechanism, and Method

**Rokuro Nishimura,¹ Tooru Tsuru,² Toshiaki Ohtsuka,³ Nobuyoshi Hara,⁴
En-Hou Han,⁵ and Osama Alyousif⁶**

¹ Graduate School of Engineering, Osaka Prefecture University, Sakai, Osaka 599-8531, Japan

² Graduate School of Science and Engineering, Tokyo Institute of Technology, O-okayama, Meguro-ku, Tokyo 152-8552, Japan

³ Faculty of Engineering, Hokkaido University, Hokkaido, Sapporo 060-8628, Japan

⁴ Graduate School of Engineering, Tohoku University, Aoba-ku, Miyagi, Sendai 980-8579, Japan

⁵ Institute of Metal Research, Chinese Academy of Sciences, 62 Wencui Road, Liaoning, Shenyang 110016, China

⁶ Mechanical Engineering Department, College of Engineering & Petroleum, Kuwait University, P.O. Box 5969, Safat 13060, Kuwait

Correspondence should be addressed to Rokuro Nishimura, nishimu@mtr.osakafu-u.ac.jp

Received 8 July 2012; Accepted 8 July 2012

Copyright © 2012 Rokuro Nishimura et al. This is an open access article distributed under the Creative Commons Attribution License, which permits unrestricted use, distribution, and reproduction in any medium, provided the original work is properly cited.

Corrosion phenomena of materials are very complicated in order that corrosion reactions and/or processes depend largely upon the material/environment systems. The damage of the materials caused by the corrosion phenomena has led to the loss in energy and resources, the instability of human life, the decline in the reliability of the infrastructure, and so on. To overcome them, recent advances in the understanding of corrosion phenomena and the mechanisms have been introduced for new aspects and perspective to study the roles of anion species and films formed in corrosion behavior, the factors influencing SCC (stress corrosion cracking) susceptibility, hydrogen permeation behavior associated with hydrogen embrittlement, and so on. These have led to the development of a higher corrosion resistant material, a more suitable inhibitor and corrosion prevention method, and to the reasonable judgment of the material selection in a given corrosive environment. Therefore, this special issue was focused on recent developments in stress corrosion cracking, advances in corrosion resistant materials, role of atomic hydrogen in hydrogen embrittlement, the stability and strength of the films formed, new aspects of localized corrosion (pitting corrosion and crevice corrosion), recent developments in inhibitors, new methods for elucidating corrosion behavior, and so on.

Several papers described the corrosion protection, atomic modeling of corrosion phenomena, the corrosion products exposed with the long-range term at the atmospheric

environment and the corrosion behavior of advance material (Ni-based intermetallic compound). T. Ohtsuka reviewed the corrosion protection of steels by the coating of the conducting polymers which are polyaniline, polypyrrole, and polythiophene. He described that they work as a strong oxidant, inducing the potential shift to the noble direction. C. D. Taylor reviewed and considered the atomistic modeling of corrosion events such as the metal-water interface, the reaction of water, competitive adsorption, the structure of a metallic surface, and so on. F. Q-Li et al. investigated many bronze wares of Qin Dynasty excavated from tombs at Xinfeng town using SEM/EDS, XRD and RM and obtained valuable information on the conservation of the bronze wares. S. O. Adeosun et al. investigated the corrosion behavior of as-cast and retrogressed-reaged Al-Mg alloys in solutions of NaCl, FeCl₃, and so on. They pointed out that Mg₂Si crystals being anodic relative to the matrix affected the corrosion behavior. The corrosion behavior of Ni₃Al/Ni₃V two-phase intermetallic compounds was investigated in various acidic solutions by using the immersion test and SEM by G. Priyotomo et al. They found that the preferential dissolution of (L1₂ + D0₂₂) phase took place and the corrosion behavior depended largely upon anion species.

The other papers described the localized corrosion behavior such as the intergranular corrosion, pitting corrosion and SCC. M. E. Arikian et al. determined the susceptibility to intergranular corrosion of UNS 31803-type duplex stainless

steel, which was aged at various times with 725°C, using electrochemical reactivation method and weight loss test. They found that the degree of sensitization was related to chromium- and molybdenum-depleted areas. N. Hara et al. studied the pitting corrosion resistance of 316 L-type stainless steel. They concluded that the enhancement in pitting corrosion resistance was due to the beneficial effect of removing MnS inclusions from the steel surface rather than the modification effect of the chemical composition of passive films. The SCC of A516 pressure vessel steel was investigated by slow strain rate tests in H₂O-CO-CO₂ solutions by J. W. van der Merwe. It was found that CO component played an important role in initiation of SCC, that is, the inhibition of corrosion reaction. H. Nakano et al. investigated the SCC property of Al-Mg alloy processed by equal-channel angular pressing (ECAP) by a slow strain technique in 3% NaCl of pH 4 at 303 K. They found that the decrease in the SCC susceptibility was attributed to an improvement in corrosion resistance afforded by ECAP. O. M. Alyousif et al. investigated the effect of applied stress on environment induced cracking (EIC) of Al alloy (5052) in 0.5 M NaCl solution using a constant load method. They concluded that the steady state elongation rate became a parameter for predicting time to failure and the EIC was induced by SCC, not by HE (hydrogen embrittlement).

*Rokuro Nishimura
Tooru Tsuru
Toshiaki Ohtsuka
Nobuyoshi Hara
En-Hou Han
Osama Alyousif*

Research Article

Environmental and Material Influences on the Stress-Corrosion Cracking of Steel in H₂O–CO–CO₂ Solutions

J. W. van der Merwe

School of Chemical and Metallurgical Engineering, University of the Witwatersrand, Johannesburg, Private Bag 3, Wits 2050, South Africa

Correspondence should be addressed to J. W. van der Merwe, josias.vandermerwe@wits.ac.za

Received 14 March 2012; Revised 18 April 2012; Accepted 26 April 2012

Academic Editor: Rokuro Nishimura

Copyright © 2012 J. W. van der Merwe. This is an open access article distributed under the Creative Commons Attribution License, which permits unrestricted use, distribution, and reproduction in any medium, provided the original work is properly cited.

The stress-corrosion cracking of A516 pressure vessel steel was investigated by the use of slow strain-rate tests. The orientation of samples to the rolling direction was investigated, and it was found that samples machined longitudinal to the rolling direction showed a slightly increased sensitivity to stress corrosion. The temperature variation showed that for different gas mixtures, the maximum sensitivity to stress corrosion was in the region of 45° to 55°C for the 25% CO gas mixture, whereas with higher CO concentrations, this temperature region of maximum sensitivity moved to higher temperatures. Surface finish showed a slight increase in sensitivity to cracking with increased surface roughness. The most significant increase was found with increased total gas pressures and when samples have been exposed to the environment for an extended period. This was as a result of the inhibition of the corrosion reaction by the passivation of the carbon monoxide, which is a time-dependent process.

1. Introduction

During coal gasification processes, a significant volume of water comes in contact with the combustion gas mixture, and the result of this is a contaminated, black water by-product that is transported and processed. Due to water shortages, the by-product water is used as a cooling agent. This water by-product then comes in contact with steel piping which leads to embrittlement thereof during exposure to the appropriate conditions. The water by-product consists of water with dissolved gasses mainly as carbon monoxide and carbon dioxide. Steel is susceptible to stress-corrosion cracking (SCC) in CO/CO₂/H₂O environments. Extensive research [1, 2] has indicated that SCC in this system is probably due to inhibition of iron corrosion in the H₂O–CO₂ system by the time-dependent adsorption of CO. Rupture of the inhibited passive surface by emerging slip steps then creates the highly localised active region on a passive surface necessary for the development of a sharp crack. Previous work done by various researchers [1–3] using a wide spectrum of mechanical tests and potentiodynamic polarisation has indicated that SCC of steel in this system occurs over a wide range of

CO partial pressures and temperatures which include the typical operating conditions for coal gasification plants. This indicated that high susceptibility to SCC has not always been found in the plant, from personal experience, where SCC is indeed limited to certain areas of the plant. Malik [4] performed an investigation on steel exposed to the vapour phase of H₂O–CO–CO₂ mixtures and found that in the presence of both carbon monoxide and carbon dioxide, the steel was more sensitive to cracking.

This investigation concentrated on the effect of temperature, carbon monoxide concentration, pressure, sample orientation, and surface finish on the susceptibility to cracking of carbon-manganese steels. The slow strain-rate test technique was used since it is a simple test to discriminate between environments and material conditions to reveal the relative sensitivities to cracking. With the appropriate strain rate, it is possible to induce stress-corrosion cracking. The most important characteristic of the test is the relatively slow strain rate generated at the region of crack initiation and growth. A principle advantage of the test is the rapidity with which the stress-corrosion susceptibility may be assessed. For many systems, a tensile strain rate of 10⁻⁵ to 10⁻⁶ s⁻¹

TABLE 1: The A516 pressure vessel steel composition.

Element	Al	B	C	Co	Cr	Cu	V	Mn
wt%	0.009	0.002	0.217	0.010	0.010	0.010	0.010	1.030
Element	Mo	N ₂	Nb	Ni	P	S	Ti	Si
wt%	0.010	0.007	0.004	0.020	0.009	0.003	0.001	0.290

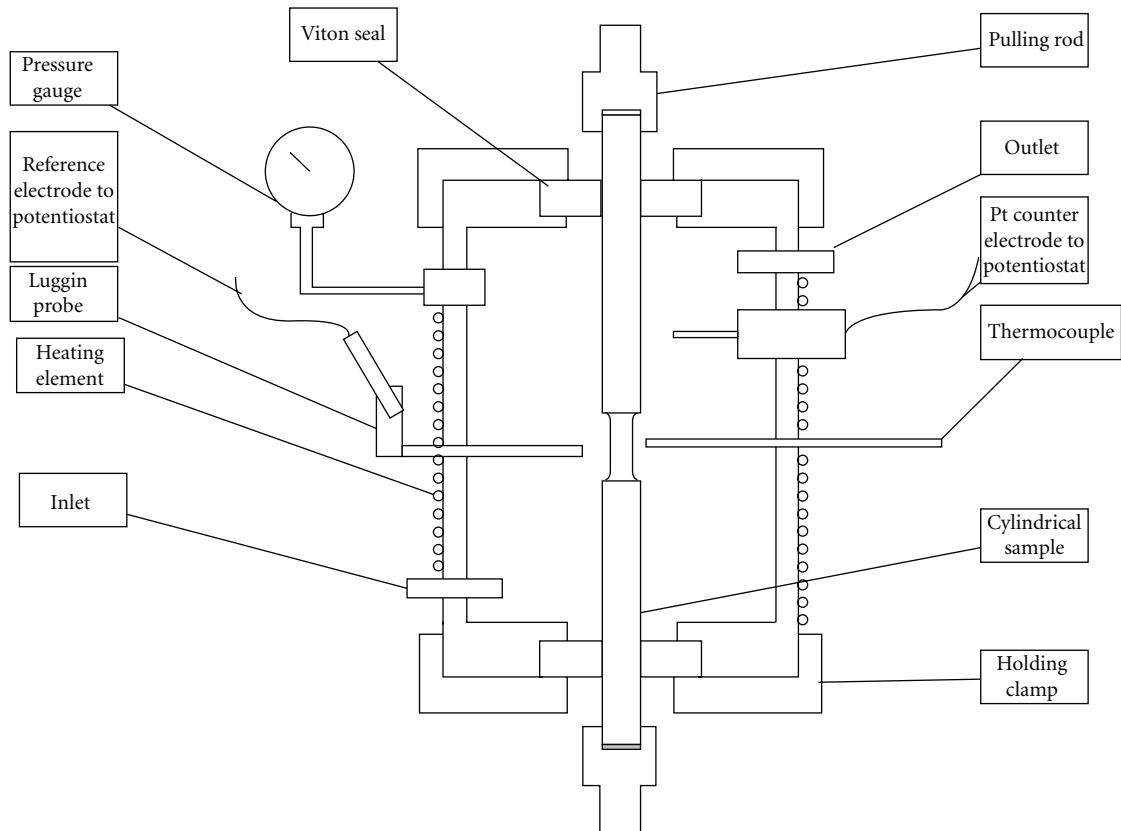


FIGURE 1: A schematic presentation of the tensile specimen in the autoclave that was used for the slow strain-rate test.

promotes cracking, but the absence of embrittlement at these rates would not be indicative of immunity to cracking if other strain rates have not been investigated. Generally, the strain rate is constant for most of the test, but as soon as the necking starts, the localised strain rate increases dramatically, and the sensitivity to cracking diminishes. However, at this stage, the cracks have formed already, and the ductile failure induced by the higher strain rates is reduced, because of the existing cracks that formed during the uniform strain-rate application. The effective strain rate once cracks have initiated cannot be measured. With the slow strain-rate test it is possible to control the rate-determining step which is the strain rate of the deforming specimen.

Comparison between identical specimens exposed to the embrittling environment and inert conditions can be used to assess the susceptibility to cracking. In this study, the parameters used were the percentage elongation, as well as the percentage reduction in area, as these are easily measured.

The stress-corrosion cracking characteristics of A516 pressure vessel steel were investigated in terms of the influence of the gas composition, rolling direction,

temperature, total gas pressure, applied electrochemical potential, time of exposure before testing, surface finish, and strain rate. The interrelationship of these factors was investigated to determine conditions of maximum susceptibility to cracking.

2. Experimental Procedure

2.1. Material. The steel used throughout the study was A516 pressure vessel steel, with the composition shown in Table 1. The composition was determined by using Leco Carbon/Sulphur Analysers, 3460 Emission Spectrometer, and 8680 + 72RET XRF Spectrometers.

Stress-corrosion cracking was evaluated by using the slow strain-rate method according to ISO 7539-7 (ASTM E8), with the initial slow strain rate being 10^{-6} s^{-1} . A schematic drawing of the test rig used is shown in Figure 1.

The environment consisted of distilled water saturated with a CO/CO₂ gas mixture. Small-sized specimens proportional to the standard specimen according to ASTM

standard E8 for cylindrical tensile test specimens were used, with a diameter of 4.0 mm and a reduced section length of 22.5 mm, slightly longer than the standard which is at 19.0 mm a schematic drawing of the tensile specimen is shown in Figure 2.

2.2. Experimental Procedure. The water-gas mixture was prepared in a stainless steel pressure vessel of approximately 160 litres. This setup was also used for the other laboratory tests performed during this study. The pressure vessel was filled with distilled water and purged with nitrogen for long enough to ensure that the dissolved oxygen concentration was below 0.1 ppm. Following the nitrogen purge, there was a purge with the appropriate gas mixture for approximately 20 minutes, and thereafter, the vessel was sealed and pressurised to the required level. Most of the experiments for the slow strain-rate tests were performed at a pressure of 800 kPa and a gas composition of 25% carbon monoxide and 75% carbon dioxide. The gas mixture was prepared beforehand by a commercial gas company according to the required concentrations.

The prepared solution was then transferred to the cell with the slow strain-rate tensile specimen as shown in Figure 1. The solution was allowed to flow through this unit to ensure that the same conditions were achieved in the environment of the tensile specimen. The temperature was measured with a K-type thermocouple that was introduced into the autoclave with a Swagelok fitting, and the temperature was controlled by a temperature controller that regulated a heating element which was wrapped around the autoclave. The pressure in the slow strain-rate autoclave was measured with a pressure gauge that was also introduced into the autoclave with a 1/8" stainless steel tube and Swagelok fitting. Two Viton seals were used to seal and insulate tensile specimen from the autoclave. The autoclave was manufactured from stainless steel which would have shown insignificant corrosion with very little contamination. Each tensile specimen was further insulated from the testing rig at the pulling rod ends, to ensure that no galvanic cell was formed between the stainless steel autoclave and the carbon steel specimen.

With most of the tests, unless otherwise noted, the specimen was installed in the autoclave, after which the autoclave was filled with the solution, and the test was started shortly afterwards. The tensile specimen was also slightly prestressed to ensure that no time was wasted during the tensioning of the frame and pulling rods, since the strain-rate was low and this would have increased the duration of the test considerably.

The specimen was measured beforehand with a vernier calliper in terms of its gauge length and original diameter. The accuracy of these measurements was to the nearest 0.1 mm, according to the accuracy of the vernier calliper. The gauge length measurements were made from shoulder to shoulder on the tensile specimen, which included the radii where no elongation would be expected, but these positions were the best defined and consistent on all the specimens. The original and final diameters were measured, and the final

diameter, after the test, was measured by carefully rejoining the two fractured pieces. This measurement was difficult and the accuracy disputable with a definite higher margin of error.

3. Results

The results from the slow strain-rate tests for samples machined parallel to the rolling direction are shown in Table 2. Here, the lengths of the two fractured sections were given as l_1 and l_2 ; therefore, l_f the final length of the specimen, was

$$l_{\text{final}} = l_1 + l_2. \quad (1)$$

The elongation of the specimen was calculated as follows:

$$\text{Elongation} = \frac{l_{\text{final}} - l_0}{l_0} \times 100, \quad (2)$$

where l_0 was the original length of the specimen, measured from shoulder to shoulder. The reduction in area was given by

$$\text{Reduction in area} = \frac{d_0^2 - d_{\text{final}}^2}{d_0^2} \times 100, \quad (3)$$

where d_0 was the original diameter, and d_{final} was the final diameter of the gauge length of the sample. Table 3 gives the results of the samples tested perpendicular to the rolling direction. These results are further presented in Figure 3 to Figure 7. Figures 3 and 4 show the influence of the orientation of the specimens to the rolling direction of the plate, as well as the environment temperature in terms of the reduction in area and elongation, respectively. The stress-corrosion cracking susceptibility was demonstrated by the loss in the reduction in area, as well as elongation. The errors were calculated by considering the accuracy of the measuring equipment, and especially on the reduction in area the error was more significant. These results did not show considerable repeatability; however, the reason for this was established during the course of the investigation. The influence of rolling direction on the susceptibility to cracking was not significant, and it would appear that stress-corrosion was affected to a greater extent by the environmental parameters, such as temperature, rather than material parameters.

Figure 5 illustrates the influence of the total pressure of the medium on the susceptibility to cracking in terms of the elongation and reduction in area. These results were for samples machined parallel to the rolling direction at a temperature of 45°C.

The effect of the total gas pressure on the cracking sensitivity exposed to a 25% carbon monoxide environment is shown in Figures 5 and 6. From these two figures, it appears that the increase in pressure has a significant effect on the crack sensitivity; with higher overall gas pressures the steel becomes more embrittled than for similar conditions at lower pressures. In Figure 5, it is shown that at 20°C an increase in the total gas pressure causes a drop in the reduction in area measured on the samples. When the

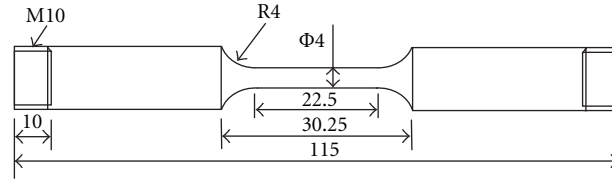


FIGURE 2: The configuration of the tensile specimen used.

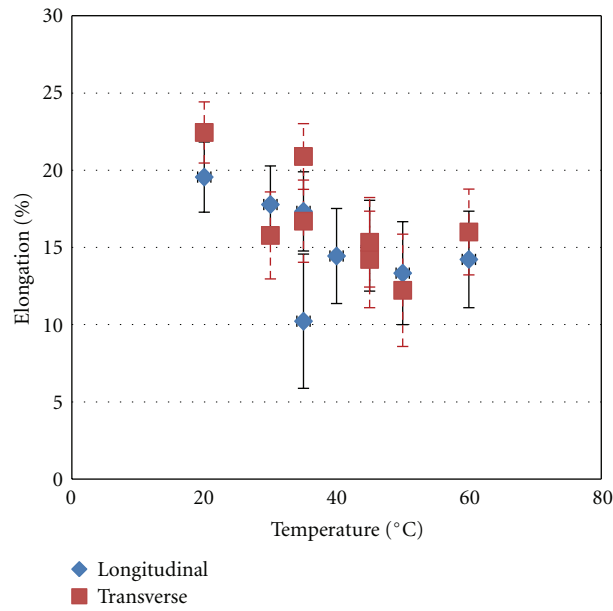


FIGURE 3: Elongation as a function of temperature for specimens machined longitudinal and transverse to the rolling direction, at 800 kPa with a gas mixture of 25% CO and 75% CO₂.

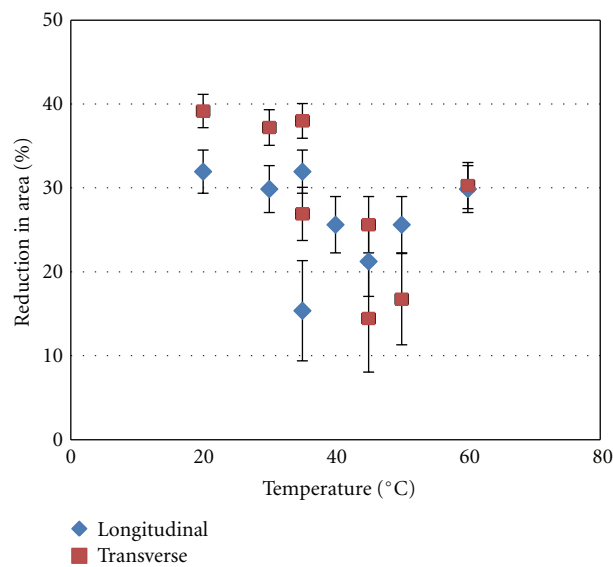


FIGURE 4: Reduction in area as a function of temperature for specimens machined longitudinal and transverse to the rolling direction, at 800 kPa with a gas mixture of 25% CO and 75% CO₂.

TABLE 2: Temperature-dependent results of samples machined parallel to the rolling direction.

Sample	Temperature (°C)	Total pressure (kPa)	l_1 (mm)	l_2 (mm)	l_{final} (mm)	Elongation (%)	d_{final} (mm)	Reduction in area (%)
L1	20	350	10.3	23.7	34.0	17.8	3.05	41.8
L3	20	500	23.8	10.35	34.15	18.4	3.20	36.0
L15	20	800	14.1	20.3	34.4	19.6	3.30	31.9
L13	20	1000	23.6	10.1	33.7	16.4	3.55	21.2
L10	20	Air	11.0	25.5	36.5	28.9	2.20	69.8
L16	30	800	11.2	22.8	34.0	17.8	3.35	30.3
L7	35	800	10.2	22.1	32.3	10.2	3.68	15.6
L4	35	800	12.5	21.4	33.9	17.3	3.30	31.9
L9	40	200	23.2	11.7	34.9	21.8	3.00	43.8
L6	40	800	11.1	22.15	33.25	14.4	3.45	25.6
L8	45	800	23.2	10.2	33.4	15.1	3.55	21.2
L14	50	800	20.5	12.5	32.0	13.5	3.45	25.6
L17	60	800	24.7	8.5	33.2	14.4	3.35	29.4

* This total length includes the shoulders of the specimen and does not refer to the gauge length.

TABLE 3: Temperature-dependent results of samples machined perpendicular to the rolling direction.

Sample	Temperature (°C)	Total pressure (kPa)	l_1 (mm)	l_2 (mm)	l_{total} (mm)	Elongation (%)	d_{final} (mm)	Reduction in area (%)
K7	20	800	24.55	10.50	35.05	22.4	3.12	39.2
K4	20	1000	15.10	20.00	35.10	22.7	3.1	39.9
K9	30	800	23.15	10.40	33.55	15.8	3.17	37.2
K2	35	800	17.20	17.50	34.70	20.8	3.15	38.0
K6	35	1000	15.50	18.25	33.75	16.7	3.42	26.9
K1	45	1000	20.55	12.45	33.0	13.3	3.55	21.2
K5	45	800	15.70	17.50	33.20	14.2	3.7	14.4
K8	50	800	24.95	7.80	32.75	12.2	3.65	16.7
K11	60	1000	24.40	9.20	33.6	16.0	3.34	30.3

influence of the total gas pressure was evaluated at various temperatures, as shown in Figure 6, the effect of the total gas pressure was not as significant.

The influence of the temperature on transverse samples exposed to 50% carbon monoxide and 50% carbon dioxide was investigated, and the detailed results are shown in Table 4. The tests were performed at 800 kPa.

The test results shown in Table 4 were similar to the results of the tests performed in 25% CO and 75% CO₂, where there existed a range of greater stress-corrosion susceptibility for the intermediate temperatures, such as from 40°C to 60°C.

Figure 7 shows the reduction in area as well as the elongation for samples that were tested in 50% carbon monoxide and 50% carbon dioxide evaluated over a range of temperatures, between 20°C and 80°C.

The test results are compared later in Figure 8 for the two gas compositions evaluated, namely, 25% and 50% carbon monoxide; the maximum sensitivity increased to higher temperature for the 50% carbon monoxide.

The electrochemical potential dependence was investigated by using a *Voltamograph* CV-27 potentiostat to keep the sample at a certain potential for the whole duration of

the slow strain-rate test. These tests were performed at 45°C, 800 kPa, and a carbon monoxide concentration of 25% and 75% carbon dioxide. The potential was measured with an Ag/AgCl reference electrode that was introduced into the autoclave by a Luggin probe. The results are shown in Table 5, where the embrittling factor is plotted as a function of the applied electrochemical potential in terms of the Ag/AgCl reference electrode.

The results shown above in Table 5 are illustrated in Figures 9 and 10, demonstrating the effect of applied potential on elongation and reduction in area, respectively.

From both figures, it is clear that at a particular applied potential range, the cracking sensitivity of the steel was more enhanced.

The effect of surface roughness was investigated when scanning electron micrographs showed crack initiation on grinding marks as seen in Figures 11 and 12. Here, the cracks formed on what seems to be a 45° angle, which turned out to be the grinding angle for the specific sample. Slow strain-rate tests were performed on samples with different surface finishes. Grinding papers with the following ISO/FEPA grit designation grit sizes: P180, P200, P400, P600, P800, and P1200 were used on separate samples, where the P180 is the

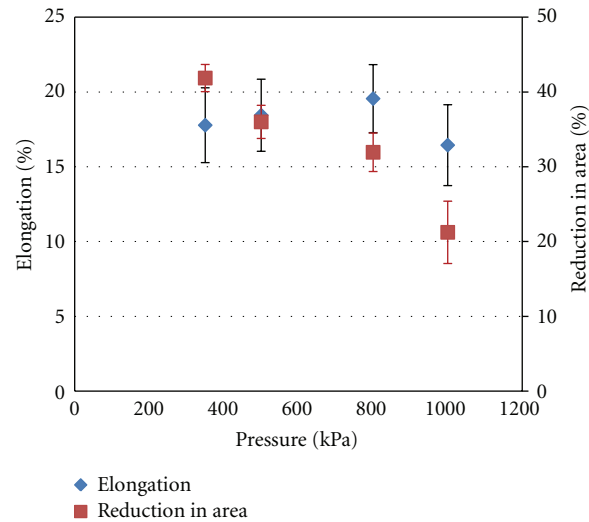


FIGURE 5: Reduction in area and elongation as a function of pressure of slow strain-rate tests performed at 20°C with a gas mixture of 25% CO and 75% CO₂.

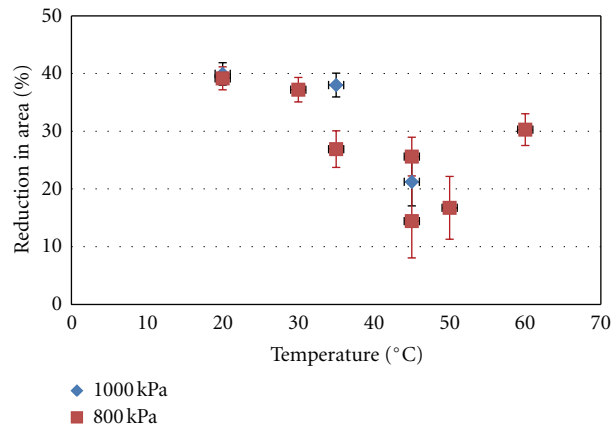


FIGURE 6: Comparison of two pressures over a temperature range with regard to reduction in area for a 25% CO and 75% CO₂ gas mixture.

roughest and P1200 is the smoothest paper, and the average particle diameters are approximately 82, 75, 35, 26, 22, and 15 μm . Table 6 shows the results of these tests performed on samples exposed to 25% carbon monoxide and 75% carbon dioxide, at 45°C and 800 kPa. Figures 13 and 14 show the results of the slow strain-rate tests in terms of the reduction in area and elongation; here, it can be seen that elongation did not show a marked difference in the influence of the machining marks on the surface of the samples. However, on the reduction in area results, a decrease was found, a greater susceptibility, with increasing surface roughness. This trend is slightly masked by scatter in the results.

The time of exposure of the specimen to the solution before test was started was investigated when it accidentally became evident that a specimen showed increased brittleness when the test was not performed immediately. In Figure 15, the embrittling factor index is plotted against the time of exposure prior to testing. For these exposure tests, the experimental parameters were a total gas pressure of 800 kPa, a temperature of 45°C, and a strain rate of 10^{-6} s^{-1} . Here, the time of exposure before the test had a significant effect on

the embrittling of the sample, which is unexpected, especially considering the degree of embrittling that was found. The embrittling indices for reduction in area and elongation both dropped in the order of 50% when the samples were not exposed to the environment before the test, and when the samples were exposed for 48 hours before testing. This trend was confirmed by the intermediate sample that was only exposed for 24 hours.

The influence of the strain-rate was investigated and in Figure 16 the embrittling factor index is plotted as a function of the strain rate. These tests were also performed at 45°C, 800 kPa, and 25% CO–75% CO₂. The strain-rate varied from 10^{-5} s^{-1} down to 10^{-8} s^{-1} unfortunately only one test was performed at 10^{-8} s^{-1} . The reduction in area index for embrittling increased from 0.2% to 0.4% when the strain rate decreased from 10^{-7} s^{-1} to 10^{-8} s^{-1} , and the same trend was seen on the elongation of the samples it went from slightly above 0.2 to 0.7 when the strain rate was decreased.

In Figure 17 the fracture surface of a specimen tested at 45°C and 800 kPa indicated the typical transgranular cleavage cracking for these tests. Some pearlite colonies are

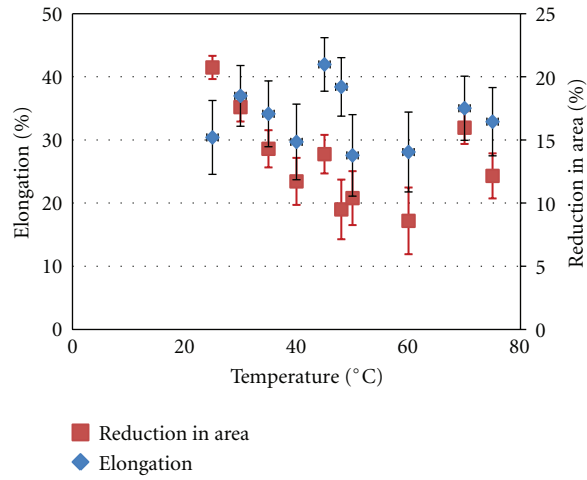


FIGURE 7: Elongation and reduction in area as a function of temperature for specimens machined transverse to the rolling direction, at 800 kPa with a gas mixture of 50% CO and 50% CO₂.

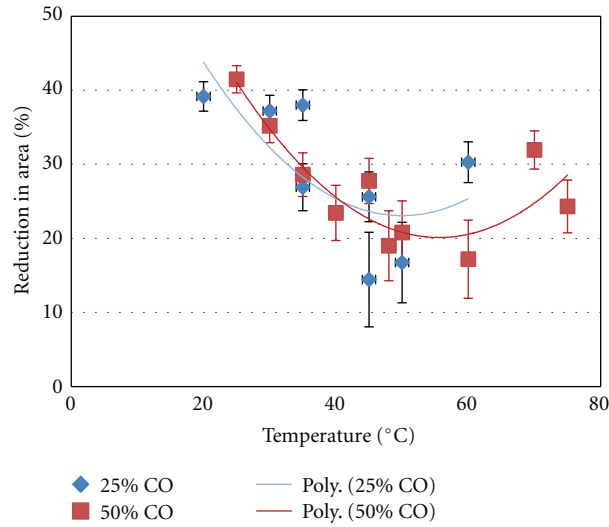


FIGURE 8: Comparison of results with two different gas mixtures, 25% CO and the other 50% CO.

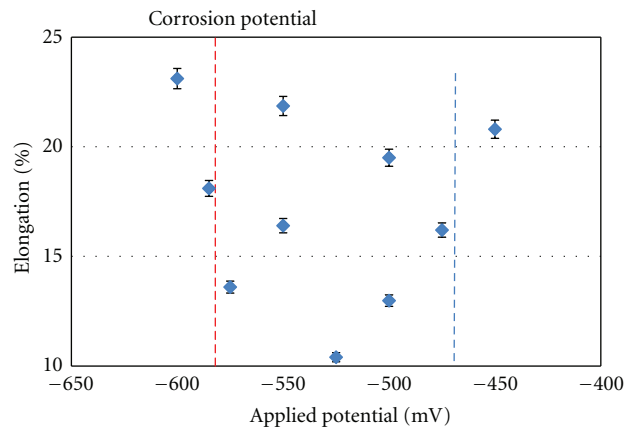


FIGURE 9: Elongation as a function of the applied electrochemical potential at 800 kPa and 45°C with a gas mixture of 25% CO and 75% CO.

TABLE 4: Temperature-dependent results of samples machined perpendicular to the rolling direction and tested in 50% CO–50% CO₂.

Temperature (°C)	l_1 (mm)	l_2 (mm)	l_{total} (mm)	Elongation (%)	d_{final} (mm)	Reduction in area(%)
25	8.18	25.24	33.42	15	3.06	41
30	10.90	23.26	34.16	18	3.22	35
35	7.84	26.00	33.84	17	3.38	29
40	14.82	18.52	33.34	15	3.50	23
45	13.80	20.92	34.72	21	3.40	28
48	12.42	21.90	34.32	19	3.60	19
50	20.92	12.18	33.10	14	3.56	21
60	12.16	21.00	33.16	14	3.64	17
70	8.94	25.00	33.94	18	3.30	32
75	19.50	14.20	33.70	16	3.48	24

TABLE 5: Potential-dependent results of samples tested in 25% CO–75% CO₂ at 45°C.

Potential (mV)	l_1 (mm)	l_2 (mm)	l_{final} (mm)	Elongation (%)	d_{final} (mm)	Reduction in area (%)
–600	8.9	26.3	35.2	23.11	3.05	41.85
–585	13.2	20.9	34.1	18.1	3.34	30.27
–575	17.8	15.3	33.1	13.6	3.64	17.19
–550	15.8	17.9	33.7	16.4	3.56	21.68
–550	8.0	26.9	34.9	21.86	3.19	36.4
–525	12.9	19.45	32.35	10.4	3.45	25.6
–500	24.9	8.0	32.9	12.98	3.57	20.34
–500	26.15	8.2	34.35	19.5	3.05	41.86
–475	10.95	22.7	33.65	16.2	3.16	37.59
–450	23.8	10.8	34.6	20.8	2.9	47.43

TABLE 6: Results of the slow strain-rate tests performed at 45°C, total pressure of 800 kPa, and 25% CO for different surface finishes.

Sample	Grit finish	Elongation	Reduction in area
L52	P1200	24.0	41.9
L70	P1200	21.7	31.9
L68	P800	22.1	38.4
L59	P600	26.1	36.0
L57	P400	22.8	34.4
L67	P400	16.0	26.0
L63	P220	22.2	31.9
L66	P180	26.2	31.9

seen as the crack propagated through the colony and was possibly etched by the environment. A cross section was also made to show the transgranular nature.

A test was performed in 100% CO, 800 kPa, at a strain rate of 10^{-7} s^{-1} and 45°C. These specimens did show cracking with the elongation at 21.8%.

4. Summary of Results

Here the results of the material and surface characteristics are compared with the environmental influences on the susceptibility of the steel to stress-corrosion cracking.

4.1. Rolling Direction. The results in Figure 4 did not show a significant difference between the two orientations of testing specimens being aligned parallel or perpendicular to the rolling direction, although it did appear that the samples machined longitudinal to the rolling direction showed a slightly higher susceptibility to stress corrosion. At the lower temperature range the samples longitudinal to the rolling direction showed a definitely higher susceptibility. However, at the higher temperatures, between 50°C to 60°C the difference was negligible and in some instances the opposite to the lower temperatures. From both the elongation and reduction in area data, a similar tendency was found.

4.2. Total Pressure. The results in Figure 6 show that according to the % reduction in area, higher pressures increase the susceptibility to stress-corrosion cracking. However, this is in the range of 200 to 1000 kPa. According to the % elongation a similar trend is followed with a slight increase at 800 kPa. It is also seen (Figures 4 and 5) that with an increase in the temperature, the effect of the total pressure is even greater, although this was based on two samples, and more information is needed for statistical certainty. These results are similar to those of Hannah et al. [3] where the reduction in area of the samples decreased with increasing pressures.

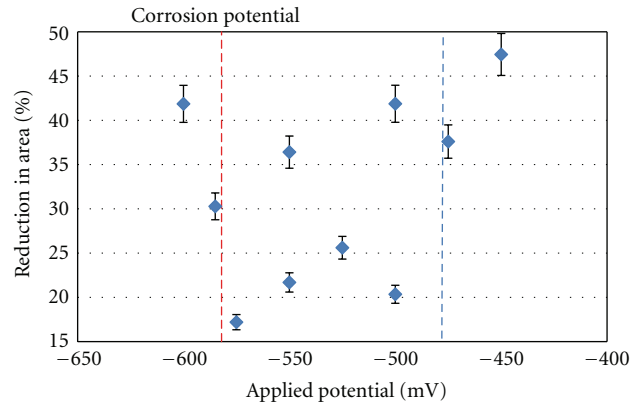


FIGURE 10: Reduction in area as a function of the applied electrochemical potential at 800 kPa and 45°C with a gas mixture of 25% CO and 75% CO₂.

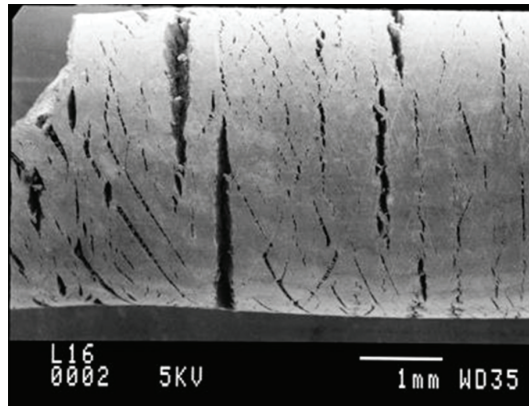


FIGURE 11: The influence of grinding marks on crack initiation for a slow strain-rate sample tested at 45°C and 800 kPa 25% CO–75% CO₂.

4.3. Gas Composition. It is clear that at higher carbon monoxide concentrations, the susceptibility to cracking increases dramatically.

4.4. Temperature. The influence of temperature was examined for two situations, samples parallel and perpendicular to the rolling direction.

4.4.1. Samples Perpendicular to the Rolling Direction. When looking at the reduction in area, these samples show a minimum resistance to stress corrosion in the order of 45°C to 55°C. This means that there is an increase in both sides—the region close to room temperature as well as higher temperatures. The increase in the resistance to stress-corrosion cracking at higher temperatures (60°C) was expected with the lower solubility of gases at the higher temperatures.

4.4.2. Samples Parallel to the Rolling Direction. The results show that a similar tendency in sensitivity to temperature for both the samples machined perpendicularly and parallel to the rolling direction. The reduction in area decreased in the temperature range 40°C to 50°C, and this seems to be in agreement with the work of Kowaka [1] as well as

Itoh [5], on the general trend of the effect of temperature. The elongations for these samples gave the same region of greater embrittlement. This behaviour is expected due to the influence of the temperature upon the kinetics of the corrosion reaction and the passivity of the steel. Here, decreased sensitivity to cracking is an indirect effect, due to the decreasing solubility of the carbon monoxide in water at increasing temperatures, which would affect the passivation of the steel. Schmitt and Rothmann [6] also showed a decrease in ductility of various carbon steel with the increase in temperature, from 25°C to 50°C. Although Schmitt et al. [7] found a maximum susceptibility around 40°C for 37 Mn5 steel grades loaded to 90% of yield strength at 10-bar CO₂.

4.5. Applied Electrochemical Potential. In Figure 9, the region where the testing was performed, the cracking resistance increased towards the higher and lower limits. Embrittlement was prevalent from around –575 mV to –475 mV, which is very similar to results obtained by Brown et al. [2]. The fractured specimens at the more noble potentials were characterised by general corrosion and little cracking. Towards the more active limit, hydrogen formation could have induced cracking, but here the resistance to cracking also increased, thus indicating that cracking is not enhanced

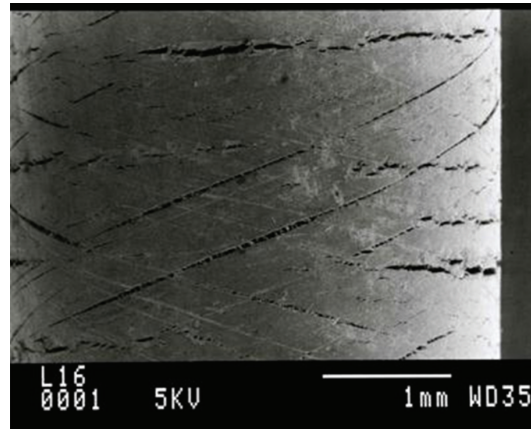


FIGURE 12: The same sample as shown above at a slightly higher magnification revealing how the cracks followed the grinding marks on the sample after a slow strain-rate test at 45°C and 800 kPa 25% CO–75% CO₂.

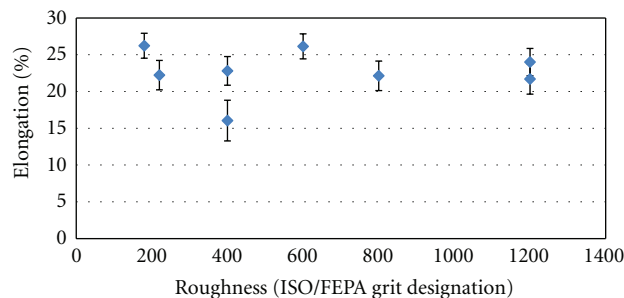


FIGURE 13: Slow strain-rate test results showing the influence of the surface roughness on the stress-corrosion resistance of steel at 45°C and 800 kPa.

by an excess of hydrogen. It could be argued that cracking could still be promoted by the presence of a small amount of hydrogen, but if this was the case, higher concentrations would have decreased the resistance to cracking. The situation is convoluted by the shifting of the corrosion potential with time, but this is evaluated in the next section.

4.6. Time of Exposure. The results in Figure 15 indicated the importance of the adsorbed CO species on the surface of the specimen and the effectiveness of this layer before the sample is stressed. Although only three samples were tested, the trend shows very clearly a greater sensitivity towards cracking. The time of exposure shows a very clear effect on the susceptibility and is a parameter that would cause significant errors if it is not kept constant during testing.

4.7. Surface Finish. The effect of the surface finish was first noted when one of the specimens was studied with the scanning electron microscope, and it was found that cracking occurred along most of the scratches left from the machining and grinding process (Figures 11 and 12). The grinding marks served as crack initiation points. This indicated the sensitivity of the cracking process to crack initiation. Although the influence of grinding grooves was not severe, there was a tendency towards a greater resistance to cracking when the surfaces had finer grinding grooves.

Therefore, it would seem that the crack initiation was more probable with the larger grooves and might be one of the reasons why cracking would occur in one area and not another. The grooving is expected to be similar on the surface, although it is possible that larger grooves remained from previously applied, coarser grinding papers.

4.8. Strain Rate. Strain rate is a very important variable and this was evaluated to a greater extent with other test methods. However, as shown by Kim and Wilde [8], with slow strain-rate testing, it is possible to differentiate between the hydrogen-induced cracking and stress-corrosion cracking. This is because of the repassivation reaction of the steel that prevents the corrosion reaction of the bare steel, since the repassivation occurs at a faster rate than the exposure of the steel due to the slip step emergence. From the results, it is clear that the minimum resistance to cracking is in the order of 10^{-7} s^{-1} . The resistance to cracking increased at 10^{-8} s^{-1} , which means that the passivation rate at the crack tip could keep up with the bare surface that is formed due to the crack tip strain rate. This is an important result that indicates that the cracking is dependent upon the passivation of the steel, and again not the hydrogen embrittlement. Therefore, if the passivation of the steel can be influenced, either by enhancing or breaking it down, the stress-corrosion cracking can be mitigated. Unfortunately, the test at 10^{-8} s^{-1} strain rate was

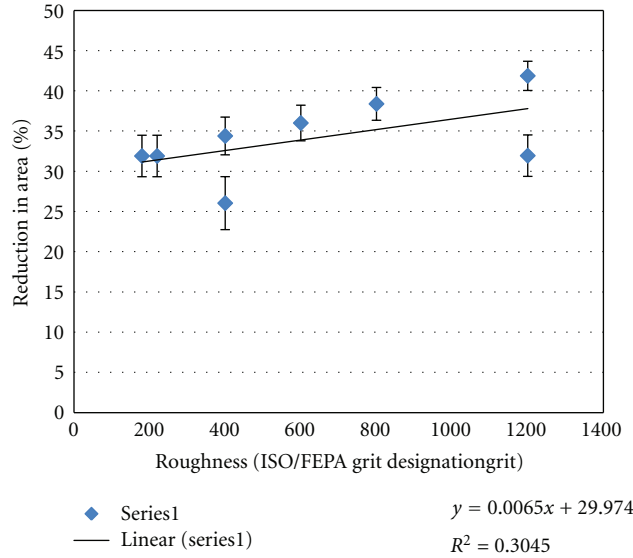


FIGURE 14: Slow strain-rate test results showing the influence of the surface roughness on the stress-corrosion resistance of steel at 45°C and 800 kPa.

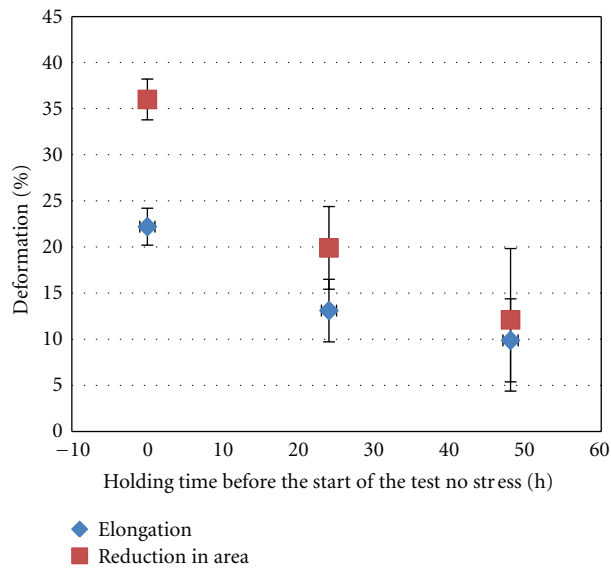


FIGURE 15: The embrittlement of the steel as a function of the time of exposure prior to testing at 45°C and 800 kPa.

performed over a very long period, and only one of these tests was performed; therefore, this is not completely conclusive evidence but suggests that strain rate is a very important component in the cracking process.

5. Discussion

Stress-corrosion cracking of steel exposed to CO–CO₂–H₂O appears to be very dependent upon the carbon monoxide adsorption on the steel surface. With the increase of temperature, the solubility of both carbon monoxide and carbon dioxide decreases and therefore, decreasing sensitivity to cracking was found at higher temperatures. A similar decrease in sensitivity to cracking was found at the lower

temperatures. However, the effect of temperature was moved to higher temperatures for the higher carbon monoxide concentration, therefore indicating the importance of the higher carbon monoxide concentration. The influence of the gas is further highlighted by the effect of higher total gas pressures. Furthermore, the effect of exposure time before the test illustrates the dependence upon the adsorption of the carbon monoxide on the steel interface. This time-dependent adsorption was demonstrated by Heaver [9], illustrating the effect of the passivation of the steel as a result of exposure time to a carbon-monoxide-containing environment. Therefore, when the time dependency of the embrittlement is considered, it has to be ascribed to the adsorption reaction of the carbon monoxide. The other

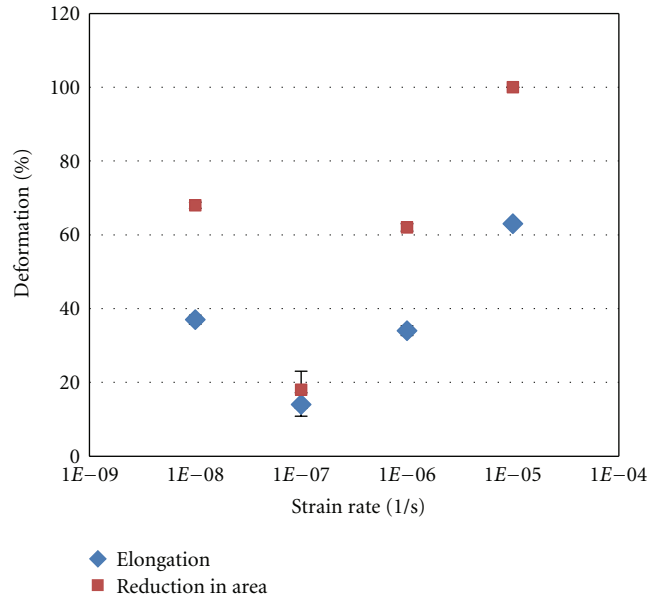


FIGURE 16: The embrittling factor index as a function of the strain rate of the slow strain-rate test at 45°C and 800 kPa.

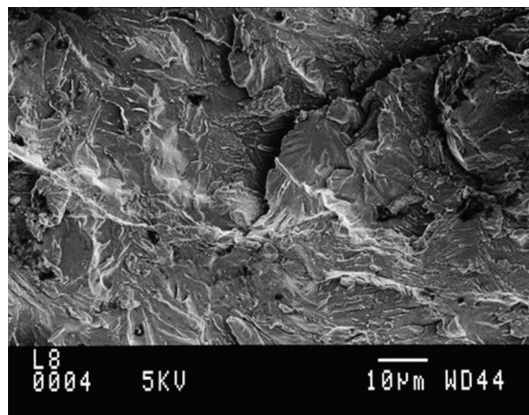


FIGURE 17: A scanning electron micrograph of the fractured surface of a slow strain-rate specimen tested in 25% CO at 45°C and 800 kPa total pressure.

parameters that were investigated did not show similar significant embrittling effects. The orientation of the samples and grinding marks on the surface of the samples both did not have a very significant effect, although these parameters showed some contribution to cracking. However, applied potential showed a significant effect on cracking with a definite potential range where cracking was enhanced. The minimum potential to this crack sensitive range corresponded to the corrosion potential and shows insensitivity towards hydrogen charging, whereas the maximum probably corresponded to the transpassive potential. This confirms the importance of the passivation and the passivation kinetics on the crack propagation.

6. Conclusions

- (1) An increase in the total pressure of the gas increases the susceptibility of the steel to stress-corrosion cracking.
- (2) Samples machined longitudinal to the rolling direction showed a slightly increased sensitivity to stress corrosion as compared to those machined transverse to the rolling direction.
- (3) Maximum susceptibility to stress-corrosion cracking is between 40°C and 50°C.
- (4) Cracking is dependent on the electrochemical potential, and cracking decreases on the cathodic side of the polarisation diagram.
- (5) A waiting time before the test is started reduces the resistance to cracking.
- (6) The surface finish does not have a large effect on the cracking resistance, although with a finer finish, the cracking is less.
- (7) Strain-rate dependence shows a maximum susceptibility at around 10^{-7} s^{-1} .

Acknowledgments

The author would like to acknowledge the guidance of Professor R. F. Sandenbergh and Professor G. T. Van Rooyen during the project.

References

- [1] M. Kowaka, *Metal Corrosion Damage and Protection Technology*, Allerton Press, 1991.
- [2] A. Brown, J. T. Harrison, and R. Wilkins, "Trans-granular stress corrosion cracking (S.C.C.) of ferritic steels," *Corrosion Science*, vol. 10, no. 7, pp. 547–548, 1970.
- [3] I. M. Hannah, R. C. Newman, and R. P. M. Procter, "Environmental cracking of C-Mn steels in aqueous CO-CO₂ environments," in *Proceedings of the 4th international conference on the effect of hydrogen on the behaviour of materials*, N. R. Moody and A. W. Thompson, Eds., p. 965, 1990.
- [4] H. Malik and F. Nawaz, "Stress corrosion cracking and electrochemistry of C-Mn steels in CO-CO₂-H₂O environments," *Anti-Corrosion Methods and Materials*, vol. 52, no. 5, pp. 259–265, 2005.
- [5] G. Itoh, Ko-atsu gas, *Journal of the High Pressure Gas Safety Institute of Japan*, vol. 14, p. 19, 1977.
- [6] G. Schmitt and B. Rothmann, "Corrosion of unalloyed and low alloyed steels in carbonic acid solutions," *Werkstoffe und Korrosion*, vol. 29, no. 4, pp. 237–245, 1978.
- [7] G. Schmitt, H. Schlerkman, and Aachen, "Corrosion cracking of steel in the system CO₂/H₂O," in *Proceedings of the 8th International Congress on Metallic Corrosion*, pp. 426–431, 1981.
- [8] C. D. Kim and B. E. Wilde, "A review of constant strain-rate stress corrosion cracking test," in *Stress Corrosion Cracking The Slow Strain Rate Technique*, STP665, G. M. Ugianski and J. H. Payer, Eds., pp. 97–112, American Society for Testing and Materials, 1979.
- [9] E. E. Heaver, *Stress corrosion cracking of steels in industrial process environments [Ph.D. thesis]*, 1994.

Research Article

The Effect of Applied Stress on Environment-Induced Cracking of Aluminum Alloy 5052-H3 in 0.5 M NaCl Solution

Osama M. Alyousif¹ and Rokuro Nishimura²

¹Department of Mechanical Engineering, College of Engineering & Petroleum, Kuwait University, P.O. Box 5969, Safat 13060, Kuwait

²Department of Applied Materials Science, College of Engineering, Osaka Prefecture University, 1-1, Gakuen-cho, Sakai, Osaka 599-8531, Japan

Correspondence should be addressed to Osama M. Alyousif, osama.alyouisif@ku.edu.kw

Received 31 March 2012; Accepted 17 May 2012

Academic Editor: Nobuyoshi Hara

Copyright © 2012 O. M. Alyousif and R. Nishimura. This is an open access article distributed under the Creative Commons Attribution License, which permits unrestricted use, distribution, and reproduction in any medium, provided the original work is properly cited.

The environment-induced cracking (EIC) of aluminum alloy 5052-H3 was investigated as a function of applied stress and orientation (Longitudinal rolling direction—Transverse: LT and Transverse—Longitudinal rolling direction: TL) in 0.5 M sodium chloride solution (NaCl) using a constant load method. The applied stress dependence of the three parameters (*time to failure*; t_f , *steady-state elongation rate*, I_{ss} , and *transition time at which a linear increase in elongation starts to deviate*, t_{ss}) obtained from the corrosion elongation curve showed that these relationships were divided into three regions, the stress-dominated region, the EIC-dominated region, and the corrosion-dominated region. Aluminum alloy 5052-H3 with both orientations showed the same EIC behavior. The value of t_{ss}/t_f in the EIC-dominated region was almost constant with 0.57 ± 0.02 independent of applied stress and orientation. The fracture mode was transgranular for 5052-H3 with both orientations in the EIC-dominated region. The relationships between $\log I_{ss}$ and $\log t_f$ for 5052-H3 in the EIC-dominated region became a good straight line with a slope of -2 independent of orientation.

1. Introduction

The environment-induced cracking (EIC) behavior of metallic alloys in chloride and other corrosive solutions has been extensively investigated using various EIC methods [1–7], where EIC is composed of stress corrosion cracking (SCC) subjected to anodic reactions such as film formation and dissolution and hydrogen embrittlement (HE) to cathodic reactions such as hydrogen evolution. A number of theories have been developed for cracking mechanisms of aluminum alloys in chloride environments [5–9]. Suresh et al. have concluded that EIC behavior in high-strength 7075 aluminum alloy under fatigue loading is mostly governed by three mechanisms, namely, the embrittling effect by the hydrogen products of the electrochemical reactions at the crack tip, the role of microstructure and slip mode and crack closure arising from environmental and microstructural elements [8, 9].

It has been reported that the behavior of the metallic alloy can be characterized using a constant load method [10]. The

method can produce a corrosion elongation curve which can be used to obtain three parameters, namely, time to failure (t_f), steady-state elongation rate (I_{ss}), and transition time at which a linear increase in elongation starts to deviate (t_{ss}). These parameters were confirmed to be used in analyzing the failure behavior and to predict time to failure (t_f) [11, 12].

The objectives of this research work are (1) to investigate the effect of applied stress on the susceptibility of aluminum alloys to EIC, (2) to evaluate the role of orientation in alloys, and (3) to elucidate a qualitative cracking mechanism for aluminum alloys in the chloride solution.

2. Experimental

The specimens used were made out of commercial 5052-H3 aluminum alloy. The geometry for EIC experiments was as follows: the gauge length 25.6 mm, its width 5 mm, and the thickness 1 mm. The specimen geometry is shown in Figure 1. The sample orientation used for the experiments

TABLE 1: Chemical compositions (wt%) and mechanical properties of A5052-H3 aluminum alloy used.

	Cu	Si	Fe	Mn	Mg	Zn	Cr	Ti	Al	σ_{yield} (MPa)	σ_{Tensile} (MPa)
A5052-H34	0.01	0.08	0.26	<0.001	2.59	<0.001	0.17	—	Bal.	180	251

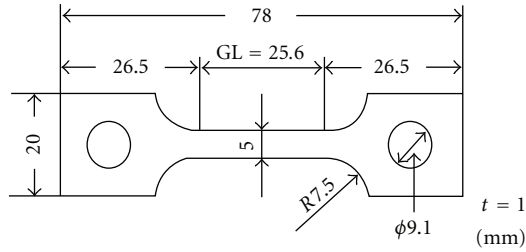
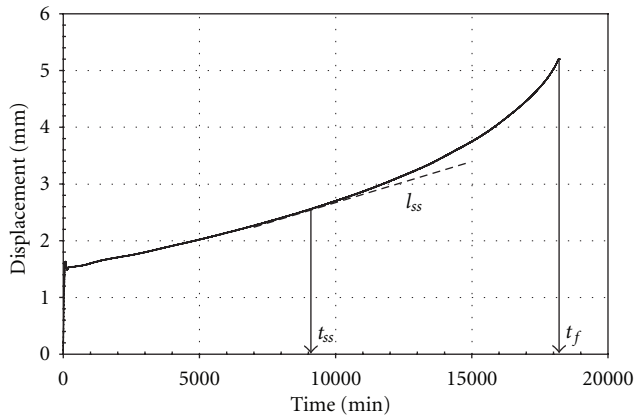


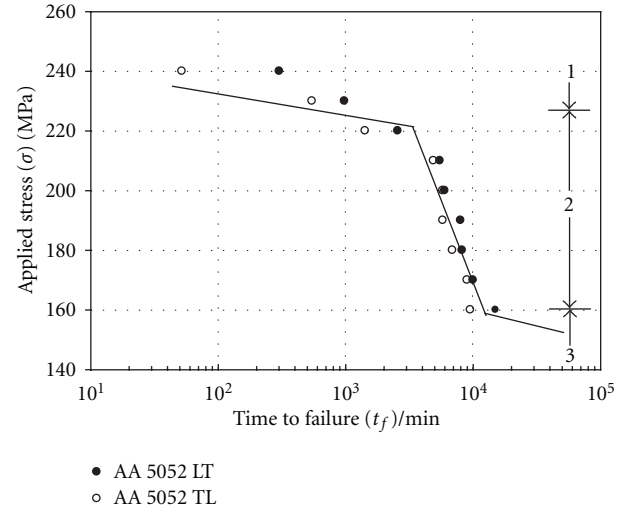
FIGURE 1: Geometry of the specimens (dimensions in mm).

FIGURE 2: The corrosion elongation curves for A5052-H3-LT at $T = 353$ K and $\sigma = 240$ MPa in 0.5 M sodium chloride solution.

was TL (Transverse—Longitudinal rolling direction) and LT (Longitudinal rolling direction—Transverse) where, in the TL orientation, the former T is the loading direction and the later L is the direction of crack growth whereas, in the LT specimens, the loading direction is in the longitudinal (L) direction and the crack growth direction is the T direction.

The chemical composition (wt%) for aluminum alloy 5052-H3 used was shown in Table 1. Prior to the experiments, the specimens were polished to 600 grit emery paper, degreased with acetone in an ultrasonic cleaner, and washed with distilled water. After the pretreatment, the specimens were immediately set into an SCC cell. The SCC tests were conducted in 0.5 M sodium chloride solutions at a test temperature of 353 K. The applied stress range for aluminum alloy 5052-H3 was from 140 MPa to 240 MPa. All experiments were carried out under an open-circuit condition.

A lever-type constant load apparatus (lever ratio 1 : 10) to which three specimens can be separately and simultaneously attached was used with a cooling system on the top to avoid evaporation of the solution during the experiments. The specimens were insulated from rod and grip by surface-oxidized zirconium tube. A change in elongation of the

FIGURE 3: The logarithm of time to failure (t_f) versus applied stress (σ) for A5052-H3 in a 0.5 M sodium chloride solution.

specimens under the constant load condition was measured by an inductive linear transducer with an accuracy of ± 0.01 mm.

3. Results

3.1. Corrosion Elongation Curve. Figure 2 shows an example of the corrosion elongation curve for 5052-H3 with the LT orientation at a test temperature of 353 K and an applied stress of 240 MPa in 0.5 M sodium chloride solution. From this curve the three parameters were obtained: time to failure (t_f), steady-state elongation rate (l_{ss}) for the straight part of the corrosion elongation curve, and transition time (t_{ss}), which is the time when the elongation curve begins to deviate from the linear increase and is indicated as t_{ss}/t_f in the paper.

3.2. Applied Stress Dependence of Three Parameters (t_f , l_{ss} , and t_{ss}/t_f). Figure 3 depicts the logarithm of time to failure (t_f) versus applied stress (σ) for 5052-H3 with the TL and LT orientations in a 0.5 M sodium chloride solution at a test temperature of 353 K. The relationships fell into three regions shown by Arabic numerals 1–3 in the figures, whereas the applied stress dependence of t_f was identical independent of the orientation. Figure 4 shows the relationship between the logarithm (l_{ss}) and applied stress (σ). The relationships were also divided into three regions with the same applied stress ranges as those in Figure 3. The value of l_{ss} in region 3 became significantly small compared to those in region 2, although this is not clear in Figure 3. Figure 5 shows the relationship between t_{ss}/t_f and σ . The value of t_{ss}/t_f was divided into three regions with the same

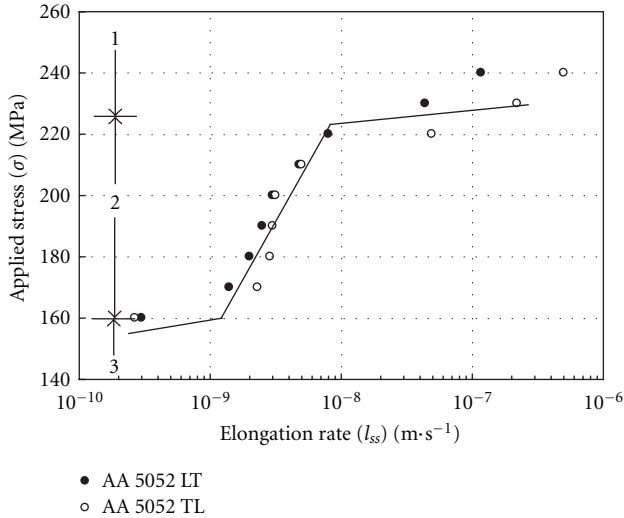


FIGURE 4: The logarithm of steady-state elongation rate (l_{ss}) versus applied stress (σ) for A5052-H3 in a 0.5 M sodium chloride solution.

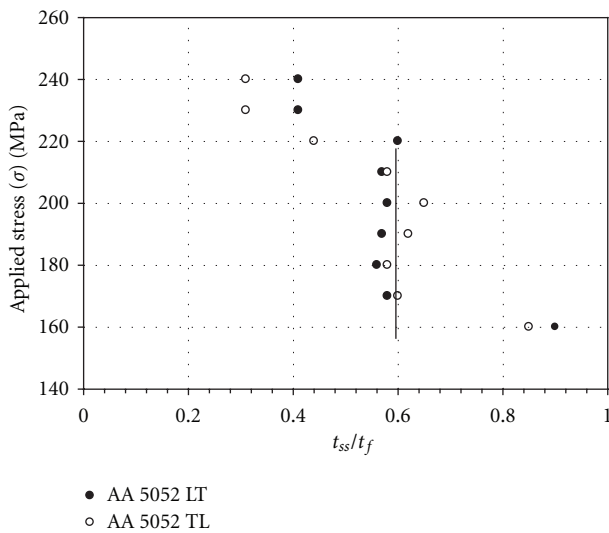


FIGURE 5: The logarithm of (t_{ss}/t_f) versus applied stress (σ) for A5052-H3 in a 0.5 M sodium chloride solution.

applied stress ranges as those in Figures 3 and 4. The value of t_{ss}/t_f in region 2 kept constant with 0.57 ± 0.02 independent of applied stress and orientation. However, that of t_{ss}/t_f in region 3 was 0.8 to 0.9 irrespective of orientation, while in region 1 it became smaller with a value of 0.3 to 0.4.

Thus, the applied stress dependences of three parameters were divided into three regions (regions 1 to 3). In region 1 t_f decreased rapidly with increasing applied stress with the rapid increase in l_{ss} . In region 2 $\log t_f$ increased and $\log l_{ss}$ decreased linearly with decreasing applied stress and in region 3 $\log t_f$ was not clear for deviation from the linear relationship in region 2, but $\log l_{ss}$ showed clearly deviation. This behavior was almost the same as those for the solution annealed and sensitized austenitic stainless steels

[13–16] and pure titanium [17]. Therefore, it was decided that region 1 was the stress-dominated, region 2 the EIC-dominated region, and region 3 the corrosion-dominated region, respectively.

3.3. Fracture Appearance. The fracture appearances of 5052-H3 with both orientations were investigated by using the scanning electron microscopy. Figure 6 shows the fracture appearance of 5052-H3 with the LT orientation in the EIC-dominated region (region 2). It was found that the fracture mode was predominantly transgranular (TG) with a dimple pattern, which was observed over the whole applied stresses in the EIC-dominated region.

4. Discussion

4.1. A Parameter for Predicting Time to Failure. Figure 7 shows the relationship between $\log t_f$ and $\log l_{ss}$ for 5052-H3 with both orientations, which was obtained by using those in Figures 3 and 4. The $\log t_f$ versus $\log l_{ss}$ curve in the EIC-dominated region for 5052-H3 became a straight line with a slope of $m = -2$ independent of orientation. Thus, we got the empirical equation as expressed in the following:

$$\log l_{ss} = -2 \log t_f + C_1, \quad (1)$$

where C_1 is a constant.

From (1), it was found that l_{ss} becomes a useful parameter for predicting t_f independent of applied stress as well as for austenitic stainless steels in hydrochloric acid and sulphuric acid solutions [8], because l_{ss} can be obtained at a time within 10–20% of t_f from the corrosion elongation curve.

4.2. A Qualitative Proposal of EIC Mechanism. In general, the fracture mode of aluminum alloys is recognized to be intergranular [18]. In 5xxx series alloys, a precipitate of Mg_2Al_3 is considered to exist along a grain boundary and to become anodic compared to grain itself [18], which may suggest that the EIC of 5052-H3 would be an intergranular stress corrosion cracking (IG-SCC). However, the present fracture mode was transgranular. This means that the precipitate would not affect the EIC behavior under the present experimental condition.

As for the EIC of the solution annealed and sensitized austenitic stainless steels in boiling saturated magnesium chloride solutions [13–16], when the EIC was TGSCC, the value of t_{ss}/t_f was 0.57 ± 0.02 and the slope of the linear relationship between $\log t_f$ and $\log l_{ss}$ was -2 . On the other hand, in the case of HE, the value of t_{ss}/t_f was 0.8 ± 0.02 and the slope of the linear relationship was -1 , which were similar to those for HE of pure titanium [17]. Therefore, the present results obtained suggest that the EIC of 5052-H3 is TGSCC and would be explained by adopting the TGSCC mechanism of the austenitic stainless steels. The TGSCC was based on a cyclic film rupture-formation event. A crack is initiated at slip steps and a film formed at the crack tip inhibits dislocation movement, which is enhanced by metal dissolution. As a result, a dislocation pileup takes place and

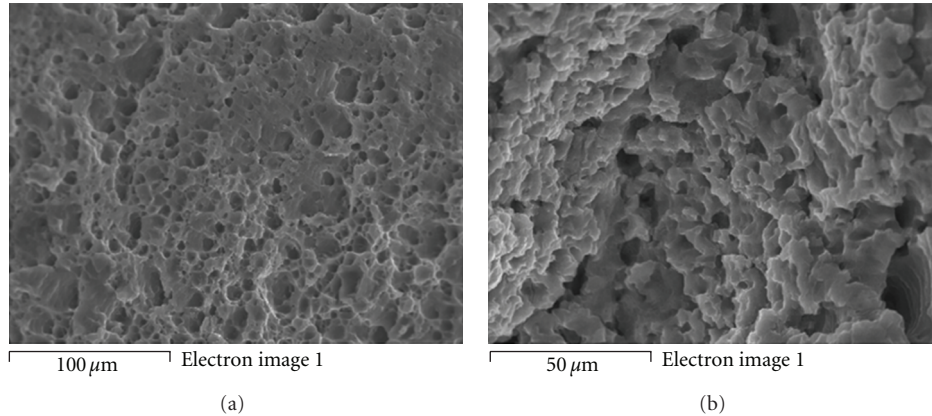


FIGURE 6: Fracture appearances for A5052-H3 at $T = 353\text{ K}$ and $\sigma = 230\text{ MPa}$; X550, LT orientation (a), TL orientation (b) in 0.5 M sodium chloride solution.

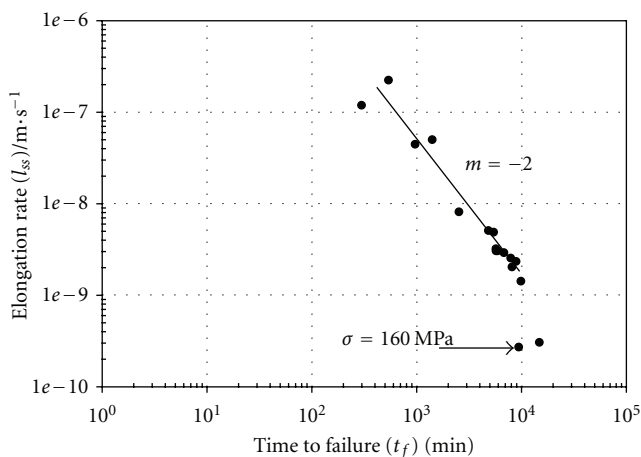


FIGURE 7: The relations between the logarithms of time to failure (t_f) and steady-state elongation rate (l_{ss}) for A5052-H3 in 0.5 M sodium chloride solution, where m is the slope of the straight line.

an additional local stress in the vicinity of crack tip (σ_{app}) is generated in addition to a local stress caused by applied stress (σ_{app}), where a net local stress (σ_{tip}) = $\sigma_{app} + \sigma_{add}$. When σ_{tip} reaches a critical film fracture stress (σ_{cri}), film fracture occurs. Such a film rupture-formation event is repeated inducing crack propagation until t_{ss} and as a result the steady state elongation rate can be obtained.

5. Conclusions

The following conclusions can be drawn from this work.

- (i) The applied stress dependences of the three parameters (t_f , l_{ss} , and t_{ss}/t_f) obtained from the corrosion elongation curve showed that these relationships were divided into three regions, the stress-dominated region, the SCC- or HE-dominated region, and the corrosion-dominated region.
- (ii) Aluminum alloy 5052-H3 showed identical behavior in both orientations at all applied stress range.

(iii) The fracture mode for aluminum alloy 5052-H3 was transgranular in both orientations.

(iv) The relationships between $\log t_f$ and $\log l_{ss}$ for the aluminum alloy used became a good straight line. The slope of the line was -2 .

References

- [1] M. O. Speidel, "Stress corrosion cracking of aluminum alloys," *Metallurgical Transactions A*, vol. 6, no. 4, pp. 631–651, 1975.
- [2] M. R. Bayoumi, "The mechanics and mechanisms of fracture in stress corrosion cracking of aluminium alloys," *Engineering Fracture Mechanics*, vol. 54, no. 6, pp. 879–889, 1996.
- [3] R. J. Gest and A. R. Troiano, "Stress corrosion and hydrogen embrittlement in an aluminum alloy," *Corrosion*, vol. 30, no. 8, pp. 274–279, 1974.
- [4] J. R. Pickens, J. R. Gordon, and J. A. S. Green, "Effect of loading mode on the stress-corrosion cracking of aluminum alloy 5083," *Metallurgical transactions. A*, vol. 14, no. 5, pp. 925–930, 1983.
- [5] J. G. Rinker, M. Marek, and T. H. Sanders, "Microstructure, toughness and stress corrosion cracking behavior of aluminum alloy 2020," *Materials Science and Engineering*, vol. 64, no. 2, pp. 203–221, 1984.
- [6] W. Y. CHU, Y. B. WANG, and C. M. HSIAO, "Research of hydrogen induced cracking and stress corrosion cracking in an aluminum alloy," *Corrosion*, vol. 38, no. 11, pp. 561–570, 1982.
- [7] K. Sieradzki and R. C. Newman, "Stress-corrosion cracking," *Journal of Physics and Chemistry of Solids*, vol. 48, no. 11, pp. 1101–1113, 1987.
- [8] S. Suresh, A. K. Vasudevan, and P. E. Bretz, "Mechanisms of slow fatigue crack growth in high strength aluminum alloys: role of microstructure and environment," *Metallurgical Transactions. A*, vol. 15, no. 2, pp. 369–379, 1984.
- [9] A. K. Vasudevan and S. Suresh, "Influence of corrosion deposits on near-threshold fatigue crack growth behavior in 2xxx and 7xxx series aluminum alloys," *Metallurgical Transactions. A*, vol. 13, no. 12, pp. 2271–2280, 1982.
- [10] R. Nishimura and K. Kudo, "Stress corrosion cracking of AISI 304 and AISI 316 austenitic stainless steels in HCl and H_2SO_4 solutions—prediction of time-to-failure and criterion

- for assessment of SCC susceptibility," *Corrosion*, vol. 45, no. 4, pp. 308–316, 1989.
- [11] R. Nishimura, "The effect of chloride ions on stress corrosion cracking of type 304 and type 316 austenitic stainless steels in sulfuric acid solution," *Corrosion Science*, vol. 34, no. 11, pp. 1859–1868, 1993.
- [12] R. Nishimura, "The effect of potential on stress corrosion cracking of type 316 and type 310 austenitic stainless steels," *Corrosion Science*, vol. 34, no. 9, pp. 1463–1473, 1993.
- [13] O. M. Alyousif and R. Nishimura, "The effect of test temperature on SCC behavior of austenitic stainless steels in boiling saturated magnesium chloride solution," *Corrosion Science*, vol. 48, no. 12, pp. 4283–4293, 2006.
- [14] O. M. Alyousif and R. Nishimura, "The stress corrosion cracking behavior of austenitic stainless steels in boiling magnesium chloride solutions," *Corrosion Science*, vol. 49, no. 7, pp. 3040–3051, 2007.
- [15] O. M. Alyousif and R. Nishimura, "Stress corrosion cracking and hydrogen embrittlement of sensitized austenitic stainless steels in boiling saturated magnesium chloride solutions," *Corrosion Science*, vol. 50, no. 8, pp. 2353–2359, 2008.
- [16] O. M. Alyousif and R. Nishimura, "On the stress corrosion cracking and hydrogen embrittlement of sensitized austenitic stainless steels in boiling saturated magnesium chloride solutions: effect of applied stress," *Corrosion Science*, vol. 50, no. 10, pp. 2919–2926, 2008.
- [17] R. Nishimura, J. Shirono, and A. Jonokuchi, "Hydrogen-induced cracking of pure titanium in sulphuric acid and hydrochloric acid solutions using constant load method," *Corrosion Science*, vol. 50, no. 9, pp. 2691–2697, 2008.
- [18] R. H. Jones, Ed., *Stress-Corrosion Cracking*, ASM International, Materials Park, Ohio, USA, 1992.

Research Article

Improvement of Pitting Corrosion Resistance of Type 316L Stainless Steel by Potentiostatic Removal of Surface MnS Inclusions

Nobuyoshi Hara,¹ Koichi Hirabayashi,^{2,3} Yu Sugawara,¹ and Izumi Muto¹

¹ Department of Materials Science, Graduate School of Engineering, Tohoku University, 6-6-02 Aobayama, Aoba-ku, Sendai 980-8579, Japan

² Department of Materials Science and Engineering, School of Engineering, Tohoku University, 6-6-02 Aobayama, Aoba-ku, Sendai 980-8579, Japan

³ ISFnetlife Ltd., Akasaka 7-1-16, Minato-ku, Tokyo 107-0052, Japan

Correspondence should be addressed to Nobuyoshi Hara, haran@material.tohoku.ac.jp

Received 26 March 2012; Accepted 15 May 2012

Academic Editor: Rokuro Nishimura

Copyright © 2012 Nobuyoshi Hara et al. This is an open access article distributed under the Creative Commons Attribution License, which permits unrestricted use, distribution, and reproduction in any medium, provided the original work is properly cited.

The beneficial effect of the removal of MnS inclusions on the pitting of stainless steels has been demonstrated in two ways. (1) High-purity Type 316L stainless steel with no inclusions was used as a specimen in the measurement of anodic polarization curves in 0.5 M NaCl and (2) commercial Type 316L stainless steel with MnS and slag-related inclusions was first polarized at different potentials for 30 min in 1 M Na₂SO₄ of pH 3 and then anodic polarization measurements were taken in 0.5 M NaCl. Pitting did not occur in the passive or transpassive region of the high-purity steel. The polarization treatment dissolved MnS and some oxide inclusions (CaO and SiO₂) on the surface of the commercial steel. An increase in pitting potential of the commercial steel was noted after treatment at potentials above 0.2 V. At the same time, the number of current spikes due to metastable pits decreased significantly. These results are more likely due to the beneficial effect of removing MnS inclusions from the steel surface rather than the modification effect of the chemical composition of passive films on the surface.

1. Introduction

Manganese sulfide (MnS) inclusions are known to act as the initiation sites of pitting corrosion on stainless steels [1–9], while the overall dissolution of the inclusions is not necessary for the formation of pit initiation sites [10–17]. It is therefore expected that the removal of surface MnS inclusions improves the pitting corrosion resistance of stainless steels. The aim of treating the surface of stainless steels with processes like nitric acid passivation (ASTM A380 and ASTM A967) is to form a stable Cr-enriched passive oxide film [18], which plays an important role in providing high corrosion resistance to stainless steels. Such surface treatment has an additional effect of dissolving and removing the MnS inclusions from the surface of stainless steels [19]. Therefore, the improvement of pitting corrosion resistance by passivation treatments can be attributed not only to

the modification of the chemical composition of the passive films but also to the removal of MnS from the surface of stainless steels. However, these two effects cannot be distinguished from each other in practice. For the further development of passivation treatments of stainless steels which meet environmental regulations and human safety standards, it is important to understand the intrinsic mechanism of each effect provided by passivation treatments.

The purpose of the present study is to examine solely the effect of removing MnS on the pitting corrosion resistance of austenitic stainless steels. To realize this purpose, surface MnS inclusions were removed by potentiostatic anodic polarization in a weakly acidic Na₂SO₄ solution and the pitting corrosion resistance was then examined by potentiodynamic polarization in a neutral NaCl solution.

TABLE 1: Chemical composition of specimens (wt%).

Specimen	C	Si	Mn	P	S	Ni	Cr	Mo	Cu
Commercial type 316L	0.022	0.69	0.9	0.027	0.004	12.08	17.25	2.09	—
High-purity type 316L	0.004	0.01	0.01	0.003	0.001	14.78	17.4	2.63	0.01

2. Experimental

Commercial Type 316L and high-purity Type 316L stainless steels were used as specimens. The chemical composition of the steels is given in Table 1. The high-purity Type 316L steel was prepared by a vacuum induction melting method using electrolytic Fe, Cr, and Ni and high-purity Mo as starting materials. Plates with dimensions of $15 \times 25 \times 2$ mm were cut from cold rolled sheets and heat-treated at 1323 K for 0.5 h followed by water quenching. The specimens were mechanically ground with SiC paper through a 1500 grid and cleaned ultrasonically with acetone. The specimen surfaces, except for the electrode area of 10×10 mm, were covered with epoxy resin and subsequently with paraffin.

To evaluate the pitting corrosion resistance, potentiodynamic polarization measurements were carried out with a conventional three-electrode cell. The electrolyte solution was 0.5 M NaCl at 298 K. The solution was deaerated with purified N_2 for more than 30 min before the measurements. The potential scan rate was $3.8 \times 10^{-4} \text{ V s}^{-1}$ (23 mV min^{-1}). The polarization was started from 50 mV lower than the open-circuit potential after immersion in the test solution for 10 min. The reference electrode was an Ag/AgCl (3.33 M KCl) electrode. All the potentials cited in this paper refer to this electrode.

In order to remove MnS inclusions from the surface of specimens, potentiostatic polarization treatment was performed at different potentials of 0.1 to 0.5 V for 30 min in 1 M Na_2SO_4 of pH 3. The solution pH was adjusted with the addition of a small amount of 1 M H_2SO_4 . Immediately after potentiostatic polarization treatment, the potentiodynamic anodic polarization curves in 0.5 M NaCl were measured in the manner described above.

A JEOL JSM-6510 scanning electron microscope (SEM) equipped with a JEOL JED-2300 energy dispersive X-ray spectrometer (EDS) was employed to analyze the inclusions on the surface of the specimens. The accelerating voltage was set at 20 kV. The specimens used for the SEM/EDS analysis were first mirror polished with a diamond paste of $1 \mu\text{m}$.

3. Results and Discussion

Figure 1 shows the anodic polarization curves of as-polished commercial Type 316L and high-purity Type 316L stainless steels in 0.5 M NaCl. The commercial steel exhibits many current spikes in the potential range from 0.2 V to 0.6 V and a sharp increase in current at around 0.6 V. These two characteristic events can be attributed to the formation of metastable pits and the growth of a stable pit, respectively. In the polarization curve of the high-purity steel, no characteristic pitting event was observed in the passivity and transpassivity region from 0.0 V to 1.2 V. No pit

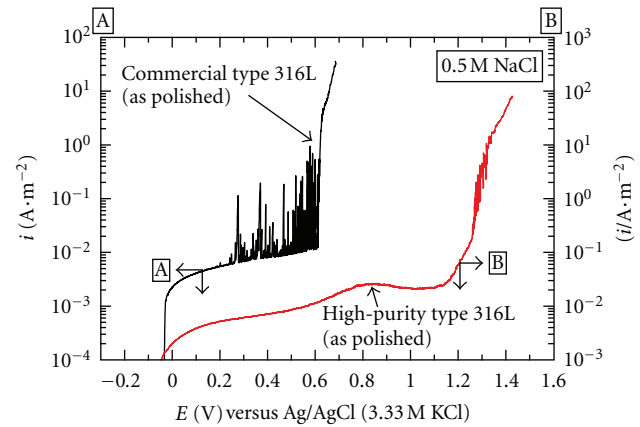


FIGURE 1: Anodic polarization curves of commercial Type 316L and high-purity Type 316L stainless steels in 0.5 M NaCl.

initiation sites were found on the surface of the high-purity steel.

Round inclusions with a diameter of 5 to $10 \mu\text{m}$ were observed on the surface of as-polished commercial Type 316L stainless steel. Figure 2 shows the SEM image and EDS elemental maps of a typical inclusion in the commercial steel. A skin of steel partly covers the central part of the inclusion. The inclusion consists mainly of oxides, CaO, SiO_2 , Al_2O_3 , and MgO, which come from steel making slag. Small MnS particles are distributed in the peripheral region of the oxide inclusion. Because a skin of steel partly covers the inclusion, MnS particles observed in the central part of the inclusion are actually not inside but outside the oxide inclusion. The dissolution of MnS at the boundary region between the inclusion and the steel matrix is thought to have triggered the pitting observed in Figure 1. No visible inclusion was detected on the surface of the high-purity steel.

The results of the previous study using a microelectrochemical technique suggest that MnS inclusions undergo electrochemical dissolution under anodic polarization in neutral solutions [10–17]. Figure 3 shows the SEM image and EDS elementary maps of commercial Type 316L stainless steel after potentiostatic polarization at 0.5 V for 30 min in 1 M Na_2SO_4 with pH 3. This SEM/EDS analysis was performed in the same region as the images in Figure 2. Not only MnS but also CaO and SiO_2 components were dissolved by the polarization treatment. Spinel ($MgAl_2O_3$) and perovskite ($CaTiO_3$) remained undissolved after polarization treatment. According to the potential-pH diagram of MnS- H_2O system [20], the stable Mn and S species in the potential range of 0.1 V to 0.5 V at pH 3 were Mn^{2+} and $S_2O_3^{2-}$ ions, respectively. Therefore, MnS undergoes

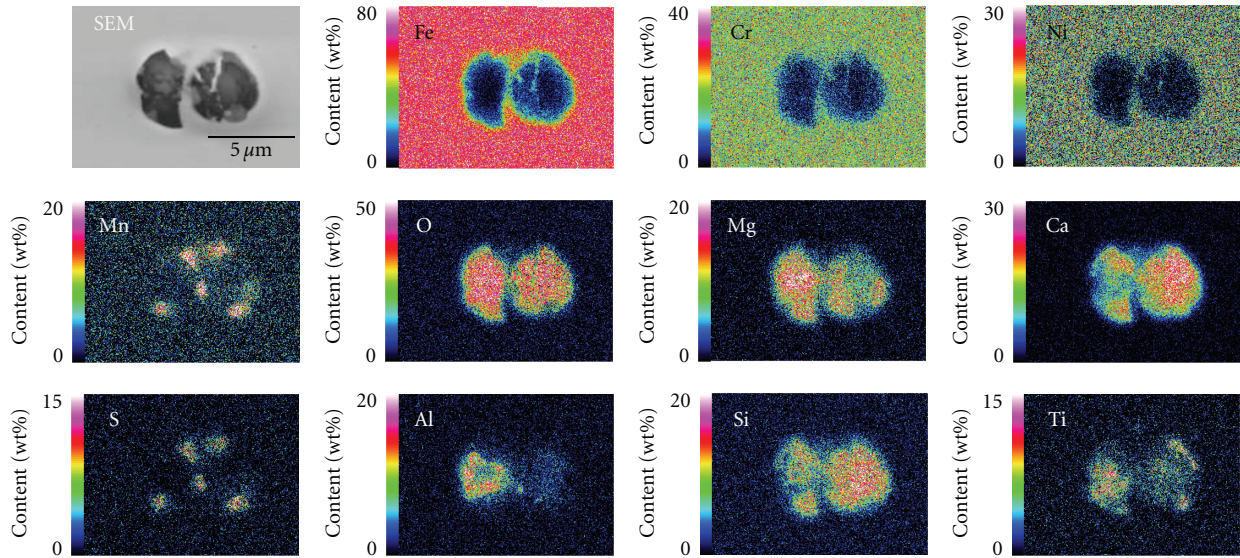


FIGURE 2: SEM image and EDS elemental mappings for as-polished commercial Type 316L stainless steel.

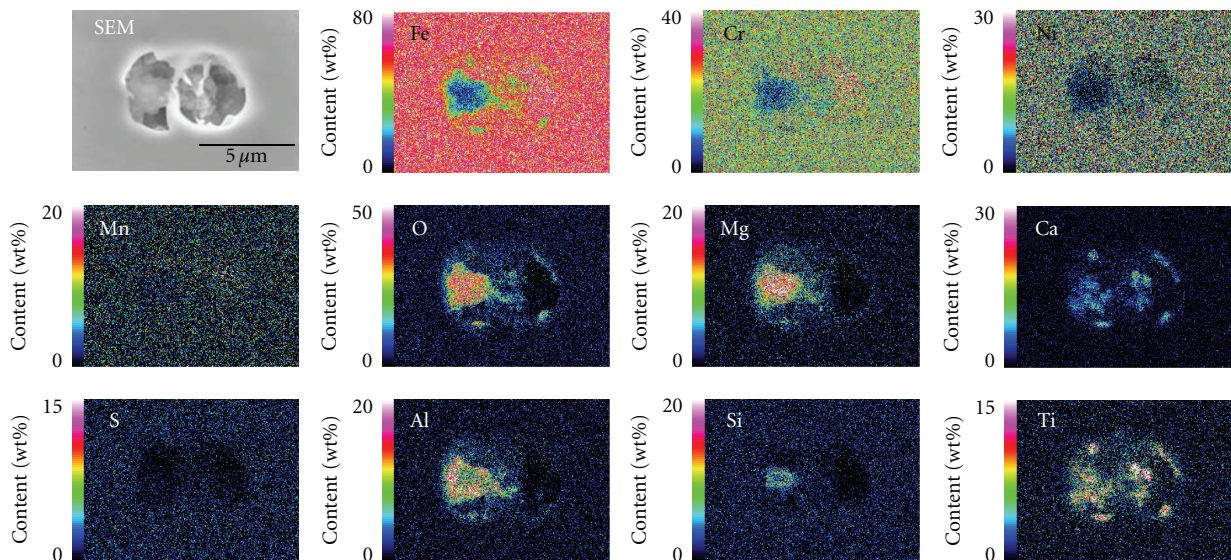
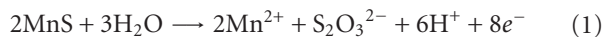


FIGURE 3: SEM image and EDS elemental mappings for the same region as in Figure 2 after polarization treatment at 0.5 V for 30 min in 1 M Na_2SO_4 of pH 3.

the following oxidative dissolution during the polarization treatments:



The dissolution of CaO and SiO_2 is caused by chemical reactions. Since SiO_2 itself is insoluble in weakly acidic solutions, the disappearance of SiO_2 after the treatments reveals that SiO_2 forms soluble calcium silicate such as $2\text{CaO} \cdot \text{SiO}_2$ and $3\text{CaO} \cdot \text{SiO}_2$ in the inclusion.

The effect of potentiostatic polarization treatments on the pitting corrosion resistance of commercial 316L stainless steel was examined by measuring the anodic polarization curves in 0.5 M NaCl. Figure 4 exhibits three anodic polarization curves after the same polarization treatment at 0.5 V

for 30 min in 1 M Na_2SO_4 . Compared with the as-polished specimen shown in Figure 1, fewer current spikes due to metastable pitting were noted and the onset potential of stable pitting was higher. However, the characteristics of the parameters of pitting varied from experiment to experiment, as can be seen in Figure 4. This indicates that the pitting had a randomness or a probabilistic property [21–23]. In order to statistically treat the pitting properties, we repeated the anodic polarization measurement at least eight times for each treatment condition. The following three electrochemical parameters were evaluated from each of the polarization curves: the onset potential of metastable pitting, E_r , the onset potential of stable pitting, E_{pit} , and the number of metastable pits, N_{msp} , which is assumed to be equal to the number of

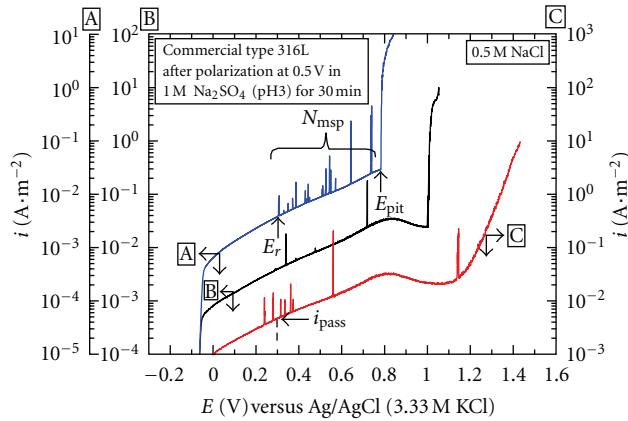


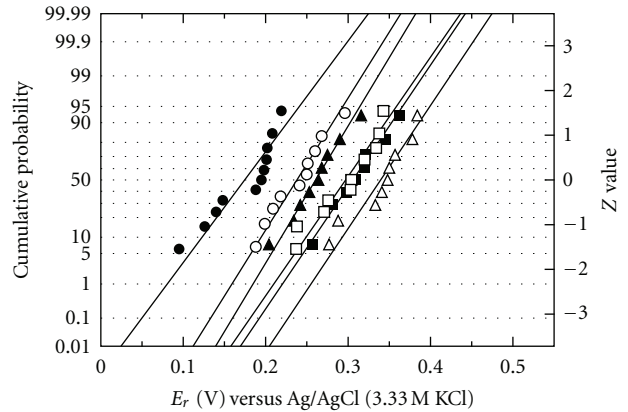
FIGURE 4: Anodic polarization curves of commercial Type 316L stainless steels in 0.5 M NaCl after polarization treatments at 0.5 V for 30 min in 1 M Na₂SO₄ of pH 3. The value of current density in each curve with a label of A, B, or C is given by the ordinate scale with the corresponding label.

current spikes in the potential region between E_r and E_{pit} . The distribution of each of these parameters was examined using a normal probability paper.

Figures 5, 6 and 7 show the normal probability plots of the distribution of E_r , E_{pit} , and N_{msp} , respectively. Linear relationships were observed for the three parameters examined, suggesting that the scattering of data follows a normal distribution. The average value of E_r , which is the value of E_r at the cumulative probability of 50%, increased gradually with increasing treatment potential, while the slope of the normal probability plot, which corresponds to the reciprocal of standard deviation, remained unchanged. The average value of E_{pit} increased significantly with increasing treatment potential and, at the same time, the slope of the normal probability plot became less steep. The latter result is due to the fact that very high E_{pit} values above 1.0 V were obtained for several specimens treated at potentials higher than 0.2 V. In other words, the scattering of E_{pit} data originates not only from the intrinsic nature of the pitting process but also from the variation of the effectiveness of polarization treatments for eliminating pit initiation sites.

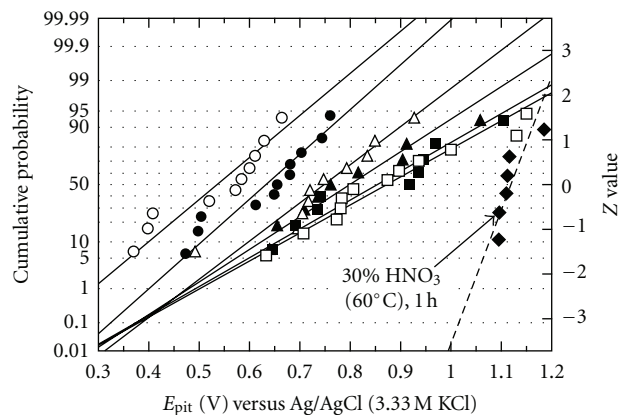
In Figure 7 the average value of N_{msp} decreases remarkably with polarization treatment. The average value of N_{msp} for specimens treated at potentials above 0.3 V is at least one order of magnitude lower than that for the as-polished specimen, indicating that the number of pit initiation sites decreased significantly with the polarization treatments employed in this study. The decrease in the number of pit initiation sites may well explain the observed increase in E_{pit} . However, there is also a possibility that the passivation effect, that is, the Cr enrichment in passive films, was induced by the polarization treatment and that this led to the improvement of pitting resistance.

To examine the passivation effect, the anodic polarization curves in 0.5 M NaCl were measured after the following nitric passivation treatment: the immersion of specimens in 30% HNO₃ at 60°C for 1 h. A typical result is shown in Figure 8



- As polished
- 0.1 V, 30 min
- ▲ 0.2 V, 30 min
- △ 0.3 V, 30 min
- 0.4 V, 30 min
- 0.5 V, 30 min

FIGURE 5: Normal probability plots of onset potential of metastable pitting, E_r , in 0.5 M NaCl for commercial Type 316L stainless steels after polarization treatments at different potentials for 30 min in 1 M Na₂SO₄ of pH 3.



- As polished
- 0.1 V, 30 min
- ▲ 0.2 V, 30 min
- △ 0.3 V, 30 min
- 0.4 V, 30 min
- 0.5 V, 30 min

FIGURE 6: Normal probability plots of onset potential of stable pitting, E_{pit} , in 0.5 M NaCl for commercial Type 316L stainless steels after polarization treatments at different potentials for 30 min in 1 M Na₂SO₄ of pH 3. The data for nitric acid passivation is shown for comparison.

and compared with another result after the polarization treatment at 0.5 V. After the nitric acid passivation treatment, no metastable pitting was observed and stable pitting occurred only at a very high potential of about 1.1 V (see also Figure 6). Even though the pitting potential of the two specimens shown in Figure 8 is almost identical, the current densities in the passivity and transpassivity regions are quite different. The current density of the specimen passivated in nitric acid was extremely low in the passivity region but increased remarkably with potential in the transpassivity region above 0.6 V. Such a large change in the current density

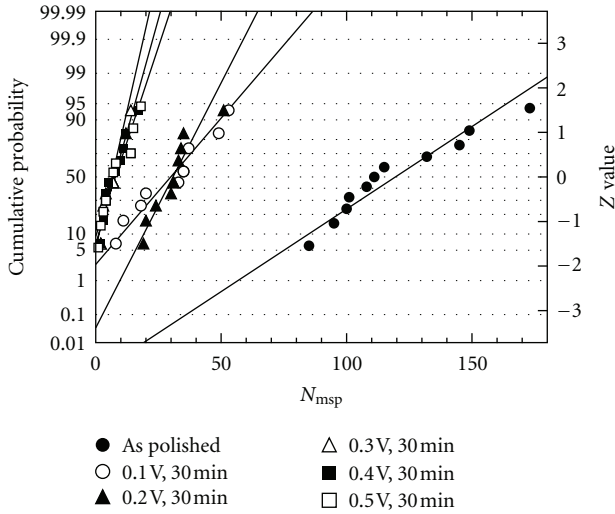


FIGURE 7: Normal probability plots of the number of metastable pits, N_{msp} , in 0.5 M NaCl for commercial Type 316L stainless steels after polarization treatments at different potentials for 30 min in 1 M Na_2SO_4 of pH 3.

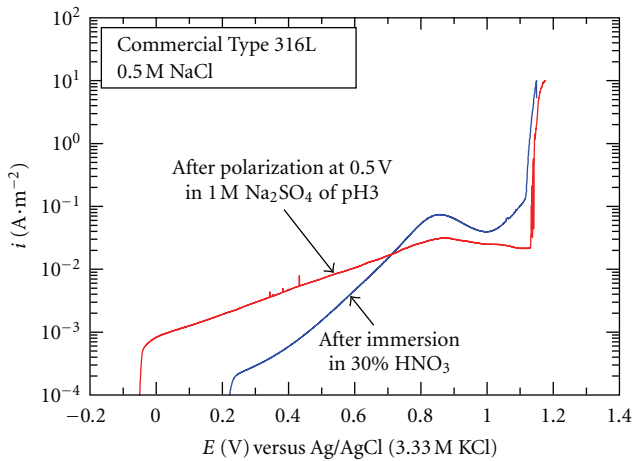


FIGURE 8: Anodic polarization curves in 0.5 M NaCl for commercial Type 316L stainless steels after passivation for 1 h in 30% HNO_3 at 60°C and after polarization treatments at 0.5 V for 30 min in 1 M Na_2SO_4 of pH 3.

of the specimen passivated in nitric acid can be explained by the presence of a passive film enriched with Cr oxide. The presence of Cr oxide suppresses dissolution in the passive state but accelerates dissolution in the transpassive state to form soluble Cr (VI) species.

The passive current density at 0.3 V, i_{pass} , in 0.5 M NaCl was read from all the polarization curves measured, and its average value was calculated and then plotted against the polarization treatment potential in Figure 9. While the average value of i_{pass} decreased slightly with increasing treatment potential, it was always one order of magnitude higher than that for specimens passivated in nitric acid and was rather close to that for as-polished specimens. It is therefore suggested that the polarization treatment used in

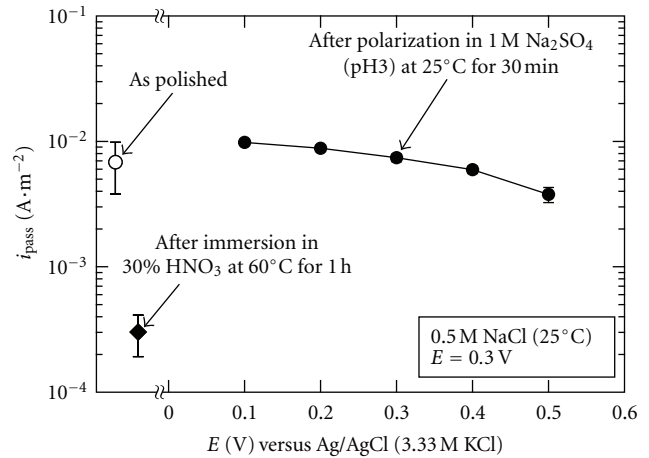


FIGURE 9: Passive current density, i_{pass} , at 0.3 V in 0.5 M NaCl as a function of polarization potential in 1 M Na_2SO_4 of pH 3 for commercial Type 316L stainless steels. The corresponding data for as-polished and HNO_3 passivated steels are shown for comparison. Error bars indicate a standard deviation of i_{pass} .

this study did not have a strong passivation effect but had the significant beneficial effect of reducing the number of pit initiation sites.

4. Conclusions

By comparing the anodic polarization curves in 0.5 M NaCl for high-purity Type 316L stainless steels with those of commercial 316L stainless steels, it is confirmed that the removal of MnS is essential to derive excellent pitting corrosion resistance. Manganese sulfide (MnS) and some oxide (CaO , SiO_2) inclusions on the surface of commercial Type 316L stainless steels were dissolved by potentiostatic polarization treatments in 1 M Na_2SO_4 with pH 3. After polarization treatment, the number of current spikes due to metastable pitting decreased significantly and the pitting potential increased, while the passive current density did not change as remarkably as for specimens subjected to nitric passivation treatment. The elimination of pit initiation sites rather than the modification of the chemical composition of passive films is important to improve the pitting corrosion resistance of stainless steels.

References

- [1] J. E. Castle and R. Ke, "Studies by auger spectroscopy of pit initiation at the site of inclusions in stainless steel," *Corrosion Science*, vol. 30, no. 4-5, pp. 409–428, 1990.
- [2] M. A. Baker and J. E. Castle, "The initiation of pitting corrosion of stainless steels at oxide inclusions," *Corrosion Science*, vol. 33, no. 8, pp. 1295–1303, 1992.
- [3] R. Ke and R. Alkire, "Surface analysis of corrosion pits initiated at MnS inclusions in 304 stainless steel," *Journal of the Electrochemical Society*, vol. 139, no. 6, pp. 1573–1580, 1992.
- [4] M. A. Baker and J. E. Castle, "The initiation of pitting corrosion at MnS inclusions," *Corrosion Science*, vol. 34, no. 4, pp. 667–682, 1993.

- [5] R. Ke and R. Alkire, "Initiation of corrosion pits at inclusions on 304 stainless steel," *Journal of the Electrochemical Society*, vol. 142, no. 12, pp. 4056–4062, 1995.
- [6] G. S. Frankel, "Pitting corrosion of metals: a review of the critical factors," *Journal of the Electrochemical Society*, vol. 145, no. 6, pp. 2186–2198, 1998.
- [7] H. Krawiec, V. Vignal, O. Heintz, R. Oltra, and J. M. Olive, "Influence of the chemical dissolution of MnS inclusions on the electrochemical behavior of stainless steels," *Journal of the Electrochemical Society*, vol. 152, no. 7, pp. B213–B219, 2005.
- [8] T. L. S. L. Wijesinghe and D. J. Blackwood, "Real time pit initiation studies on stainless steels: the effect of sulphide inclusions," *Corrosion Science*, vol. 49, no. 4, pp. 1755–1764, 2007.
- [9] G. S. Eklund, "Initiation of pitting at sulfide inclusions in stainless steel," *Journal of the Electrochemical Society*, vol. 121, no. 4, pp. 467–473, 1974.
- [10] G. Wranglén, "Pitting and sulphide inclusions in steel," *Corrosion Science*, vol. 14, no. 5, pp. 331–349, 1974.
- [11] T. Suter, E. G. Webb, H. Böhni, and R. C. Alkire, "Pit initiation on stainless steels in 1 M NaCl with and without mechanical stress," *Journal of the Electrochemical Society*, vol. 148, no. 5, pp. B174–B185, 2001.
- [12] C. Punckt, M. Bölscher, H. H. Rotermund et al., "Sudden onset of pitting corrosion on stainless steel as a critical phenomenon," *Science*, vol. 305, no. 5687, pp. 1133–1136, 2004.
- [13] P. Schmuki, H. Hildebrand, A. Friedrich, and S. Virtanen, "The composition of the boundary region of MnS inclusions in stainless steel and its relevance in triggering pitting corrosion," *Corrosion Science*, vol. 47, no. 5, pp. 1239–1250, 2005.
- [14] H. Krawiec, V. Vignal, O. Heintz, and R. Oltra, "Influence of the dissolution of MnS inclusions under free corrosion and potentiostatic conditions on the composition of passive films and the electrochemical behaviour of stainless steels," *Electrochimica Acta*, vol. 51, no. 16, pp. 3235–3243, 2006.
- [15] I. Muto, Y. Izumiyama, and N. Hara, "Microelectrochemical measurements of dissolution of MnS inclusions and morphological observation of metastable and stable pitting on stainless steel," *Journal of the Electrochemical Society*, vol. 154, no. 8, pp. C439–C444, 2007.
- [16] I. Muto, D. Ito, and N. Hara, "Microelectrochemical investigation on pit initiation at sulfide and oxide inclusions in type 304 stainless steel," *Journal of the Electrochemical Society*, vol. 156, no. 2, pp. C55–C61, 2009.
- [17] S. J. Zheng, Y. J. Wang, B. Zhang, Y. L. Zhu, C. Liu, and P. Hu, "Identification of MnCr₂O₄ nano-octahedron in catalysing pitting corrosion of austenitic stainless steels," *Acta Materialia*, vol. 58, no. 15, pp. 5070–5085, 2010.
- [18] J. S. Noh, N. J. Laycock, W. Gao, and D. B. Wells, "Effects of nitric acid passivation on the pitting resistance of 316 stainless steel," *Corrosion Science*, vol. 42, no. 12, pp. 2069–2084, 2000.
- [19] R. R. Maller, "Passivation of stainless steel," *Trends in Food Science and Technology*, vol. 9, no. 1, pp. 28–32, 1998.
- [20] J. Shinozaki, I. Muto, T. Omura, M. Numata, and N. Hara, "Local dissolution of MnS inclusion and microstructural distribution of absorbed hydrogen in carbon steel," *Journal of the Electrochemical Society*, vol. 158, no. 9, pp. C302–C309, 2011.
- [21] T. Shibata and T. Takeyama, "Stochastic theory of pitting corrosion," *Corrosion*, vol. 33, no. 7, pp. 243–251, 1977.
- [22] T. Shibata, "Stochastic studies of passivity breakdown," *Corrosion Science*, vol. 31, pp. 413–423, 1990.
- [23] T. Shibata, "1996 W.R. Whitney Award Lecture: statistical and stochastic approaches to localized corrosion," *Corrosion*, vol. 52, no. 11, pp. 813–830, 1996.

Research Article

The Corrosion Behavior of Ni₃Al/Ni₃V Two-Phase Intermetallic Compounds in Various Acidic Solutions

Gadang Priyotomo, Hideyuki Momono, Sanat Wagle, Kenji Okitsu, Akihiro Iwase, Yasuyuki Kaneno, Rokuro Nishimura, and Takayuki Takasugi

Department of Materials Science, Graduate School of Engineering, Osaka Prefecture University, 1-1 Gakuen-cho, Sakai, Osaka 599-8531, Japan

Correspondence should be addressed to Gadang Priyotomo, gadangp@gmail.com

Received 28 February 2012; Revised 21 March 2012; Accepted 5 April 2012

Academic Editor: Toshiaki Ohtsuka

Copyright © 2012 Gadang Priyotomo et al. This is an open access article distributed under the Creative Commons Attribution License, which permits unrestricted use, distribution, and reproduction in any medium, provided the original work is properly cited.

The corrosion behavior of the Ni₃Al/Ni₃V two-phase intermetallic compounds with and without minor elements (Nb, Co, and Cr) to be composed of L₁₂ phase (Ni₃Al) and a mixed phase of L₁₂ (Ni₃Al) and D0₂₂ (Ni₃V) has been investigated by using an immersion test in 0.5 kmol/m³ HCl, H₂SO₄, and HNO₃ solutions. The surface morphology was observed before and after the immersion test by scanning electron microscope (SEM). The results were compared to those of the L₁₂ single-phase Ni₃(Si,Ti) and austenitic stainless steel type 304. In all acidic solutions, preferential dissolution of (L₁₂ + D0₂₂) phase was found in Ni₃Al/Ni₃V, but no intergranular attack, whereas the attacks took place on Ni₃(Si,Ti). The Ni₃Al/Ni₃V showed a higher corrosion resistance in HCl solution and a lower resistance in HNO₃ solution than Ni₃(Si,Ti) and type 304. The addition of the minor elements enhanced corrosion resistance in HNO₃ solution, but not clearly in HCl and H₂SO₄ solutions. In HCl and H₂SO₄, their weight losses during the immersion test were almost the same.

1. Introduction

Recently, Ni-Al-V intermetallic compounds with a two-phase microstructure of Ni₃Al (L₁₂) and Ni₃V (D0₂₂) phases have been developed by Takasugi et al. [1–13] and are confirmed to exhibit a highly coherent interface between these constituent phases. They have superior mechanical properties (i.e., high creep rupture life, high hardness, low thermal expansion, and better thermal conductivity) and also have high tensile strength and fracture toughness over a broad range of temperature in comparison with those of Inconel 750, Inconel 718 and Hastelloy [1–13]. Therefore, the Ni₃Al/Ni₃V two-phase intermetallic compounds are a candidates as materials in land-based, marine-based, and aero-gas turbine industries (turbine blade), high strength nut and bolt, and high temperature bearing or high temperature tool [8, 9, 14]. However, many studies revealed that the intermetallic compounds containing aluminum are very susceptible to hydrogen embrittlement [15–18], where hydrogen embrittlement takes place with permeation of

atomic hydrogen formed by corrosion reaction into the compounds. Hence, to suppress this environmental embrittlement a small amount of boron was added to these compounds. However, it was reported that the boron segregation at grain boundaries became the preferential dissolution site and led to the intergranular attack in the L₁₂ single-phase Ni₃(Si,Ti) [19].

Furthermore, Ni base intermetallic compounds such as single-phase Ni₃(Si,Ti) have attractive properties for high-temperature structural material (e.g., high phase stability and strength at high temperature), but the intermetallic compounds have been shown to suffer from (1) poor ductility at room temperature and low strength at high temperature, and (2) to have the decrease in strength at high temperature. However, multiphase intermetallic compounds such as Ni₃Al/Ni₃V two-phase intermetallic compounds were found to improve these weakness points [13].

At present, with regard to the Ni₃Al/Ni₃V two-phase intermetallic compounds, there are few studies on their

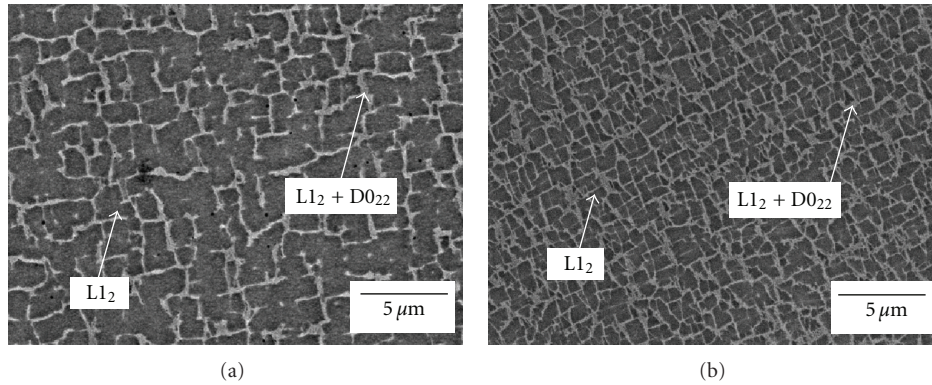


FIGURE 1: Microstructures of $\text{Ni}_3\text{Al}/\text{Ni}_3\text{V}$ two-phase intermetallic compounds: (a) type 1 and (b) type 2 before experiments and after galvanostatic etching.

corrosion behavior in aqueous solutions at ambient temperature. Therefore, the purpose of this work is to elucidate the corrosion behavior of the $\text{Ni}_3\text{Al}/\text{Ni}_3\text{V}$ two-phase intermetallic compounds with and without minor elements of Nb, Co, and Cr in HCl, H_2SO_4 , and HNO_3 solutions and to compare with that of L1_2 single-phase $\text{Ni}_3(\text{Si},\text{Ti})$ intermetallic compound and austenitic stainless steel type 304.

2. Experimental

2.1. The Specimens. The $\text{Ni}_3\text{Al}/\text{Ni}_3\text{V}$ two-phase intermetallic compounds with and without minor elements used in the present study were fabricated from the raw materials of 99.9 wt% Ni, 99.9 wt% Al, 99.9 wt% V, 99.9 wt% Nb, 99.9 wt% Co, and 99.9 wt% Cr. These compounds were prepared as buttons by using an arc melting method under an argon gas atmosphere using a nonconsumable tungsten electrode on a copper hearth. A small amount of boron was added to suppress an intergranular fracture in environments such as air, water, and hydrogen gas [1–13]. Then the button ingot was homogenized at 1553 K for 3 h in vacuum and then furnace cooled. The plate specimens with a 1 mm thickness were prepared by cutting perpendicular to the basal plane of the homogenized button, and then test specimens were cut to the geometry of 1.0 mm \times 10.0 mm \times 20.0 mm by using an electrodischarge machine. The nominal chemical compositions of two types of $\text{Ni}_3\text{Al}/\text{Ni}_3\text{V}$ two-phase intermetallic compounds (hereafter referred to as a type 1 without minor elements and type 2 with minor elements) were shown in Table 1. Here, major alloy elements are Ni, Al, and V and minor elements such as Nb, Co, and Cr are added at the levels of several atomic percents. The addition of Co and Cr was reported to improve oxidation property, while that of Nb to improve high temperature strength and wear properties [8].

2.2. Pretreatment of the Specimens and Test Solutions. The specimens homogenized were cut into 1.2 mm \times 9 mm \times 15 mm. Then they were polished to 1.0 micrometer alumina

paste, degreased by acetone in an ultrasonic cleaner and washed with distilled water. The test solutions, 0.5 kmol/m³ HCl, H_2SO_4 , and HNO_3 , were prepared by reagent grade chemicals and distilled water. For microstructure observation, galvanostatic etching of the mechanically polished specimens was conducted in a solution consisting of 15 mL of 17.8 kmol/m³ H_2SO_4 and 85 mL of methanol at a current density of 0.446 A/cm² for 30 sec at a temperature of 243 K.

2.3. Corrosion Test. The corrosion test of the mechanically polished specimen was conducted by immersion in the three acidic solutions at 303 K under an open circuit condition. A corrosion weight loss (ΔW) was estimated from the difference in weights of the specimens before and after the immersion test at various immersion times up to a maximum time of 96 hours. After the experiments, the morphology of the specimen surfaces was observed by using scanning electron microscope (SEM).

3. Results and Discussion

3.1. Microstructure of $\text{Ni}_3\text{Al}/\text{Ni}_3\text{V}$ Two-Phase Intermetallic Compounds. The $\text{Ni}_3\text{Al}/\text{Ni}_3\text{V}$ two-phase intermetallic compound exhibited the two phases composed of the cuboidal L1_2 precipitate and ($\text{L1}_2 + \text{D0}_{22}$) phase [1, 2] as shown in the magnified photos in Figure 1. Furthermore, Figure 1 shows the microstructure of the $\text{Ni}_3\text{Al}/\text{Ni}_3\text{V}$ two-phase intermetallic compound after the galvanostatic etching. The intermetallic compound consists of two regions of an L1_2 phase of Ni_3Al (dark areas) and a mixed phase of L1_2 of Ni_3Al and D0_{22} of Ni_3V (white areas). In addition, Figure 1 clearly shows that the size of the cuboidal L1_2 precipitate decreases with decreasing the Al content: in other words, a volume fraction of the cuboidal L1_2 precipitate increases with the increase in the Al content in the compounds. The observed microstructures were consistent with those reported in the previous studies [1–13].

3.2. Weight Loss. Figure 2 shows the change in weight loss with immersion time for type 1 and type 2 in 0.5 kmol/m³

TABLE 1: Chemical compositions of the materials investigated.

Alloy	At%														ppm
	C	Si	Mn	P	Nb	S	Ni	Cr	Co	Mo	Al	Fe	V	Ti	
Type 1	—	—	—	—	—	—	75	—	—	—	12	—	13	—	100
Type 2	—	—	—	—	3	—	70.5	3	3	—	10	—	10.5	—	100

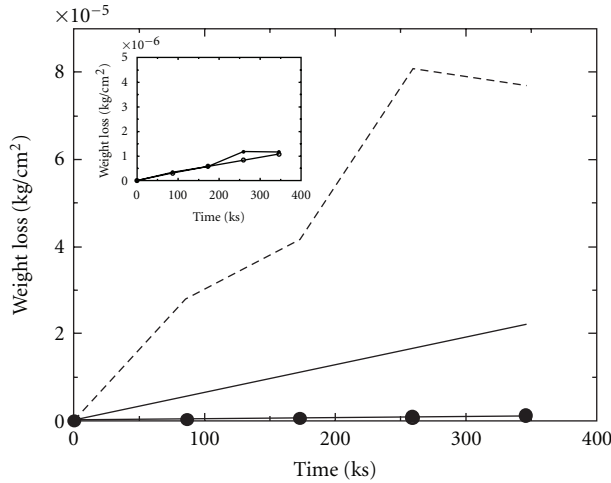


FIGURE 2: The weight losses of $\text{Ni}_3\text{Al}/\text{Ni}_3\text{V}$ two-phase intermetallic compounds: • type 1, ○ type 2, (solid line) $\text{Ni}_3(\text{Si},\text{Ti})$, and (dotted line) Type 304 as a function of immersion time in 0.5 kmol/m^3 HCl solution at 303 K.

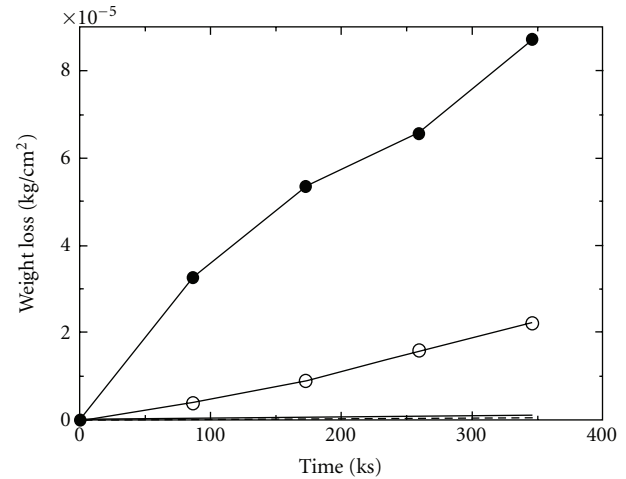


FIGURE 4: The weight losses of $\text{Ni}_3\text{Al}/\text{Ni}_3\text{V}$ two-phase intermetallic compounds: • type 1, ○ type 2, (solid line) $\text{Ni}_3(\text{Si},\text{Ti})$, and (dotted line) Type 304 as a function of immersion time in 0.5 kmol/m^3 HNO_3 solution at 303 K.

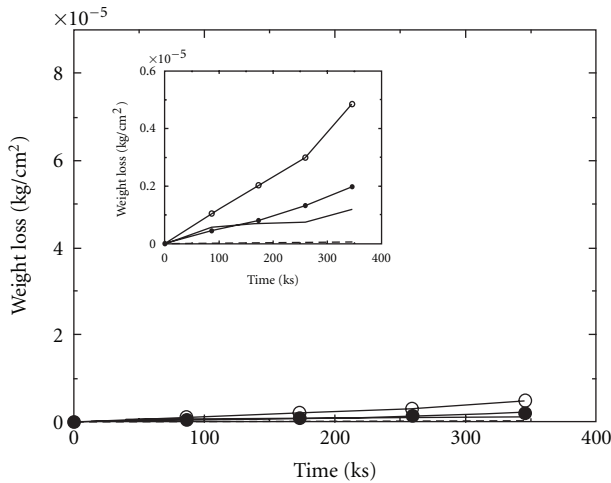


FIGURE 3: The weight losses of $\text{Ni}_3\text{Al}/\text{Ni}_3\text{V}$ two-phase intermetallic compounds: • type 1, ○ type 2, (solid line) $\text{Ni}_3(\text{Si},\text{Ti})$, and (dotted line) Type 304 as a function of immersion time in 0.5 kmol/m^3 H_2SO_4 solution at 303 K.

HCl solution at 303 K, where that for the L1_2 single-phase $\text{Ni}_3(\text{Si},\text{Ti})$ and austenitic stainless steel type 304 was shown for comparison [19]. The weight losses of both compounds were found to be significantly lower than those of $\text{Ni}_3(\text{Si},\text{Ti})$ and type 304. In addition, in the figure magnified in Figure 2,

the weight loss for type 1 was almost the same as that for type 2 over the whole immersion time.

Figure 3 shows the change in weight loss with immersion time for type 1 and type 2 in 0.5 kmol/m^3 H_2SO_4 solution at 303 K, where that for $\text{Ni}_3(\text{Si},\text{Ti})$ and type 304 was also shown for comparison [19]. The weight losses of $\text{Ni}_3(\text{Si},\text{Ti})$ and type 304 were much smaller than those in Figure 2, whereas those of type 1 and type 2 became slightly larger than those in Figure 2. Furthermore, from the figure magnified in Figure 3, it was found that the weight losses of both type 1 and type 2 were larger than those of $\text{Ni}_3(\text{Si},\text{Ti})$ and type 304, and the weight loss of type 2 was larger than that of type 1.

Figure 4 shows the change in weight loss with immersion time for type 1 and type 2 in 0.5 kmol/m^3 HNO_3 solution at 303 K, where that for $\text{Ni}_3(\text{Si},\text{Ti})$ and type 304 was also shown for comparison [19]. In this solution, the weight losses of both type 1 and type 2 were larger than those of $\text{Ni}_3(\text{Si},\text{Ti})$ and type 304. This result was found to be clearly different from that in the HCl solution. In addition, the weight loss of type 1 was larger than that of type 2.

From the results obtained, it was found that the magnitude of weight losses for type 1 and type 2 in acidic solutions increased in order of $\text{HNO}_3 > \text{H}_2\text{SO}_4 > \text{HCl}$, while that for $\text{Ni}_3(\text{Si},\text{Ti})$ and type 304 increased in order of $\text{HCl} > \text{H}_2\text{SO}_4 > \text{HNO}_3$ solutions.

3.3. Surface Morphology of $\text{Ni}_3\text{Al}/\text{Ni}_3\text{V}$ Two-Phase Intermetallic Compounds after Immersion Test. Figure 5 shows the

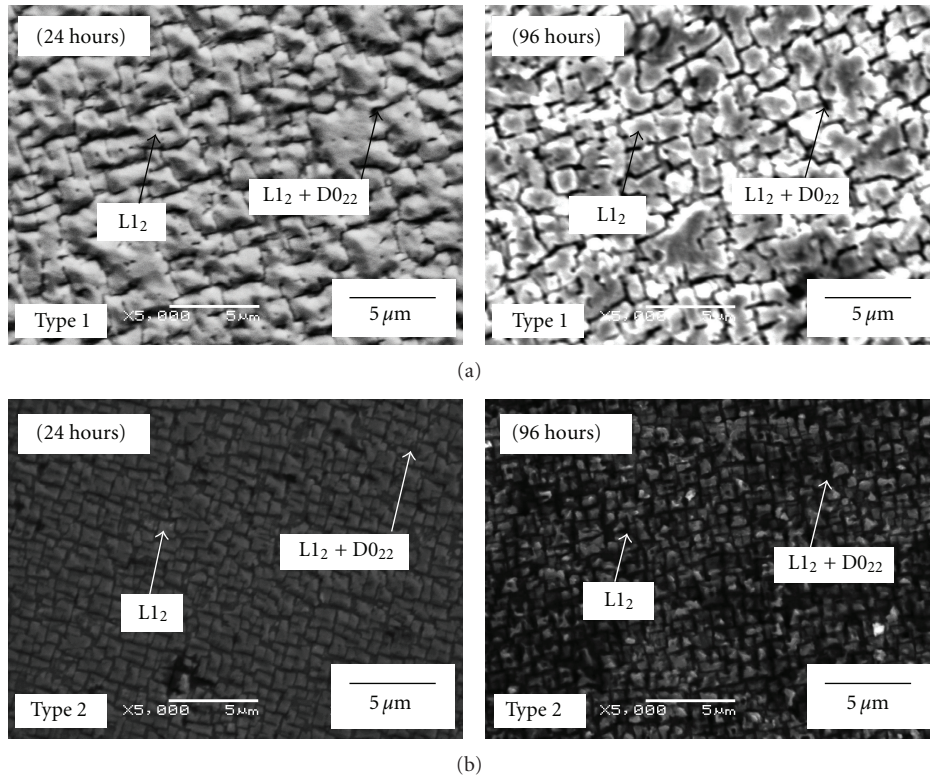


FIGURE 5: SEM microstructures of Ni₃Al/Ni₃V two-phase intermetallic compounds: (a) type 1 and (b) type 2 after the immersion times of 24 hours and 96 hours in 0.5 kmol/m³ HCl solution at 303 K.

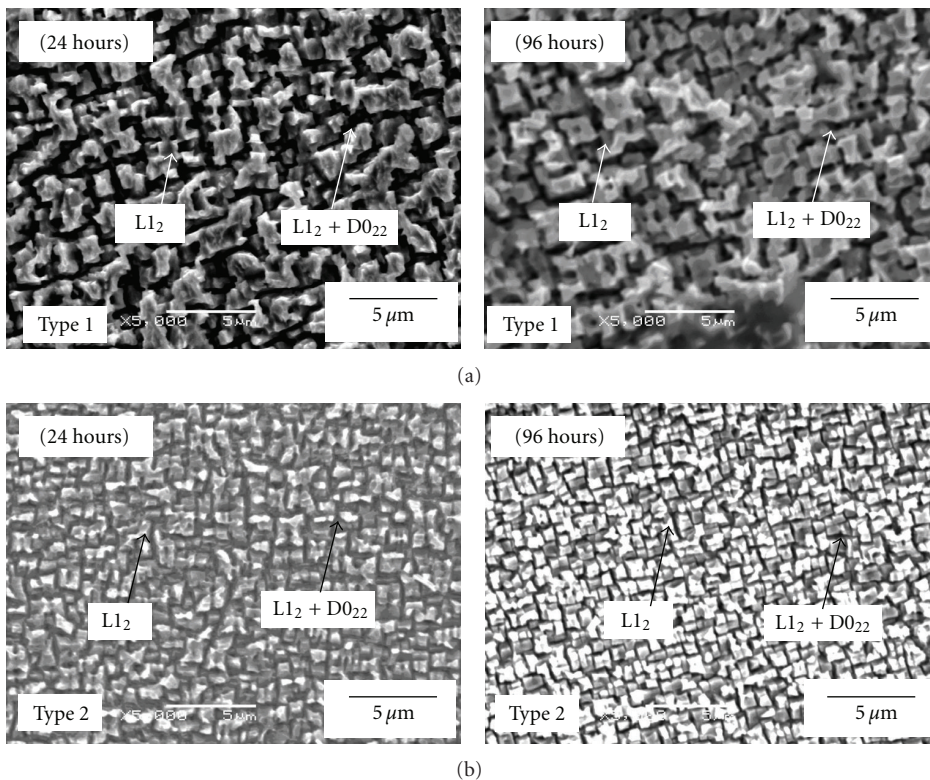


FIGURE 6: SEM microstructures of Ni₃Al/Ni₃V two-phase intermetallic compounds: (a) type 1 and (b) type 2 after the immersion times of 24 hours and 96 hours in 0.5 kmol/m³ H₂SO₄ solution at 303 K.

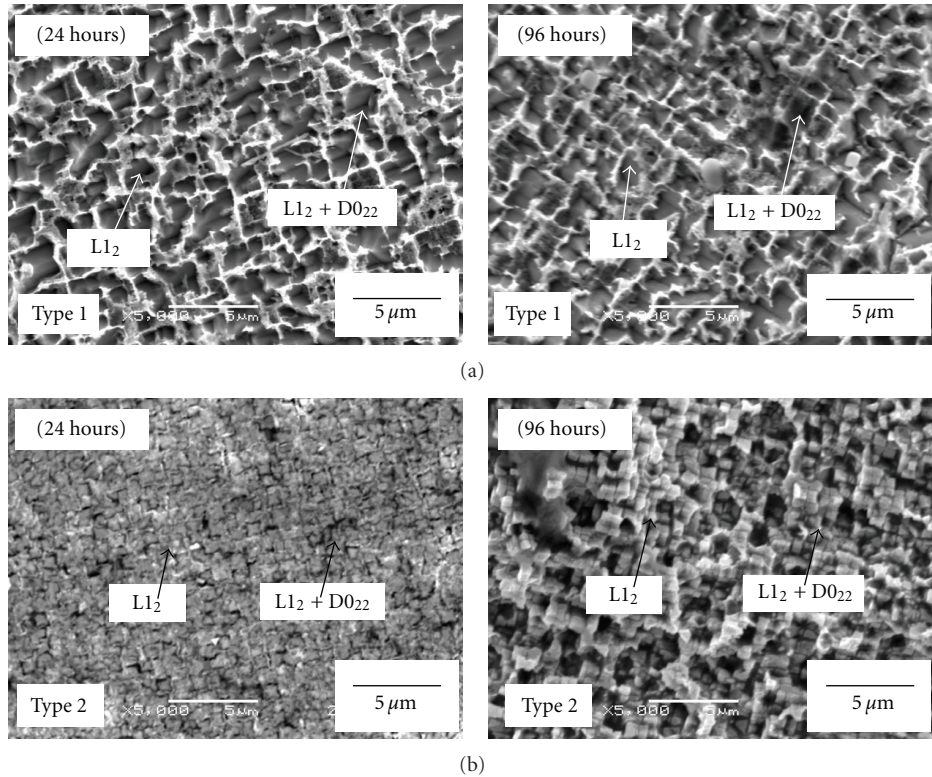


FIGURE 7: SEM microstructures of $\text{Ni}_3\text{Al}/\text{Ni}_3\text{V}$ two-phase intermetallic compounds: (a) type 1 and (b) type 2 after the immersion times of 24 hours and 96 hours in $0.5 \text{ kmol/m}^3 \text{ HNO}_3$ solution at 303 K.

surface morphologies of type 1 and type 2 at the immersion times of 24 hours and 96 hours in the HCl solution. In the HCl solution, a preferential dissolution of the mixed phase of L1_2 and D0_{22} (Ni_3Al and Ni_3V) was slightly observed at the initial stage (24 hours). At the immersion time of 96 hours, its preferential dissolution became significant. Furthermore, it was found that an intergranular attack was not observed on both compounds, although the attack was observed at $\text{Ni}_3(\text{Si},\text{Ti})$ in HCl solution in previous work [19].

Figure 6 shows the surface morphologies of type 1 and type 2 at the immersion times of 24 hours and 96 hours in the H_2SO_4 solution. The results were almost similar to those in Figure 5. Furthermore, Figure 7 shows the surface morphologies of type 1 and type 2 at the immersion times of 24 hours and 96 hours in the HNO_3 solution. Although the morphologies were similar to those in the HCl and H_2SO_4 solutions, especially for type 2, the degree of corrosion was larger than that in the HCl and H_2SO_4 solutions, in a sense that a dissolution of the L1_2 phase appeared to occur clearly in the HNO_3 solution as well as the development of the preferential dissolution for the mixed phase of L1_2 and D0_{22} (Ni_3Al and Ni_3V), especially compared to those in the HCl solution.

3.4. The Effect of Vanadium on Corrosion Resistance of $\text{Ni}_3\text{Al}/\text{Ni}_3\text{V}$ Two-Phase Intermetallic Compounds. From the above results on type 1 and type 2, it was found that (1) the weight loss increased in order of $\text{HNO}_3 > \text{H}_2\text{SO}_4 > \text{HCl}$

solutions, (2) the preferential dissolution of the mixed phase of L1_2 and D0_{22} (Ni_3Al and Ni_3V) took place, and (3) type 2 containing the minor elements showed a higher corrosion resistance than type 1 without them in HNO_3 solution. These three points would be explained as follows.

Schlain et al. [20] reported that a high purity vanadium (99.9%) was highly resistive to corrosion in H_3PO_4 , H_2SO_4 , and HCl solutions at 35°C , but corroded rapidly in HNO_3 solution. The corrosion of vanadium would explain the above points. Since the corrosion behavior of type 1 and type 2 including vanadium should be reflected by that of the bulk vanadium in the present solutions (point 1), vanadium was present only in the mixed phase (point 2), and the amount of vanadium in type 2 was smaller than that in type 1 (point 3).

For the effect of the minor elements on corrosion resistance, we tried to observe the distribution of the minor elements using electron probe microanalyzer (EPMA). It was found that the distribution appeared to be uniform, showing little enrichment of the minor elements in either the L1_2 phase or the mixed phase. This result would come from the fact that as shown in Figure 1, their microstructures were very fine with several hundreds nm diameter [21], and thus it was difficult to determine the enrichment site. Therefore, the difference in the corrosion resistance between type 1 and type 2 could not be explained only by the influence of minor elements. In addition, type 1 and type 2 showed the higher corrosion resistance in the HCl solution compared to $\text{Ni}_3(\text{Si},\text{Ti})$ and type 304. This suggests that the addition of

vanadium would inhibit the corrosion of type 1 and type 2 in the HCl solution and, however, enhance the corrosion in the H₂SO₄ and HNO₃ solutions. However, to clarify the effect of vanadium, further experiments must be conducted.

4. Conclusion

The corrosion behavior of the Ni₃Al/Ni₃V two-phase intermetallic compounds without the minor elements (type 1) and with them (type 2) in HCl, H₂SO₄, and HNO₃ solutions with 0.5 kmol/m³ has been studied and compared with that of the L1₂ single-phase Ni₃(Si,Ti) and austenitic stainless steel type 304. The following conclusions were obtained.

- (1) The type 1 and type 2 showed the higher corrosion resistance in HCl solution and the lower corrosion resistance in HNO₃ solution than Ni₃(Si,Ti) and type 304 in HCl and H₂SO₄ solutions.
- (2) Both type 1 and type 2 had the preferential dissolution of the mixed phase of L1₂ and D0₂₂ took place in all acidic solutions.
- (3) It was found that the corrosions of type 1 and type 2 were enhanced by the addition of vanadium in HNO₃ solution, while they were inhibited by vanadium in HCl solution.

References

- [1] Y. Nunomura, Y. Kaneno, H. Tsuda, and T. Takasugi, "Phase relation and microstructure in multi-phase intermetallic alloys based on Ni₃Al-Ni₃Ti-Ni₃V pseudo-ternary alloy system," *Intermetallics*, vol. 12, no. 4, pp. 389–399, 2004.
- [2] Y. Nunomura, Y. Kaneno, H. Tsuda, and T. Takasugi, "Dual multi-phase intermetallic alloys composed of geometrically close-packed Ni₃X (X: Al, Ti and V) type structures—I. Microstructures and their stability," *Acta Materialia*, vol. 54, no. 3, pp. 851–860, 2006.
- [3] W. Soga, Y. Kaneno, and T. Takasugi, "Phase relation and microstructure in multi-phase intermetallic alloys based on Ni₃Al-Ni₃Nb-Ni₃V pseudo-ternary alloy system," *Intermetallics*, vol. 14, no. 2, pp. 170–179, 2006.
- [4] S. Shibuya, Y. Kaneno, M. Yoshida, T. Shishido, and T. Takasugi, "Mechanical properties of dual multi-phase single-crystal intermetallic alloy composed of geometrically close packed Ni₃X (X: Al and V) type structures," *Intermetallics*, vol. 15, no. 2, pp. 119–127, 2007.
- [5] S. Shibuya, Y. Kaneno, H. Tsuda, and T. Takasugi, "Microstructural evolution of dual multi-phase intermetallic alloys composed of geometrically close packed Ni₃X (X: Al and V) type structures," *Intermetallics*, vol. 15, no. 3, pp. 338–348, 2007.
- [6] Y. Kaneno, W. Soga, H. Tsuda, and T. Takasugi, "Microstructural evolution and mechanical property in dual two-phase intermetallic alloys composed of geometrically close-packed Ni₃X (X: Al and V) containing Nb," *Journal of Materials Science*, vol. 43, no. 2, pp. 748–758, 2008.
- [7] W. Soga, Y. Kaneno, M. Yoshida, and T. Takasugi, "Microstructure and mechanical property in dual two-phase intermetallic alloys composed of geometrically close-packed Ni₃X (X: Al and V) containing Nb," *Materials Science and Engineering A*, vol. 473, no. 1-2, pp. 180–188, 2008.
- [8] T. Takasugi and Y. Kaneno, "Plasma-assisted surface modification of two-phase intermetallic alloy composed of Ni₃X type structures," in *Proceedings of the MRS Symposium*, vol. 1128, U06-04, 2009.
- [9] Y. Kaneno, N. Matsumoto, N. Tsuji, S. Tanaka, and T. Takasugi, "Plasma-assisted surface hardening of dual two-phase intermetallic alloy composed of Ni₃X type structures," *Materials Science and Engineering A*, vol. 516, no. 1-2, pp. 84–89, 2009.
- [10] K. Kawahara, Y. Kaneno, A. Kakitsuji, and T. Takasugi, "Microstructural factors affecting hardness property of dual two-phase intermetallic alloys based on Ni₃Al-Ni₃V pseudo-binary alloy system," *Intermetallics*, vol. 17, no. 11, pp. 938–944, 2009.
- [11] Y. Kitaura, Y. Kaneno, and T. Takasugi, "Effect of TiC addition on mechanical properties of dual two-phase Ni₃Al-Ni₃V intermetallic alloy," *Intermetallics*, vol. 18, no. 8, pp. 1623–1631, 2010.
- [12] Y. Kitaura, Y. Kaneno, and T. Takasugi, "Effect of NbC addition on mechanical properties of dual two-phase Ni₃Al-Ni₃V intermetallic alloy," *Materials Science and Engineering A*, vol. 527, no. 21-22, pp. 6012–6019, 2010.
- [13] K. Kawahara, T. Moronaga, Y. Kaneno, A. Kakitsuji, and T. Takasugi, "Effect of Nb and Ti addition on microstructure and hardness of dual two-phase intermetallic alloys based on Ni₃Al-Ni₃V pseudo-binary alloy system," *Materials Transactions*, vol. 51, no. 8, pp. 1395–1403, 2010.
- [14] R. Schafric and R. Sprague, *Advanced Materials Process*, vol. 162, pp. 27–30, 2004.
- [15] L. Y. Fang, G. J. Ting, and S. Y. Fu, *The Transactions of Non-ferrous Metals Society of China*, vol. 16, pp. 368–375, 2007.
- [16] C. T. Liu, E. H. Lee, and C. G. Mckamey, "An environmental effect as the major cause for room-temperature embrittlement in FeAl," *Scripta Metallurgica et Materialia*, vol. 23, pp. 875–880, 1989.
- [17] C. T. Liu and E. P. George, "Environmental embrittlement in boron-free and boron-doped FeAl (40 at. % Al) alloys," *Scripta Metallurgica Materialia*, vol. 24, pp. 1285–1290, 1990.
- [18] D. J. Duquette, *Intermetallic Compounds*, vol. 1, John Wiley & Sons, 1994.
- [19] G. Priyotomo, K. Okitsu, A. Iwase, Y. Kaneno, R. Nishimura, and T. Takasugi, "The corrosion behavior of intermetallic compounds Ni₃(Si,Ti) and Ni₃(Si,Ti) + 2Mo in acidic solutions," *Applied Surface Science*, vol. 257, no. 19, pp. 8268–8274, 2011.
- [20] D. Schlain, C. B. Kenahan, and W. L. Acherman, "Corrosion properties of high-purity vanadium," *Journal of The Less-Common Metals*, vol. 3, no. 6, pp. 458–467, 1961.
- [21] T. Moronaga, Y. Kaneno, H. Tsuda, and T. Takasugi, "TEM observation of the channel regions in a two-phase intermetallic alloy based on Ni₃Al-Ni₃V pseudo-binary alloy system," *Intermetallics*, vol. 21, pp. 80–87, 2012.

Review Article

Corrosion Protection of Steels by Conducting Polymer Coating

Toshiaki Ohtsuka

Faculty of Engineering, Hokkaido University, Kita 13-jo, Nishi 8-chome, Kita-ku, Sapporo 060-8628, Japan

Correspondence should be addressed to Toshiaki Ohtsuka, ohtsuka@eng.hokudai.ac.jp

Received 1 March 2012; Accepted 30 March 2012

Academic Editor: Rokuro Nishimura

Copyright © 2012 Toshiaki Ohtsuka. This is an open access article distributed under the Creative Commons Attribution License, which permits unrestricted use, distribution, and reproduction in any medium, provided the original work is properly cited.

The corrosion protection of steels by conducting polymer coating is reviewed. The conducting polymer such as polyaniline, polypyrrole, and polythiophen works as a strong oxidant to the steel, inducing the potential shift to the noble direction. The strongly oxidative conducting polymer facilitates the steel to be passivated. A bilayered PPy film was designed for the effective corrosion protection. It consisted of the inner layer in which phosphomolybdate ion, $\text{PMo}_{12}\text{O}_{40}^{3-}$ (PMo), was doped and the outer layer in which dodecylsulfate ion (DoS) was doped. The inner layer stabilized the passive oxide and the outer possessed anionic perm-selectivity to inhibit the aggressive anions such as chloride from penetrating through the PPy film to the substrate steel. By the bilayered PPy film, the steel was kept passive for about 200 h in 3.5% sodium chloride solution without formation of corrosion products.

1. Introduction

Since the investigation of Shirakawa et al. on conducting polyacetylene, various applications of conducting polymer have been reported [1]. Utilization of the conducting polymer for corrosion protection coating is one of these applications, and many papers have been presented in the last decade. Preparation of polyacetylene was made by oxidation in gaseous phase; however, at present, the conducting polymers such as polyaniline (PAni), polypyrrole (PPy), and polythiophen (Pthio) in Figure 1 for the corrosion protection have been prepared by electrochemical oxidation in liquid phase.

For application of the conducting polymer to corrosion protection, DeBerry was firstly reported in 1985, who presented that the stainless steel covered by PAni was kept in the passive state for relatively long period in sulfuric acid solution [2]. Wessling then pointed out that the conducting polymer coating of polyaniline and polypyrrole possibly possessed self-healing properties, in which the passive oxide between the substrate metal and the conducting polymer could be spontaneously reformed at a flawed site by oxidative capability of the conducting polymer [3].

When anodic potentials are applied to electrodes covered by the conducting polymers shown in Figure 1 after the polymerization, the oxidative property is provided in addition

to the conductivity. The ability of the conducting polymer to oxidize the substrate steels allows potential of steels to be shifted to the passive state, in which the steels are protected by the passive oxide formed beneath the conducting polymer. The application of the conducting polymer coating to the corrosion protection of steels was reviewed by Tallman et al. [4]. In this paper, the application of a bilayered conducting PPy to the protection of the steels is reviewed.

2. Conducting Polymer

Oxidative polymerization and the doping of anions into the polymer to provide the electronic conductivity have been reviewed by many authors, and here we briefly describe the process of PPy. When the electrode is anodically polarized in an electrolyte solution containing monomer of pyrrole (Py), the black polymer film can be formed on the electrode. The polymerization procedure is done without any difficulty, except for careful treatment of the electrolyte in which oxidation of the Py monomer by air should be avoided. The electrolyte should be thus deoxygenated by inert gas bubbling.

Figure 2 illustrates a model of the process for anodic polymerization of PPy proposed by Genies et al. [5]. Py monomer dissolved in the electrolyte donates an electron

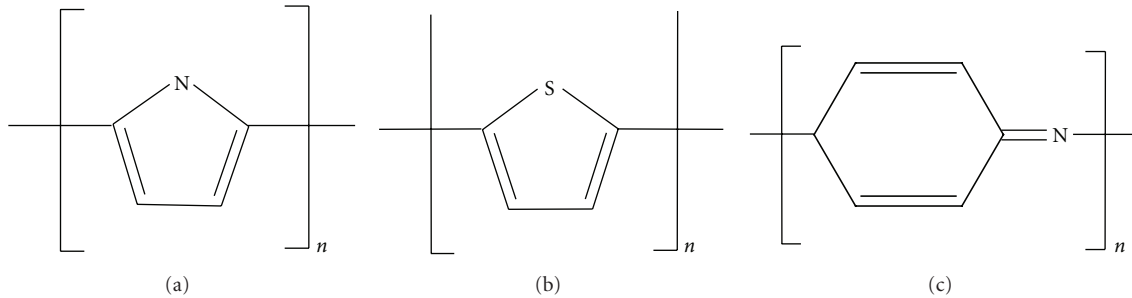


FIGURE 1: Typical conducting polymers: (a) polypyrrole (PPy), (b) polythiophen (PThio), and (c) polyaniline (PAni).

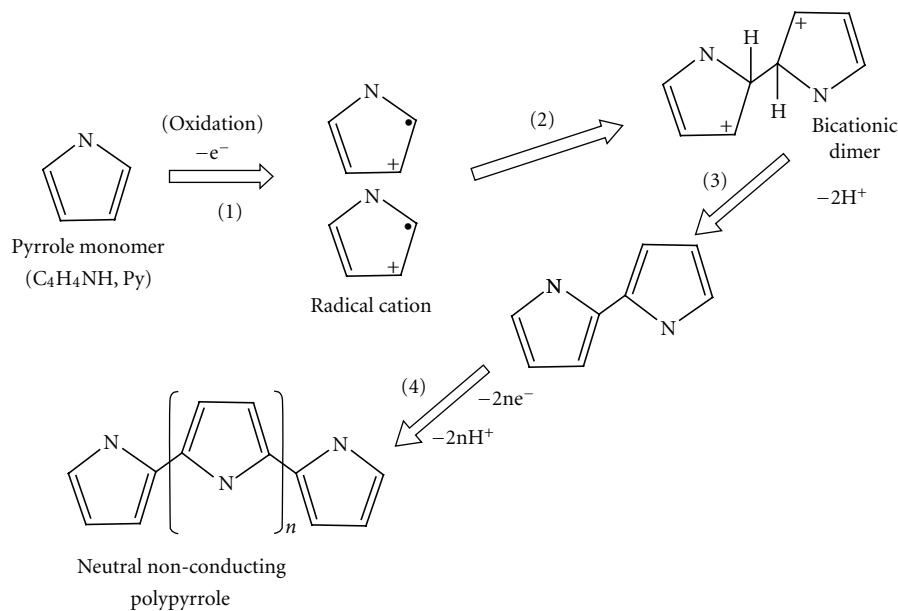


FIGURE 2: Electropolymerization process of PPy.

into the electrode, resulting in formation of a radical-cation pair (step (1)). The radicals in Py are reacted with each other and two protons are removed from the reacted Py pair (step (2)), forming a dimer of Py (step (3)). After the formation of the radical-cation pair and the reaction between the radicals are repeated, the black PPy film is formed on the electrode (step (4)).

The neutral PPy thus formed with a conjugated chain does not possess any conductivity. To add the conductivity into the neutral PPy, further oxidation is required as shown in Figure 3. When the anodic potential is applied to the electrode, an electron is removed from π electrons in the conjugated bond, yielding a pair of a radical and a positive charge (or cation) in the PPy backbone. This situation is called radical-cation state or polaron state. When the two radicals in the PPy are combined, the sites of single and double bond are replaced with each other and two cations remain in the PPy, the situation of which is called bication state or bi-polaron state. The cation thus formed in the PPy can move through π electron clouds, yielding electronic conductivity in the PPy backbone.

With the removal of electrons from the PPy backbone, insertion of anions from the environmental electrolyte solution occurs to maintain neutrality of the PPy layer; that is, when the neutral state of PPy changes to the oxidative state, removal of electrons and doping of anions simultaneously take place. It is assumed that one positive charge (or cation) can be inserted in three or four Py units at maximum. When more positive charge is added, the PPy changes to overoxidation state and loses the conductivity.

3. Corrosion Protection of Steels by Conducting Polymer of PPy

3.1. Mechanism of Corrosion Protection. For the corrosion protection, two mechanisms have been proposed; one is the physical barrier effect, and the other is anodic protection. On the barrier effect, the polymer coating works as a barrier against the penetration of oxidants and aggressive anions, protecting the substrate metals. This effect is similar to paint coating which inhibits the substances from penetrating to

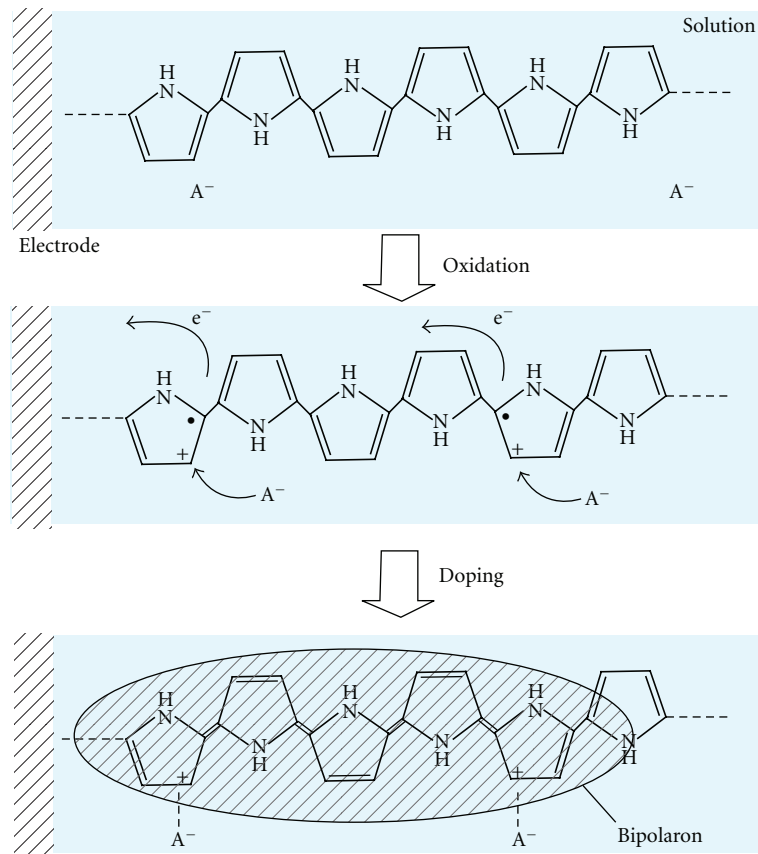
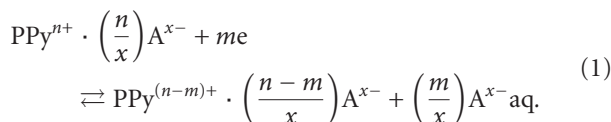


FIGURE 3: Electrochemical oxidation of neutral nonconducting PPy. During the oxidation, electron transfer from PPy to substrate steel and doping of anions from electrolyte solution to PPy simultaneously occur.

the substrate steel. On the anodic protection, the conducting polymer with the strongly oxidative property works as an oxidant to the substrate steel, potential of which is shifted to that in the passive state. In solution at neutral pH, the corrosion potential (or open circuit potential in corrosion) of bare steel is located in the active potential region and the corrosion rate of the steel is usually relatively high. Owing to the coating of conducting polymer, the maximum current in the active-passive transition region was limited by the barrier effect, and then the potential can be easily shifted to the higher potential in the passive state by the strongly oxidative property of the conducting polymer (Figure 4). In the passive state, the corrosion rate of steel becomes much lower. It is assumed that both the barrier effect and the oxidative property induce the anodic protection. Finally, the potential of the substrate steel may be in agreement with a redox potential of the PPy layer in the following reaction, and thus, depends on the degree of oxidation state of the PPy layer.



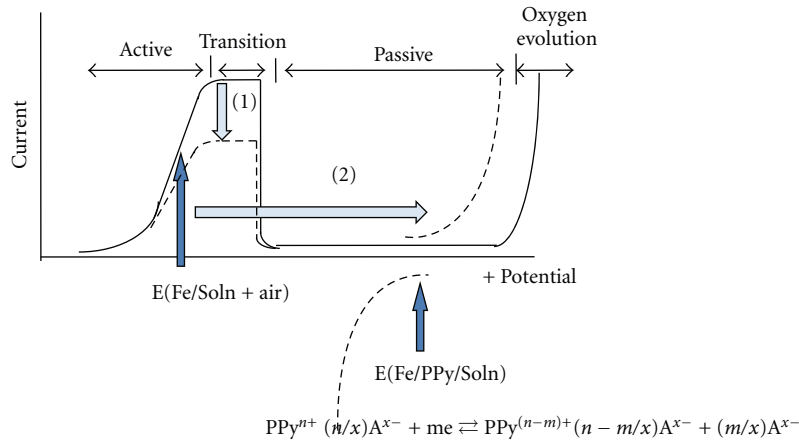
The conductivity of the PPy layer affects the oxidative power which brings about the passive state. If the coating layer has

little conductivity, the role of the coating as the oxidant is limited in the neighbourhood of the passive oxide. If the layer has enough high conductivity; however, the oxidant power of the whole layer is available and the power increases with the increase of the layer thickness.

The oxidation degree and the conductivity are assumed to decline with longer exposure to environment. If oxidants in the environment reoxidize the degraded PPy layer, the oxidation degree and conductivity can be recovered. When the oxidant in the environment, typically oxygen gas in air, can recover the PPy layer, the duration to maintain the oxidative power of the PPy layer can be prolonged and the passive state of the steel underneath the PPy layer can be kept for a longer period. The recovery process is illustrated in Figure 5.

3.2. Ion Exchange in the Conducting Polymer and Its Effect on Corrosion Protection.

In the anodic protection, the largest problem is breakdown of passive oxide due to the attack of aggressive anions such as chloride and bromide ions in solution and the breakdown is followed by a large damage of localized corrosion of pitting and crevice corrosion. As contrasted with the cathodic protection, there is a large risk of the localized corrosion connected with the anodic protection. When we control the doping ions in the PPy layer, we possibly prevent penetration of the aggressive anions into the



Role of oxidative-conductive polymer for corrosion prevention:

- (1) Suppression of active dissolution = barrier effect
- (2) Potential shift by oxidative polymer = anodic protection

FIGURE 4: Potential-current relation of steels covered by oxidative conducting PPy. A barrier effect of PPy suppresses active dissolution of the steel and an oxidative property of PPy shifts the potential into passive state.

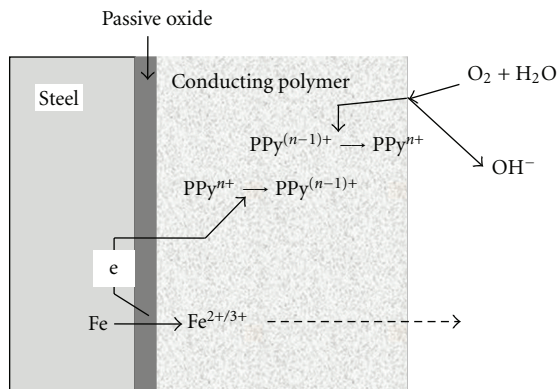


FIGURE 5: Degradation of oxidative property of PPy and recovery, which was done from reduction of oxygen on the PPy surface.

PPy layer. When the steels covered with the conducting PPy are immersed in the sodium chloride solution, the anions doped in the PPy can be exchanged with the chloride anions in the aqueous solution. The chloride anions penetrate the PPy to the substrate steels, and then induce the breakdown of the surface passive oxide film, followed by the pitting corrosion.

The mobility of the dopant anions in the PPy is affected by their mass and volume. When we adopted organic acid ions as the dopant ions in the PPy, they possessed enough large mass and volume to be immobile in the PPy. In general, organic acid anions with large mass are assumed to have small mobility and diffusion in the PPy layer. Accompanied with the oxidation and reduction of the PPy, small anions are doped into and dedoped out of the PPy, respectively, to maintain the neutrality, as described in reaction (1) and shown in Figure 6(a). When the mobility and diffusion of

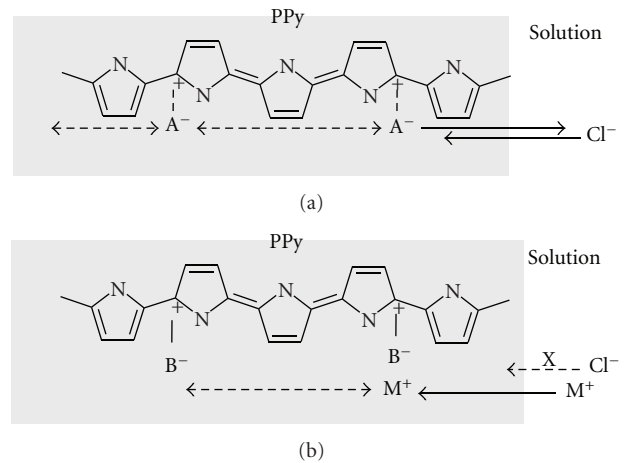
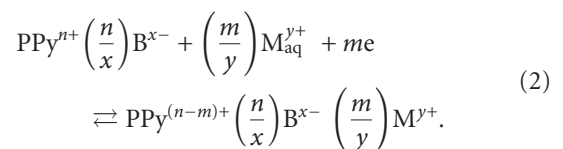


FIGURE 6: Ionic perm-selectivity of PPy film. (a) PPy film with anionic perm-selectivity, in which small-sized anions are doped in PPy and (b) PPy film with cationic perm-selectivity, in which large-sized anions are doped in PPy film.

the doped anions are restricted to small value, reversely, the cations are dedoped out of and doped into the PPy during the oxidation and reduction, respectively. The dedoping process of cations in the PPy during the oxidation and the doping during the reduction are described in the following reaction (2):



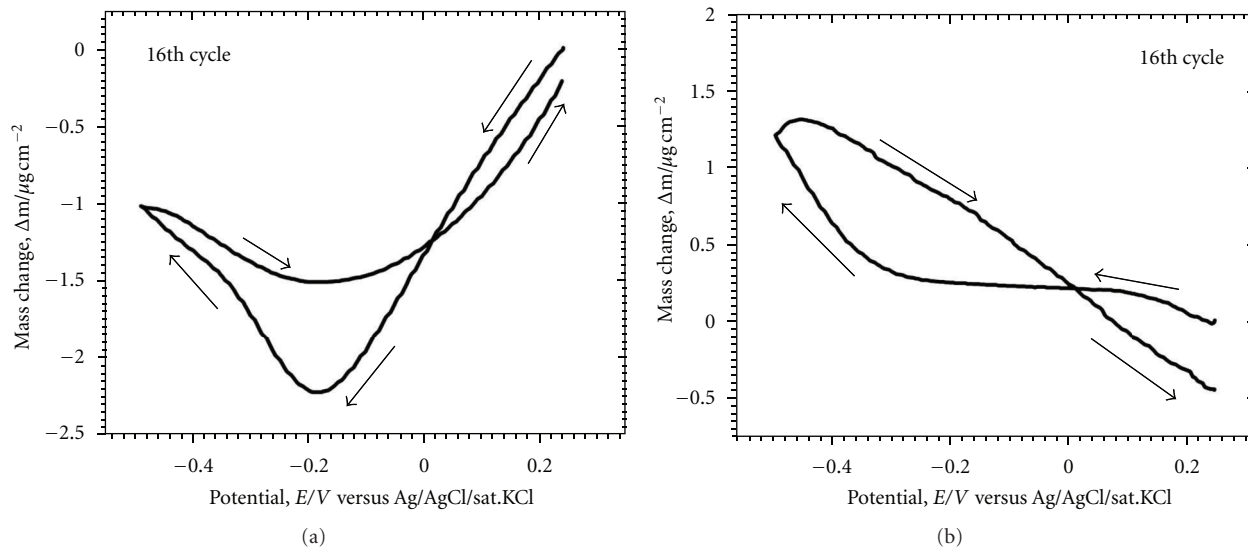


FIGURE 7: Mass change of the PPy-PMo layer and bilayer of PPy-PMo/PPy-DoS during the potentiodynamic reduction and oxidation in 3.5% NaCl solution. The data was a result of the 16th redox cycle.

When one considers the conducting PPy as a charged membrane, the immobile anions with large mass are assumed to have fixed sites with negative charge in the PPy. In the channel between the negatively charged sites, the cations can be mobile and the movement of the anions is greatly inhibited; that is, the membrane exhibits cationic permselectivity. As illustrated in Figure 6(b), under the situation where the dopant anions are large enough, the anions in the solution are excluded from the PPy and the substrate steel is protected against the pitting corrosion by chloride attack.

3.3. Design for Corrosion Protection by the PPy. The anodic protection greatly depends on the passivity and passive oxide on the steel. For the protection, the passivity and passive oxide must be kept stable. Further, the prevention of penetration of aggressive anions play an important role in the protection.

Deslouis et al. anodically prepared a PPy film on steel from an oxalate solution containing Py monomer and reported that the PPy layer protected the steel in sodium chloride solution for a long period [6–8]. They assumed that the ferric oxalate layer, which was formed underneath the PPy film by the polymerization, worked as a passivation film against corrosion. They also presented that the overcoat layer of PPy doped with dodecylsulfate, $C_{12}H_{25}OSO_3^-$ (DoS), anions was effective to the corrosion protection and that a bilayer coating of PPy-oxalate/PPy-DoS could maintain the passivation state for longer than 500 h, in which no corrosion products were observed.

DoS ion is a surfactant and forms micelle in aqueous solution at concentrations higher than critical concentration. Py monomers, which are probably incorporated in the micelle of DoS in aqueous solution, start to be polymerized when the micelles are collapsed on the electrode to which anodic potential is applied. DoS ions have relatively large masses and work as an immobile dopant in the PPy. The

PPy doped with DoS thus is considered as a membrane with negatively charged fixed sites and thus, with cationic permselectivity. The outer layer of PPy-DoS can, therefore, exclude the insertion of aggressive anions such as chloride ions.

In Figure 7 the mass change is plotted with anodic oxidation and cathodic reduction of a gold electrode covered with the PPy layers [9]. The mass change was measured by electrochemical quartz crystal microbalance (EQCM) with gold coating. The gold coating was covered by PPy doped with phosphomolybdate ions, $PMo_{12}O_{40}^{3-}$ (PMo) and a bilayered PPy of PPy-PMo/PPy-DoS. The mass change of the PPy-PMo film in Figure 7(a) indicates the uptake of mass during the oxidation and inversely, the removal during the reduction. The behaviour of the mass change during the oxidation reflects the removal of electrons from the PPy and simultaneous insertion of anions from the electrolyte to the PPy and viceversa during the reduction. When one introduces the outer layer of PPy-DoS, the mass change is inversely different from the above result, as shown in Figure 7(b). During the oxidation the mass increases and during the reduction it decreases. In PPy-DoS layer, in which negatively charged ions are fixed, the cations are mobile; during the oxidation the simultaneous removal of both electrons and cations from PPy and during the reduction viceversa. It can be understood that the PPy doped with DoS functions as a cationic perm-selective membrane.

Kowalski et al. designed the corrosion protection PPy layer of steels as following [9–14]. For the inner layer, the PPy was doped with PMo. PMo works as a passivator which stabilizes the passive state of steels and facilitates the formation of passive oxide. For the outer layer, the PPy doped with DoS was prepared. The outer layer can inhibit the anions from penetrating in the PPy layer. The results by Kowalski et al. are shown in Figure 8, [13] where the open circuit potential of the steel covered with the bilayered PPy is plotted during the immersion in 3.5% sodium chloride

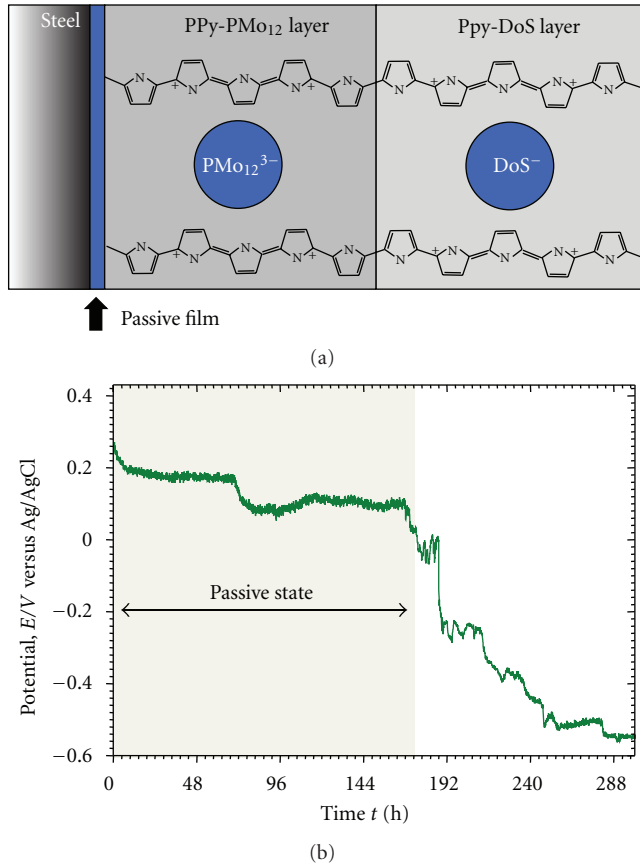


FIGURE 8: Model of bilayered PPy film and transient of open circuit potential of steel covered by the bilayered PPy in 3.5% NaCl solution.

solution. The steel covered with the bilayered PPy, about $5\ \mu\text{m}$ thick consisting of PPy-PMo/PPy-DoS exhibited the passivation for 190 h in which no corrosion products were observed. If the steel was covered with a single PPy-DoS layer of the same thickness, the passivation is kept for 10 h. It is assumed that PMo ion doped in the inner PPy stabilizes the passive oxide and helps the maintenance of the passive state of the substrate steel.

The design which combines the inner layer stabilizing the passive oxide with the outer later inhibiting anions from penetrating through PPy to the steel may be suitable to the corrosion protection of steel.

3.4. Self-Healing Property. In the corrosion protection, the coating must tolerate small defects to be considered as a suitable replacement for chromate-based coatings. We expect for the conducting polymer coating a self-healing property in which the passive oxide is spontaneously repaired after it develops small defects. On the chromate coating, the chromate ions dissolved from the coating oxidize the steel surface at the damaged sites to reform the passive oxide

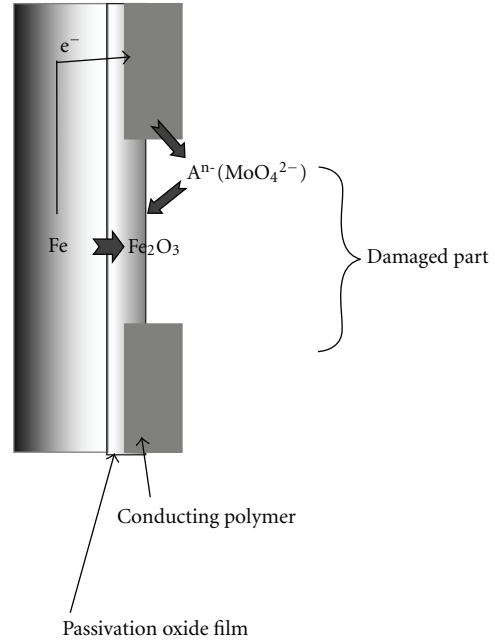


FIGURE 9: Schematic model of self-healing property of PPy-PMo₁₂/PPy-DoS bilayered PPy. Molybdate anions, dissolving from PPy film, reform a passive oxide at the damaged part.

A self-healing model proposed by Kowalski et al. is shown in Figure 9 for the bilayered PPy of PPy-PMo/PPy-DoS [9]. After the coating and passive oxide were locally flawed, PMo in the PPy layer is hydrolyzed and decomposes to molybdate and phosphate ions, and then both ions reach the flawed sites. The molybdate ions react with ferric ions on the flawed site to produce the ferric molybdate film. The salt film may be gradually changed to the passive oxide on the damaged site



Figure 10 shows the results reported by Kowalski et al. in which a small flaw was inserted by cutting knife in 2 h during the immersion in 3.5% sodium chloride solution [9]. After the PPy layer received the small flaw, the open circuit potential temporarily fell down. When the corrosion continues at the defect site, the potential will decrease to that of bare steel. The potential, however, rose up and recovered in the passive potential region. After that, the potential maintained the high potential in the passive region. When the flawed local site was measured by Raman scattering spectroscopy under this situation, the molybdate salt was detected [9]. It was found that a salt layer of ferric molybdate was reformed on the site.

4. Summary

Many papers on the corrosion protection by conducting polymer have been published since 10 years. In those,

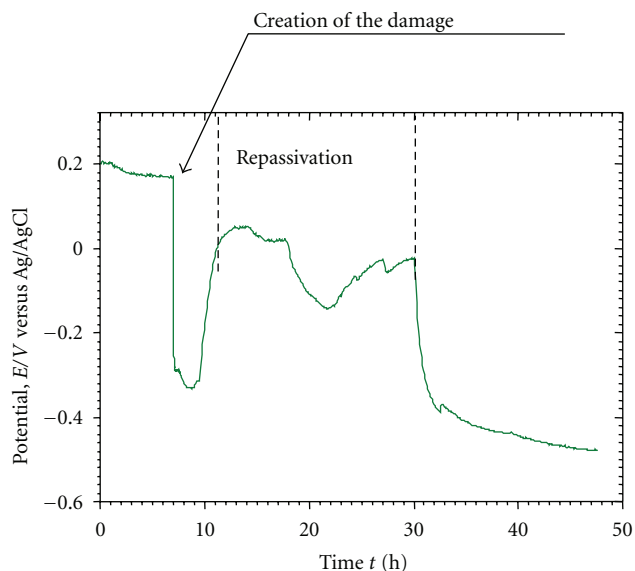


FIGURE 10: Potential change of steel covered by bilayered PPy film during the immersion in 3.5% NaCl solution. The damage was inserted on the PPy layer by a small knife in 7 h.

the attention was paid to how to form homogeneous and adherent layers of conducting polymer on steels and other metals. For the corrosion protection, we must consider the design of the conducting polymer. Since the corrosion protection by the conducting polymer is based on the anodic protection mechanism, we must consider how to stabilize the passive oxide underneath the polymer layer and how to inhibit the aggressive anions from penetrating the polymer layer.

Two mechanisms have been considered for the corrosion protection; one is physical barrier model and the other anodic protection model. We assume that the barrier effect suppresses the active dissolution of steel, facilitating the potential to be shifted in the passive region. The oxidative capability of the conducting polymer helps the potential shift and long maintenance of the passive state of the steel.

Our bilayered model, designed for the corrosion protection, includes two important factors: one is stabilization of the passive film on the steel by action of dopant ions in the inner PPy layer and the other is control of ionic permselectivity by organic acid ions doped in the outer PPy layer.

References

- [1] C. K. Chiang, C. R. Fincher, Y. W. Park et al., "Electrical conductivity in doped polyacetylene," *Physical Review Letters*, vol. 39, no. 17, pp. 1098–1101, 1977.
- [2] D. W. DeBerry, "Modification of the electrochemical and corrosion behavior of stainless steels with an electroactive coating," *Journal of the Electrochemical Society*, vol. 132, no. 5, pp. 1022–1026, 1985.
- [3] B. Wessling, "Passivation of metals by coating with polyaniline: corrosion potential shift and morphological changes," *Advanced Materials*, vol. 6, no. 3, pp. 226–228, 1994.
- [4] D. E. Tallman, G. Spinks, A. Duminis, and G. G. Wallace, "Electroactive conducting polymers for corrosion control:

- Part 1. General introduction and a review of non-ferrous metals," *Journal of Solid State Electrochemistry*, vol. 6, no. 2, pp. 73–84, 2002.
- [5] E. M. Genies, G. Bidan, and A. F. Diaz, "Spectroelectrochemical study of polypyrrole films," *Journal of Electroanalytical Chemistry*, vol. 149, no. 1-2, pp. 101–113, 1983.
- [6] H. Nguyen Thi Le, B. Garcia, C. Deslouis, and Q. Le Xuan, "Corrosion protection and conducting polymers: polypyrrole films on iron," *Electrochimica Acta*, vol. 46, no. 26-27, pp. 4259–4272, 2001.
- [7] N. T. L. Hien, B. Garcia, A. Pailleret, and C. Deslouis, "Role of doping ions in the corrosion protection of iron by polypyrrole films," *Electrochimica Acta*, vol. 50, no. 7-8, pp. 1747–1755, 2005.
- [8] T. Van Schaftinghen, C. Deslouis, A. Hubin, and H. Terryn, "Influence of the surface pre-treatment prior to the film synthesis, on the corrosion protection of iron with polypyrrole films," *Electrochimica Acta*, vol. 51, no. 8-9, pp. 1695–1703, 2006.
- [9] D. Kowalski, M. Ueda, and T. Ohtsuka, "Self-healing ion-permselective conducting polymer coating," *Journal of Materials Chemistry*, vol. 20, no. 36, pp. 7630–7633, 2010.
- [10] T. Ohtsuka, M. Iida, and M. Ueda, "Polypyrrole coating doped by molybdo-phosphate anions for corrosion prevention of carbon steels," *Journal of Solid State Electrochemistry*, vol. 10, no. 9, pp. 714–720, 2006.
- [11] D. Kowalski, M. Ueda, and T. Ohtsuka, "Corrosion protection of steel by bi-layered polypyrrole doped with molybdophosphate and naphthalenedisulfonate anions," *Corrosion Science*, vol. 49, no. 3, pp. 1635–1644, 2007.
- [12] D. Kowalski, M. Ueda, and T. Ohtsuka, "The effect of counter anions on corrosion resistance of steel covered by bi-layered polypyrrole film," *Corrosion Science*, vol. 49, no. 8, pp. 3442–3452, 2007.
- [13] D. Kowalski, M. Ueda, and T. Ohtsuka, "The effect of ultrasonic irradiation during electropolymerization of polypyrrole on corrosion prevention of the coated steel," *Corrosion Science*, vol. 50, no. 1, pp. 286–291, 2008.
- [14] D. Kowalski, M. Ueda, and T. Ohtsuka, "Self-healing ability of conductive polypyrrole coating with artificial defect," *ECS Transactions*, vol. 16, no. 52, pp. 177–182, 2008.

Review Article

Atomistic Modeling of Corrosion Events at the Interface between a Metal and Its Environment

Christopher D. Taylor

Materials Technology - Metallurgy (MST-6), Materials Science and Technology, Los Alamos National Laboratory, Los Alamos, NM 87545, USA

Correspondence should be addressed to Christopher D. Taylor, cdtaylor@lanl.gov

Received 30 November 2011; Accepted 7 March 2012

Academic Editor: Osama Alyousif

Copyright © 2012 Christopher D. Taylor. This is an open access article distributed under the Creative Commons Attribution License, which permits unrestricted use, distribution, and reproduction in any medium, provided the original work is properly cited.

Atomistic simulation is a powerful tool for probing the structure and properties of materials and the nature of chemical reactions. Corrosion is a complex process that involves chemical reactions occurring at the interface between a material and its environment and is, therefore, highly suited to study by atomistic modeling techniques. In this paper, the complex nature of corrosion processes and mechanisms is briefly reviewed. Various atomistic methods for exploring corrosion mechanisms are then described, and recent applications in the literature surveyed. Several instances of the application of atomistic modeling to corrosion science are then reviewed in detail, including studies of the metal-water interface, the reaction of water on electrified metallic interfaces, the dissolution of metal atoms from metallic surfaces, and the role of competitive adsorption in controlling the chemical nature and structure of a metallic surface. Some perspectives are then given concerning the future of atomistic modeling in the field of corrosion science.

1. Introduction to Corrosion Mechanisms

The following statement was made by Pletnev in regards to the corrosion of iron by chlorides in acidic media.

It is a common point of view that the chemical nature and structure of the surface of a metal, which is in contact with an electrolyte, are decisive in the kinetics of electrochemical reactions that proceed on this surface [1].

This “common point of view” is manifested in the great body of work in corrosion science that proposes mechanisms that explain how corrosion reactions occur (see, for instance, the monograph edited by Marcus) [2]. Corrosion in aqueous environments proceeds via an electrochemical mechanism, in which the coupled anodic and cathodic reactions take place at unique sites within the material/environment interface. The reactions themselves involve transfer of electrons or ions—often both—across the electrochemical double layer [3]. For this reason, the mechanisms via which corrosion

proceeds can be strongly influenced by perturbations in the surface and interfacial environment.

In many cases, the chemical reactions that together constitute a proposed mechanism or reaction scheme should be considered as placeholders: representative entities that subsume a host of microkinetic processes such as mass transport, surface adsorption and desorption, and bond-making/bond-breaking chemical reactions. Pletnev’s “chemical nature and structure” of the materials/environment interface are, in fact, rather complex quantities. Figure 1 contains an illustration that presents, schematically, some of the important elements of this interface and the processes relevant to corrosion [4].

Important classes of variables that impact the process and nature of corrosion in a material include the temperature, local environment, and the stress on the material. Environmental factors may include flow rates, pH, and speciation [5, 6]. The nature of the electrolyte is also significant: different corrosion mechanisms may be favored when the electrolyte is changed [7]. The conductivity of the electrolyte also affects the Ohmic drop in potential between the cathodic

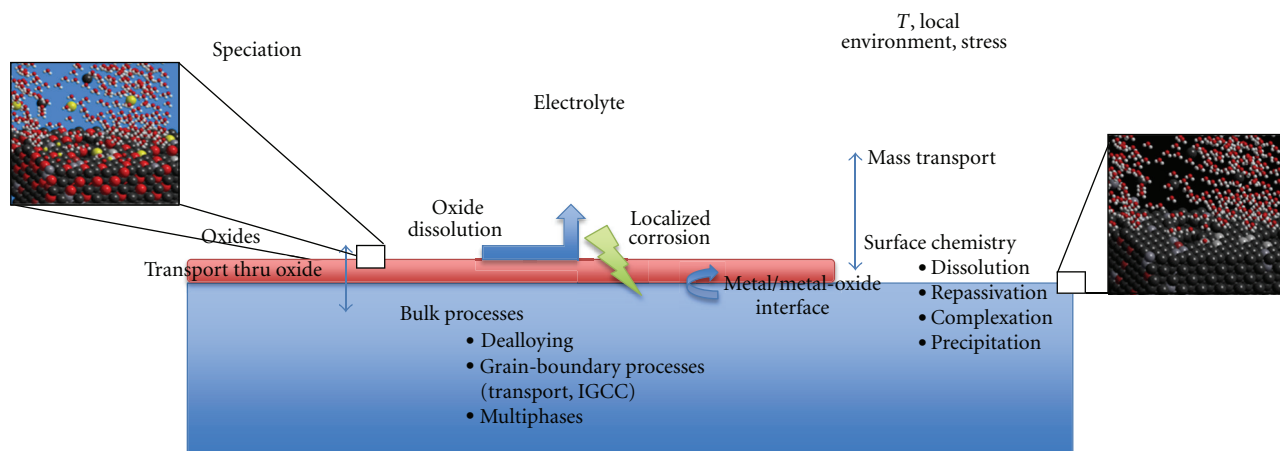


FIGURE 1: Schematic of the materials/environment interface. Features relevant to corrosion are labeled. Reproduced from [4].

and anodic reaction sites in situations such as crevice corrosion and pitting [8]. Mass transport processes at the interface often define the kinetics of corrosion reactions. These processes may occur across a hydrodynamic boundary layer, through an oxide film, or involve migration of species within the metallic component [9–13]. Each of these rates may be corrosion limiting. The microstructure of the metal itself can have important consequences for the process of corrosion. Corrosion may be intergranular, in which case corrosion occurs preferentially at the grain boundaries [14–17]. Crystallographic pitting has been observed in some cases, where the corrosion morphology reflects the crystallographic order of the material substrate [18, 19]. Galvanic coupling can occur between precipitates in the material and the bulk matrix [20], and stress-corrosion cracking pathways may be controlled by microstructural effects and phase distributions [21]. Grain boundary engineering has, in some cases, been employed to optimize corrosion resistance of certain materials [17, 22, 23].

While not comprehensive, the above list serves to illustrate that corrosion rate is a highly nonlinear function of multiple materials and environmental variables. This nonlinearity is, ultimately, the reason why, for some scientists and engineers, corrosion science presents such a rich and complex field of study.

2. Atomistic Models

Scientists working in the fields of surface science and solid-state physics have made it possible, in recent years, to directly simulate interfacial reactions with atomistic resolution using electronic structure methods or interatomic potentials, finding particular applications in the design and modeling of heterogeneous catalysts [24–26]. Whereas heterogeneous catalysis might be described as the deployment of a material to manipulate its environment, corrosion is the inverse process: the modification and depletion of a material by its environment. The deterioration of a solid-state material as a consequence of its interactions with a fluid phase, however, involves processes that are typically slower and involve

higher-energy transition states than the catalysis of a molecular transformation by a substrate [27]. Although it is not, at the present time, possible to include all of the elements contained within Figure 1 within some massively parallel computational simulation of corrosion (although for some particular mechanisms and materials this has been attempted) [28, 29], it is possible to deconstruct certain elements deemed to be critical within a given application. For instance, in cases of localized corrosion or corrosion cracking, one may focus on the chemistry occurring at a bare-metal/solution interface [30–32]. In cases where oxide growth is relevant, one can focus on ensembles that consist of defect states in the oxide material [33, 34]. It is also possible to look at dissolution processes from oxide surfaces or to interrogate questions regarding bulk or surface thermodynamic stability [4, 35, 36]. The field of computational materials science is currently growing such that, by coupling continuum kinetic or fracture mechanics models with atomistic scale codes or phase-field theory, it may soon be possible to realistically simulate increasingly comprehensive portions of Figure 1 [28, 29, 37]. The list of examples and references provided in this section should by no means be considered comprehensive, but it is an attempt to capture recent efforts, as well as historical modeling studies that are relevant to scientific studies of corrosion phenomena conducted in the present research group.

Atomistic modeling techniques can, at present, be grouped into four main categories: molecular modeling, static band-structure calculations, molecular dynamics, and Monte Carlo methods [38–40]. Molecular modeling encompasses the field of (generally) small-molecule calculations [40]. Molecular orbital theory is used to solve the electronic structure problem, which in turn allows access to molecular properties, such as HOMO-LUMO (highest occupied and lowest unoccupied molecular orbitals, resp.) gap, bond lengths and bond angles, and energetics of reactant, intermediate, transition, and product states. Extensions of molecular orbital theory allow, for example, the modeling of cationic states of metals when dissolved in solution phase [41, 42], the study of metallic nanoparticles [43], investigations of

bonding of water and oxygen to metal atoms and clusters [44, 45], and the evaluation of molecular properties of chemical inhibitors [46, 47].

Static band-structure calculations are drawn more from the fields of density functional theory and solid-state physics [48]. These calculations were originally developed to evaluate the properties of solids, in a similar way to how molecular orbital theory calculations are used to evaluate the properties of molecules. From a reaction point of view, the electronic and atomistic properties of reactant, product, intermediate, and transition states can also be evaluated using these methods, allowing insights to be gained regarding rate-limiting steps, for example, in mass-transport processes such as solid-state diffusion [49–51] or phase transformations [52]. These techniques can be extended to look at surfaces as well, as has been applied heavily in the field of heterogeneous catalysis [24] and electrocatalysis [25], and, more recently, to problems in corrosion [35, 53–57]. This technique, as well as molecular modeling, is limited primarily by the computational cost of performing such calculations. Ensembles containing small numbers of atoms, either isolated as a cluster in space or in cells with periodic boundary conditions, must therefore be carefully constructed to imitate the system one is trying to model, and the appropriate caveats should be given regarding artifacts that may be induced by these idealized conditions. Furthermore, the inability to readily incorporate dynamic effects means that reactions which require significant thermal reorganization—such as the formation of solvation shells around ions during a dissolution event—may be difficult to capture reliably. Overall, however, these methods can be powerfully applied to interrogate detailed, atomistically resolved reaction mechanisms and mass transport processes relevant to corrosion. Their dependence upon electronic structure evaluation makes them the most flexible and reliable, in terms of fundamental, deterministic physics but, at the same time, makes them exceedingly expensive in terms of computational cost and user time.

Molecular dynamics simulations can be used to simulate reaction events, particularly those involving high energy or thermally stimulated processes. While simulations using electronic structure techniques to evaluate the forces on atoms and their thermal trajectories can be performed, the cost of such methods is usually far too high to enable useful time scales to be reached within the scope of the simulation. Therefore, modelers employing molecular dynamics will typically apply interatomic potential techniques. These techniques employ simple algorithms for evaluating forces on atoms as a function of their relative positions in space, for example, the embedded atom method [58–60]. Based on this technique, one can simulate the evolution of corrosion morphologies, diffusion processes in materials, the behavior of defects in materials, such as grain boundaries, and the rates at which oxidation or other processes occur. Examples include the oxidation of aluminum and zirconium metals [28, 34], the structure of the metal/water interface [61–69], and the evolution of radiation damage effects in nanolayered materials [70].

Kinetic Monte Carlo simulations go beyond dynamic effects but utilize atomistically determined information for the rate constants of fundamental atomistic and molecular transformations to perform stochastic updates to the state of a system, which, in this context, may be considered its atomistic configuration [71, 72]. This method, therefore, is not limited to dynamic time scales but, instead, depends on the accuracy of the rate information passed to the model from lower length scale models. These models have been applied to look at atomic and molecular arrangements of adsorbates on metal surfaces [73] and growth of molecular films [74], as well as to bimetallic dissolution problems [75–77]. Monte Carlo models can also be applied to search for equilibrium structures, such as crystallographic pitting morphologies or defect clusters in materials such as metals and oxides [78, 79].

In the following, several applications of atomistic modeling to understand the details of various corrosion reactions are reviewed, drawing primarily upon studies performed within our research group. The paper concludes with a perspective on the state of contemporary modeling in corrosion research and some statements concerning our expectations for the future of this field.

3. Electrochemistry of Water on Metallic Surfaces

The structure of water molecules on metallic surfaces has been studied by various experimental and theoretical methods [80, 81]. One detail that has emerged from these studies is that liquid water tends to be more structured at the interface, due to the necessity for water molecules to arrange in such a way to preserve hydrogen bonding characteristics, despite the discontinuity presented by the interface [63, 81–83]. Additionally, metal-water interactions may impose their own preferences/constraints on the interfacial structure of water [84, 85]. A common model that has been adopted by modelers and experimentalists alike is the “bilayer” [86]. In this structure, water molecules adsorb at atop sites on the metal surface via donation of electron density from the lone pair on oxygen to the frontier orbitals or “dangling bonds” of the surface metal atoms. A second layer of water molecules arranges on the surface in such a way as to form hexagonal overlayer hydrogen bonded to the water molecules directly bound to the surface. Molecular dynamics simulations have suggested that such networks are rather stable on many metallic surfaces, and this general picture has been supported by neutron diffraction experiments [63, 82, 83].

In a work we recently performed to examine the role of ordering of water molecules in crack tips, motivated by the observation of fast transport of ions to the crack tip during stress-corrosion cracking [87], we utilized the *ab initio* molecular dynamics technique to examine the emergence of water structure on the Ni(001) surface [88]. A short molecular dynamics simulation was performed using density functional theory and the Hellman-Feynman theorem to determine forces on the atoms [38]. The code VASP was used to perform these simulations [89–93]. The simulation was

short in the sense that only a few picoseconds of time could be simulated, whereas estimates of 100 ps for water equilibration in supercell molecular dynamics simulations have been given in the literature [94]. The simulations are performed using three-dimensionally periodic supercells. This geometry allows the band structure of the exposed Ni(100) surface to be modeled realistically, as well as for bulk water to be imitated in the periodic ensemble. The periodicity in the direction normal to the slab means that the simulation is actually considering an array of nickel slabs, spaced about 2 nm apart. Similar choices are often made when simulating surface chemistry, as the slabs are usually spaced far enough apart to avoid direct interactions. However, in the case where the environment may possess some ordering, we may expect that the interaction between slabs could become more significant. In this way, the simulation we are performing is somewhat imitative of the situation in which there is a tight 2 nm width crack front.

Over the course of the molecular dynamics simulation, the position of the oxygen atoms was monitored to look for evidence of structure, as opposed to homogenization, across the entire volume of the fracture space. The probability distribution for oxygen atoms obtained from the molecular dynamics simulation is reproduced here in Figure 2. Similarly to the previous findings cited above, water molecules show some ordering in the region close to the metal. This ordering can be discerned by the presence of pronounced peaks in the distribution function of oxygen close to the interface. Since the slab spacing is small in this simulation (2 nm, or enough for 5 water layers), the ordering appears to persist throughout the entire region of the simulation cell. This result implies that a 2 nm crack is sufficiently narrow to confine the water molecules in such a way as to enforce certain “packings” of the water molecules. From a surface point of view, the results suggest that some ordering of water molecules may be expected to occur for a distance of up to 1 nm from the metallic surface. This ordering of water molecules will have implications for the diffusion of ions and molecules along surfaces, such as the newly formed surfaces that grow during a cracking event, or penetration along internal cracks in a substance.

In addition to organizing into “ice-like” configurations, water molecules have the opportunity to react on metal surfaces to form hydrided surfaces, oxidized surfaces, or hydroxylated surfaces [95]. The nature of this reaction is strongly dependent on the identity of the metal, as well as the electrochemical potential. For instance, as the electrochemical potential is made cathodic, the Fermi level of the metal is raised, which makes electron transfer to the protons in water to become more favorable, leading to the formation of atomic hydrogen via the mechanism:



On the other hand, making the surface more anodic depletes electrons from the metal, lowering the Fermi level

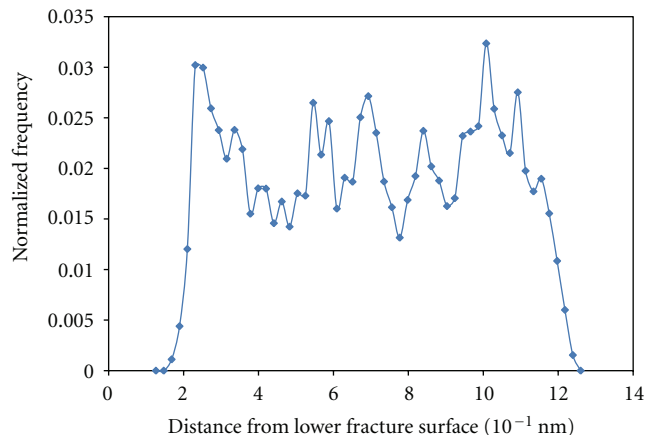
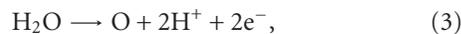
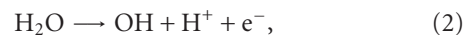


FIGURE 2: The ordering of water molecules during molecular dynamics simulation of the region in between the two Ni(100) fracture surfaces exposed to water. The normalized frequency refers to the frequency with which oxygen may be found at a given distance from the electrode surface, normalized such that the integrated frequency goes to unity.

and thus making the metal a good electron acceptor. Hence, such reactions as



become energetically favorable.

In previous work, we developed a methodology for simulating the electrochemical double layer in density functional theory models of interfaces [96]. Using this method we were able to predict the potentials at which hydrogen, water, hydroxide, and oxygen are stable species on metallic surfaces, such as Ni(111) [30, 31]. These predictions are represented in Figure 3, which plots the free energy for each of the possible surface phases (OH, O, H, and H₂O) that may be produced when water reacts with a metallic surface. The free energies are obtained by computing the energy of slab models for the surface that consist of several layers of Ni(111) planes, exposed to a supercell of water molecules, in addition to the adsorbed surface phase. The energies are corrected for the electrochemical potential using the method cited above [96]. The results correlated well with experimental determinations for the onset of oxidation of the metallic surfaces [97].

We also used the same technique to directly evaluate the nature of bonding between copper and hydroxide [98]. We found that, even when significant changes in the electrochemical potential were made, the overall binding energy did not change significantly, and this was attributed to the fact that, when the Fermi energy of the metal was raised or lowered in response to changes in the applied potential, the orbitals of the bonding hydroxide species tended to follow. The adsorption geometry, on the other hand, did change significantly, with rotation of the OH dipole moving in such a way as to counteract the electric field across the double layer. The binding of water, on the other hand, does

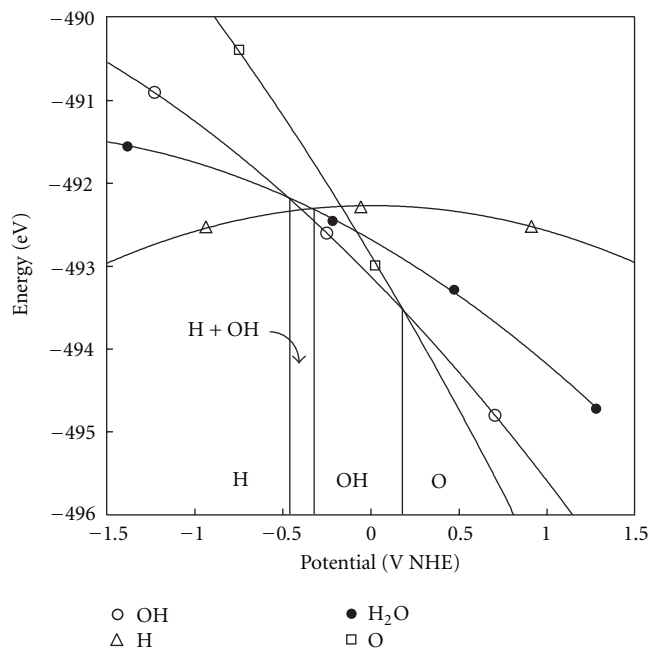


FIGURE 3: Phase diagram for surface hydride, molecular water, hydroxy and oxy species on Ni(111) at pH 0. Reproduced with permission from [30].

change more significantly, because the orbitals on water molecules are engaged much more weakly with the frontier orbitals on the metal surface; the metal-oxygen bond in the chemisorption of water is such that the highest occupied molecular orbitals on the water molecule are beyond the range of the electrochemical double layer. This relationship between the electronic structure of the metal (FERMI and D in Figure 4) and the hydroxyl molecular orbitals (S1 and P11, P12, P13 bands in Figure 4) and the water molecular orbitals (S2, P21–P24 in Figure 4) is shown as a function of the applied surface charge in Figure 4. It can be seen that the energy levels of the hydroxyl, which is bonded to the surface, closely track the Fermi level of the metal, whereas the energy levels associated with the water molecule are only weakly correlated.

In the same study we tracked the change in the OH geometry as the potential was made more anodic. During this process, the proton of the adsorbed OH begins to transfer to the second layer of H₂O close to the interface, tending towards the formation of H₃O⁺ and an adsorbed O species (an important step in surface oxidation by H₂O). One consequence of this OH-H₂O adduct formation is an increase in the capacitance of the system due to the delocalization of positive charge across the first “inner-layer” of the solution environment. These simulations represent prepassive chemistry: events that will occur prior to, or during, the formation of passive oxide layers on nickel and copper metal.

In a related study, a series of geometry optimizations was performed for a model Cu(111)-H₂O interface, with the potentials made successively more anodic at each step [99].

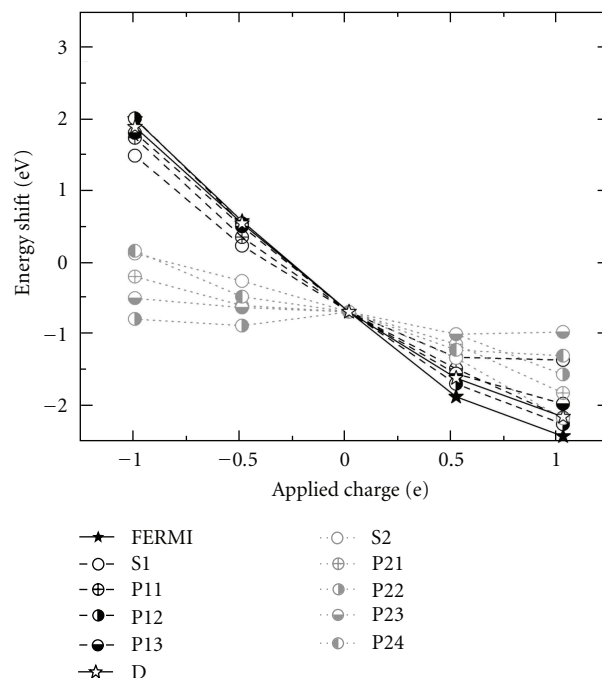


FIGURE 4: The shifts in energy of the Fermi level, copper d-band center (D), s and p bands of the oxygen of adsorbed OH (black symbols, dashed lines, S1, P11, P12, P13), and s and p bands of the oxygen of first-layer water molecules (gray symbols, dotted lines, S2, P21, P22, P23, P24) relative to the zero-charge values. Reproduced with permission from [98].

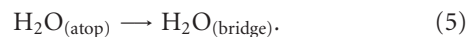
The model was, therefore, set up in an equivalent way to a cyclic voltammetry experiment, although kinetic processes were not explicitly taken into account. When the resulting geometries were plotted, it could be seen that, given a threshold surface charge density, phase transitions on the surface could be expected to emerge. These began with the simple water dissociation reactions, described above, but ultimately led to destabilization of the metallic copper surface and place exchange between the electron-rich oxygen species and the electron-depleted copper atoms. This series of phase transformations is plotted in Figure 5.

The stepwise charging of the model system and subsequent relaxation of the atomic structure prompted the following structural changes (Figure 5).

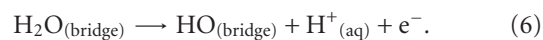
- (a) Chemisorption of H₂O to the atop site of a Cu atom:



- (b) Migration of H₂O from the atop site to a bridge site:



- (c) Deprotonation of the bridging H₂O to form OH_{ads} + H⁺_{aq} + e⁻:



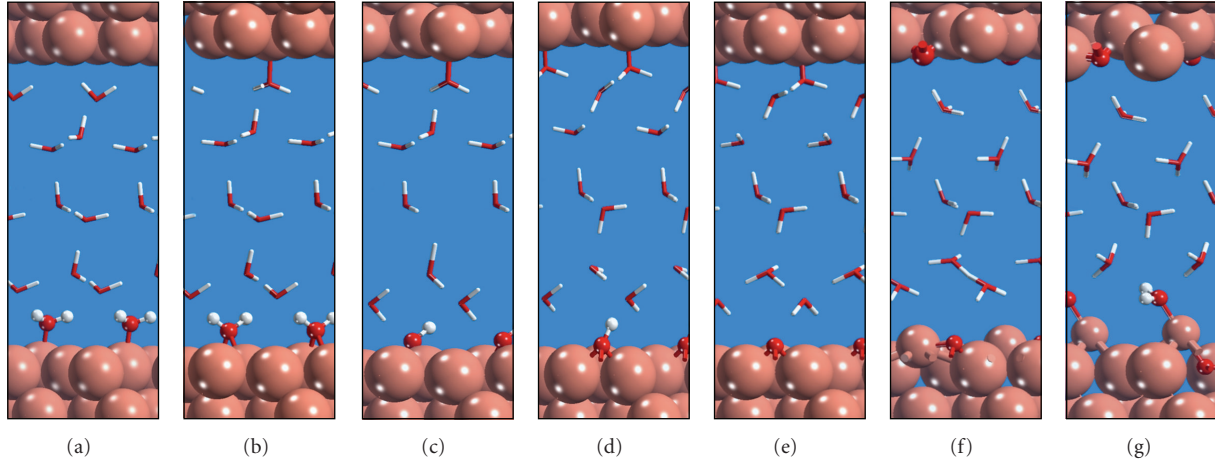
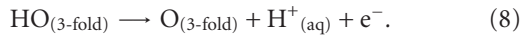


FIGURE 5: Charge-induced reaction sequence for the activation and migration of H_2O (a)–(c), OH (c)–(e) and O (e)–(g) on $\text{Cu}(111)$, followed by oxidation of Cu (f)–(g) effected by adsorbed oxygen [99].

- (d) Migration of the bridging OH to the threefold hollow site, consistent with the emergence of a second type of OH resonance in the surface enhanced resonance spectrum recorded by Niaura [100]:



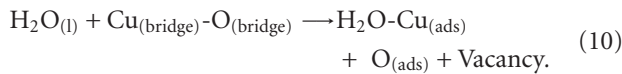
- (e) Deprotonation of OH_{ads} to form $\text{O}_{\text{ads}} + \text{H}^+_{\text{aq}} + \text{e}^-$:



- (f) Surface reconstruction by eruption of a Cu adatom from the surface layer. Adsorbed oxygen acts as a tether:



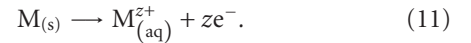
- (g) Complete displacement of the copper adatom by oxygen, resulting in a Cu_2O -like adlayer, in which O is adsorbed at the vacancy site left by the Cu atom, and this partially adsorbed Cu atom is now coordinated to H_2O , according to the reaction:



We have since generalized this work to a larger range of transition metals using a simplified version of the technique that does not require polarization of the interfacial cells but simply shifts the free energy of electrochemical reactions by an energy term $nF\Delta U$ [32]. This method works most simply when the transfers of an electron and proton occur simultaneously, as in the reaction schemes presented above, as these energies can be related to the energy of H_2 for a reference potential of the standard hydrogen electrode. The utility of this method to capture the leading terms for the free energy changes of electrochemical reactions was demonstrated in a joint paper between our research group and that of Rossmeisl and Nørskov [101].

4. Dissolution of Metal Atoms

Having demonstrated the capability to model the electrochemical reactions involving water on bare metal surfaces, we moved on to consider what is perhaps the quintessential reaction in any aqueous corrosion scheme—the dissolution event itself. This reaction is typically expressed by the chemical equation:



The above chemical equation highlights a tension between the forces of metal-metal bonding and the formation of bonds with species present in the aqueous solution. An analysis of the complexity contained within this tension was recently made through a series of papers published by Gileadi [27, 102, 103]. To understand how theoretically challenging this concept is, consider that molecular water is bound to transition and noble-metal close-packed surfaces by energies no more than a few tenths of an eV [104], whereas the surface cohesive energies are an order of magnitude greater [105]. The reason that such dissolution events do occur, on a regular and (from a corrosion mitigation perspective) inconveniently frequent basis, is that electric fields at the interface (of order $0.1 \text{ V}/\text{\AA}$) provide a gradient sufficiently strong enough to stabilize the formation and extraction of that metal atom in its ionic form [102].

One way to interrogate this process via atomistic simulation is to begin by simply considering the role of metal-metal bonding in controlling corrosion morphologies. This issue has been addressed previously to some extent via kinetic Monte Carlo simulations of the dealloying of binary alloy systems and of crystallographic pitting [75, 76, 106]. We recently published work on Fe-Tc systems, showing how the degree of local coordination and local composition affect metal atom cohesive energies [4]. It was shown in that work that the number of nearest neighbors alone was insufficient, however, to capture the strength of these interactions, but that the organization of these neighbors was of great

significance. We performed a similar study on nanoparticles, close-packed and stepped surfaces of copper, and showed that generally surface cohesive energies correlated linearly with the number of nearest neighbors, but significant noise existed in this correlation such that individual topological features must indeed be taken into account [105].

Because it is fundamentally challenging to directly model the interplay between metal-metal cohesion and metal-solvent attraction using typical materials dynamics simulation techniques (such as embedded atom potentials) [107–110], we decided to build a model system that could explore aspects of the dissolution reaction using highly controlled, density functional theory calculations [111]. The model we built to study this system consisted of a Cu nanoparticle, with a single Cu adatom adsorbed on the surface in contact with a hemispherical “nanodroplet” close to a dozen water molecules (see Figure 6(a)). The metal particle was designed to be large enough to provide a fair representation of metal-metal bonding and electronic band structure, and the solution model is sufficient to model one to two layers of an emerging ion’s solvation sheath. The configuration of the solvent molecules was obtained by performing a quantum mechanical molecular dynamics simulation at 300 K and then cooling the system to an annealed configuration, which was governed by the hydrogen bonding between water molecules and their interactions with the metal particle. We then performed a series of geometry optimizations, similar to what had been performed for water molecules on Cu(111) surfaces in the study mentioned above, but rather than varying the system charge state, we varied the height of the metal atom above the particle surface stepwise.

To understand some of the mechanistic details of the study we performed the simulation under three separate sets of conditions (no water, water, and water plus an applied electric field, thus simulating a double layer). We plotted the charge states of the adatom as a function of the height above the surface (or, equivalently, as a function of the dissolution process), as well as the associated energies (Figures 6(b) and 6(c), resp.).

In the absence of solvent, the energy of the adatom appears to rise in a quasi-harmonic way, which will at some point vary from harmonicity and tend asymptotically to the value for the surface-binding energy of the adatom. There is some weak charging of the surface adatom. When the solvent molecules are present, the charge on the adsorbed copper atom is significantly more cationic. The Bader method yields a charge of +0.36 for the copper adatom in the solvent phase, even before dissolution occurs. Thus water molecules appear to “pre-charge” adsorbed metal atoms on the surface, as they form a partial solvation shell around the adatom. As the bond is broken (due to raising of the surface metal atom), the energy increases, as does the charge. Furthermore, the copper atom begins to form more and more bonds with the surrounding water molecules, eventually obtaining a rudimentary solvation shell.

The early part of the energy-distance curve, for distances less than 1 Å, is not so different from the case of the vacuum or “no solvent.” It appears that *the energy in the early stages of dissolution is mostly concerned with the strong effect of*

breaking bonds with the metal surface. In the latter part of the curve, for distances greater than 1 Å, the formation of bonds with the solvent environment alleviates the high energies incurred when the metal-surface bond is broken, in agreement with the “make-before-break” argument as posed in the manuscript by Gileadi [102]. The development of what appears to be a +1 charge on the Cu ion may be an indicator that the +1 state develops first, and then transition to +2 takes place as an outer-layer, electron-transfer event. The application of the electric field further lowers the energy trajectory of the dissolving ion.

5. Surface Chemistry Control of Corrosion Processes

Although water chemistry and bare-metal dissolution remain important focus areas for the development of our understanding of corrosion mechanisms, in many cases corrosion takes place in more complex media. For instance, in the oil and gas industry, it is known that numerous corrosion processes take place simultaneously, and, depending on the local conditions, one or other of these processes will be dominant at a given location [112]. Documented corrosion mechanisms that occur during crude oil refining operations include ammonium-chloride corrosion, ammonium bisulfide corrosion, high-temperature sulfide corrosion, cyanide accelerated corrosion, or stress corrosion cracking that may be brought on by hydrogen, chloride, sulfide, or carbonate [112].

Recently, we embarked upon a study of ammonium chloride corrosion mechanisms, focusing on the surface adsorption processes associated with this reaction scheme [113]. Ammonium chloride corrosion occurs when conditions in the process stream are such that the ammonia and hydrogen chloride in the vapor phase crystallize as hygroscopic NH_4Cl particulates and interact with condensed water vapor to form highly saturated chloride solutions attended by aggressive corrosion behavior [112, 114, 115]. It was demonstrated by Shimbarevich and Tseitlin that increasing the chloride content for a given NH_3 concentration can cause enhanced corrosion, and it was suggested that this occurs due to adsorption of chloride ions on the surface and the subsequent enhancement of anodic dissolution process [116]. At the same time it was shown that increasing the NH_3 concentration made the solution more basic, thus favoring OH adsorption on the surface, as opposed to Cl adsorption and hence hastening passivation [117].

In order to begin to understand the significance of surface processes to the corrosion mechanism occurring when mild steel is exposed to ammonium chloride and to attempt to evaluate these mechanisms that are driven by consideration of surface processes, we applied the techniques we had developed for water-metal interfaces to a more complex mixture of reactive species. In particular, we modeled the competitive adsorption of NH_x , OH_x , H, and Cl species on an exposed Fe(110) facet as a function of the local electrochemical potential. The relevant phase diagram, computed

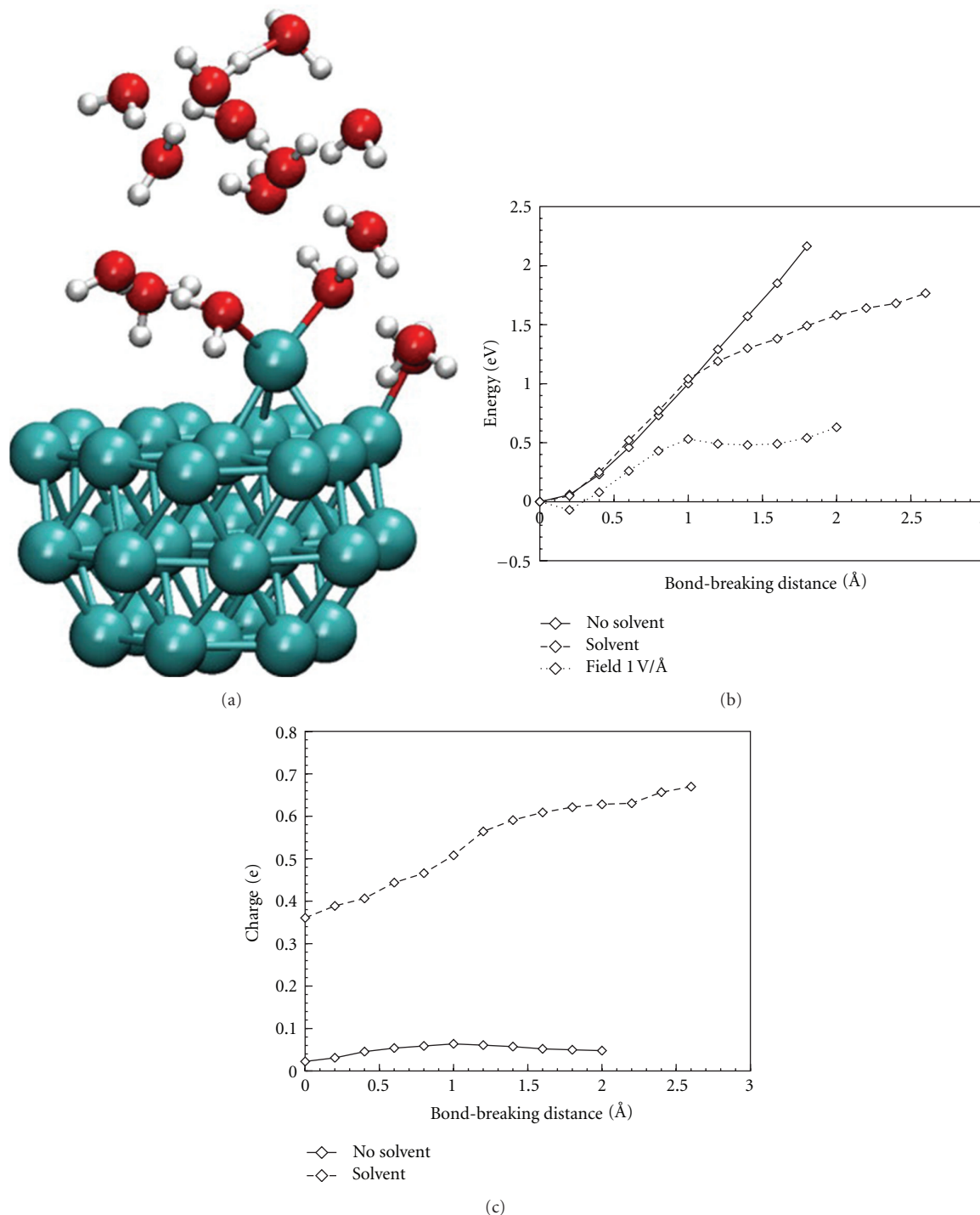


FIGURE 6: (a) Initial solvent-metal particle configuration, (b) electronic structure energies for dissolution/bond-breaking of a copper atom in proximity to a (111) copper surface, and (c) charges determined by the method of Bader for the copper adatom being “dragged” away from the (111) copper surface. Reproduced with permission from [111].

using our density functional theory slab calculations, is presented in Figure 7.

Figure 7 was calculated using a particular set of boundary conditions that apply to a saturated NH_4Cl solution, mimicking the case when a hygroscopic NH_4Cl salt film precipitates on the surface of a mild steel component.

Similarly to the case of water of transition metal surfaces, there is a range of H, OH, and O stabilities. Chloride in the solution phase, introduced by the equilibration of NH_4Cl salt film with condensed water, can also be adsorbed on to the surface between the electrochemical potentials of -450 and -420 mV SHE. In this window, which corresponds to

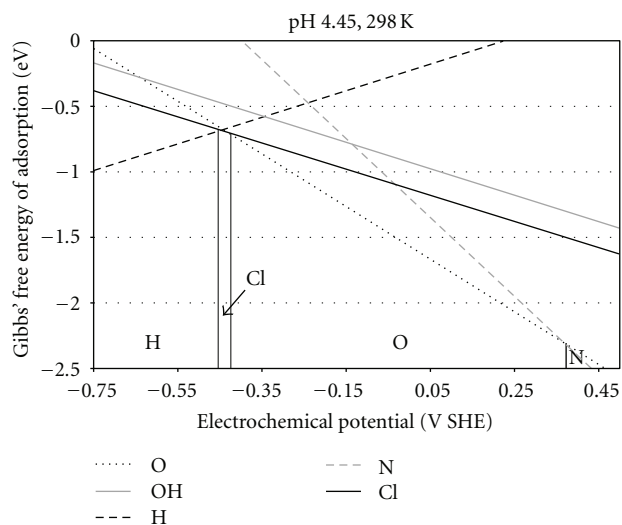


FIGURE 7: Free energy diagrams for surface coverage of the Fe(110) surface when exposed to a saturated NH_4Cl solution at pH 4.45 and 25°C (298 K). Reproduced with permission from [113].

the important prepassive state, chloride may be active in accelerating the corrosion of the mild steel [1]. Chloride may also inhibit passivation by displacing oxygen from the surface [116, 118]. The high concentrations of ammonia present also lead to the prediction of a nitrogenated surface beyond 370 mV SHE (although at this potential a bare iron surface is unlikely, unless cracking of the oxide film occurs, or the film is destabilized by some other chemical reaction). Similar diagrams can be constructed for other systems, in which the pH may be buffered to a more alkaline value or at different temperatures. The surface analysis generally supports the overall mechanisms proposed by Pletnev et al., Shimbarevich and Tseitlin, and Alvarez and Galvele [1, 116–118], although a more detailed model coupling surface thermodynamics, kinetics, and mass transport processes would be required to provide a more comprehensive understanding of the problem.

6. Perspectives

In this paper we have highlighted three specific cases where atomistic modeling has provided additional insight into the pathways via which important corrosion processes, including prepassivation and water chemistry, metal dissolution, and competitive adsorption, may occur. In particular, computational modeling of atomistic processes allows the scientist to directly assess the applicability of various corrosion mechanisms to a particular materials/environment combination and to characterize the nature of the interface at nanometer-subnanometer resolution.

At the same time, there is still some way to go for the computational science community to be able to represent the kinds of length and time scales associated with the

macro- and mesoscopic corrosion processes. Some of these challenges include:

- (1) capturing adequate dynamic time scales for the re-arrangement of solvent particles around atoms undergoing dissolution,
- (2) capturing not only details of the metal/environment interface but also the metal/oxide and oxide/environment interfaces,
- (3) Incorporating the very important effects of alloying components in both the metallic and oxide states in both solid solution and as particle inclusions,
- (4) Including the role of defect states, such as step edges, terraces, roughened surfaces, grain boundaries, and dislocations as potentially the most active sites at which corrosion events are going to occur.

The development of such advanced toolkits, using either state of the art potentials, such as the reactive force field [119], or multiscale modeling projects [28, 29, 37], is an active focus in our current portfolio of research projects.

That is not to say that the present toolkit does not allow the determination of meaningful insights into corrosion science. Using the kinds of density functional theory calculations, we have described above it is possible to do the following.

- (1) Predict thermodynamic and kinetic parameters for fundamental processes on metal and metal-oxide surfaces, such as water dissociation and adsorption of molecular and atomic species (such as NH_3 and Cl).
- (2) Understand the role local binding and morphology have on the thermodynamic cohesive energies of metal atoms exposed to the environment.
- (3) Explore dissolution trajectories and the influence of environmental species in raising or lowering the activation barriers to such processes. Consider, for example, the metal atom dissolution described in Section 3, but replacing a water molecule with a different ligand, such as chloride or nitrate, for example.
- (4) Adsorption and absorption of solution phase species, including hydrogen, for hydrogen embrittlement scenarios.
- (5) Computation of fundamental atomistic parameters for utilization in higher-level kinetic Monte Carlo simulations or phase field models.

The above five examples are just a subset of the kinds of simulations currently being performed for corrosion-related problems in the materials science literature. We anticipate many new applications developing that go beyond the specifications outlined here, as more groups adopt atomistic modeling within their research toolkit, and new algorithms and synergies with continuum or mesoscale techniques are developed.

A final point should be made regarding experimental validation. First-principles modeling techniques are subject

to variation depending upon the granularity and accuracy of the physics approximations used in their construction. For this reason, it is not uncommon to find variations, for example, in binding energies of molecules and materials calculated using different methods of 30–50 kJ/mol. Similarly, structural features, such as bond lengths and lattice parameters, can also be subject to variation depending upon the physics model selected. For these reasons, it is imperative that an equal, if not greater, effort continues to be applied in the characterization of interfacial phenomena using high-resolution, surface-specific probes (scanning tunneling microscopy and surface-enhanced Raman spectroscopy, e.g.). Improving resolution in both time and length scales is critical to provide the guidance needed for the improvement of the physics models that underlie the kinds of simulations described in this paper. As is the case in most research areas, advances in the understanding of corrosion processes can occur when a synergy is applied between the theoretical and experimental sciences.

Acknowledgments

The author is grateful for the illuminating and motivational discussions with Professor Robert Kelly (University of Virginia), Professor Matthew Neurock (University of Virginia), Professor Eliezer Gileadi (Tel-Aviv University), and Dr. Scott Lillard (Los Alamos National Laboratory). The author is also indebted to Michael Francis (U. Virginia, Los Alamos National Laboratory) for a careful reading of this paper. Los Alamos National Laboratory is operated by the Los Alamos National Security LLC for the National Nuclear Security Administration of the US Department of Energy under contract DE-AC52[28]-06NA2539.

References

- [1] M. A. Pletnev, S. G. Morozov, and V. P. Alekseev, "Peculiar effect of chloride ions on the anodic dissolution of iron in solutions of various acidity," *Protection of Metals*, vol. 36, no. 3, pp. 202–208, 2000.
- [2] P. Marcus, "Corrosion mechanics in theory and practice," in *Corrosion Technology*, P. A. Schweitzer, Ed., Marcel-Dekker, New York, NY, USA, 2nd edition, 2002.
- [3] J. O. M. Bockris, A. K. N. Reddy, and M. Gamboa-Aldeco, *Modern Electrochemistry. Vol. 2A*, Kluwer Academic; Plenum Publishers, New York, NY, USA, 2000.
- [4] C. D. Taylor, "Cohesive relations for surface atoms in the iron-technetium binary system," *Journal of Metallurgy*, vol. 2011, Article ID 954170, 8 pages, 2011.
- [5] J. Postlethwaite, S. Nešić, G. Adamopoulos, and D. J. Bergstrom, "Predictive models for erosion-corrosion under disturbed flow conditions," *Corrosion Science*, vol. 35, no. 1–4, pp. 627–633, 1993.
- [6] Y. Feng, K. S. Siow, W. K. Teo, K. L. Tan, and A. K. Hsieh, "Corrosion mechanisms and products of copper in aqueous solutions at various pH values," *Corrosion*, vol. 53, no. 5, pp. 389–398, 1997.
- [7] S. P. Trasatti and E. Sivieri, "Corrosion behaviour of titanium in non-aqueous solvents," *Materials Chemistry and Physics*, vol. 92, no. 2–3, pp. 475–479, 2005.
- [8] L. Stockert and H. Böhni, "Susceptibility to crevice corrosion and metastable pitting of stainless steels," *Materials Science Forum*, vol. 44–45, pp. 313–328, 1989.
- [9] T. R. Beck and S. G. Chan, "Experimental observations and analysis of hydrodynamic effects on growth of small pits," *Corrosion*, vol. 37, no. 11, pp. 665–671, 1981.
- [10] C. Y. Chao, L. F. Lin, and D. D. Macdonald, "A point defect model for anodic passive films: I. Film growth kinetics," *Journal of the Electrochemical Society*, vol. 128, no. 6, pp. 1187–1194, 1981.
- [11] L. F. Lin, C. Y. Chao, and D. D. Macdonald, "A point defect model for anodic passive films: II. Chemical breakdown and pit initiation," *Journal of the Electrochemical Society*, vol. 128, no. 6, pp. 1194–1198, 1981.
- [12] D. D. MacDonald, "The history of the point defect model for the passive state: a brief review of film growth aspects," *Electrochimica Acta*, vol. 56, no. 4, pp. 1761–1772, 2011.
- [13] V. A. Bogdanovskaya, M. R. Tarasevich, L. A. Reznikova, and L. N. Kuznetsova, "Composition, surface segregation, and electrochemical properties of binary PtM/C (M = Co, Ni, Cr) catalysts," *Russian Journal of Electrochemistry*, vol. 46, no. 9, pp. 1011–1020, 2010.
- [14] F. Friedersdorf and K. Sieradzki, "Film-induced brittle intergranular cracking of silver-gold alloys," *Corrosion (Houston)*, vol. 52, no. 5, pp. 331–336, 1996.
- [15] S. Jain, N. D. Budiansky, J. L. Hudson, and J. R. Scully, "Surface spreading of intergranular corrosion on stainless steels," *Corrosion Science*, vol. 52, no. 3, pp. 873–885, 2010.
- [16] E. M. Lehockey, A. M. Brennenstuhl, and I. Thompson, "On the relationship between grain boundary connectivity, coincident site lattice boundaries, and intergranular stress corrosion cracking," *Corrosion Science*, vol. 46, no. 10, pp. 2383–2404, 2004.
- [17] D. N. Wasnik, V. Kain, I. Samajdar, B. Verlinden, and P. K. De, "Controlling grain boundary energy to make austenitic stainless steels resistant to intergranular stress corrosion cracking," *Journal of Materials Engineering and Performance*, vol. 12, no. 4, pp. 402–407, 2003.
- [18] M. Baumgärtner and H. Kaesche, "Aluminum pitting in chloride solutions: morphology and pit growth kinetics," *Corrosion Science*, vol. 31, pp. 231–236, 1990.
- [19] R. Ambat, A. J. Davenport, G. M. Scamans, and A. Afseth, "Effect of iron-containing intermetallic particles on the corrosion behaviour of aluminium," *Corrosion Science*, vol. 48, no. 11, pp. 3455–3471, 2006.
- [20] F. Thébault, B. Vuillemin, R. Oltra, C. Allely, and K. Ogle, "Modeling bimetallic corrosion under thin electrolyte films," *Corrosion Science*, vol. 53, no. 1, pp. 201–207, 2011.
- [21] M. A. Arafin and J. A. Szpunar, "A novel microstructure-Grain boundary character based integrated modeling approach of intergranular stress corrosion crack propagation in polycrystalline materials," *Computational Materials Science*, vol. 47, no. 4, pp. 890–900, 2010.
- [22] V. Randle, "Grain boundary engineering: an overview after 25 years," *Materials Science and Technology*, vol. 26, no. 3, pp. 253–261, 2010.
- [23] E. A. West and G. S. Was, "IGSCC of grain boundary engineered 316L and 690 in supercritical water," *Journal of Nuclear Materials*, vol. 392, no. 2, pp. 264–271, 2009.
- [24] J. K. Nørskov, F. Abild-Pedersen, F. Studt, and T. Bligaard, "Density functional theory in surface chemistry and catalysis," *Proceedings of the National Academy of Sciences of the United States of America*, vol. 108, no. 3, pp. 937–943, 2011.

- [25] S. A. Wasileski, C. D. Taylor, and M. Neurock, "Modeling electrocatalytic reaction systems from first principles," in *Device and Materials Modeling in PEM Fuel Cells*, S. J. Paddison, Ed., Springer, Berlin, Germany, 2009.
- [26] R. A. van Santen and M. Neurock, *Molecular Heterogeneous Catalysis: A Conceptual and Computational Approach*, Wiley-VCH, Weinheim, Germany, 2006.
- [27] E. Gileadi, "Problems in interfacial electrochemistry that have been swept under the carpet," *Journal of Solid State Electrochemistry*, vol. 15, pp. 1359–1371, 2011.
- [28] T. J. Campbell, G. Aral, S. Ogata, R. K. Kalia, A. Nakano, and P. Vashishta, "Oxidation of aluminum nanoclusters," *Physical Review B*, vol. 71, no. 20, Article ID 205413, 14 pages, 2005.
- [29] S. Serebrinsky, E. A. Carter, and M. Ortiz, "A quantum-mechanically informed continuum model of hydrogen embrittlement," *Journal of the Mechanics and Physics of Solids*, vol. 52, no. 10, pp. 2403–2430, 2004.
- [30] C. Taylor, R. G. Kelly, and M. Neurock, "First-principles calculations of the electrochemical reactions of water at an immersed Ni (111) H₂O interface," *Journal of the Electrochemical Society*, vol. 153, no. 12, pp. E207–E214, 2006.
- [31] C. Taylor, R. G. Kelly, and M. Neurock, "Theoretical analysis of the nature of hydrogen at the electrochemical interface between water and a Ni(111) single-crystal electrode," *Journal of the Electrochemical Society*, vol. 154, no. 3, pp. F55–F64, 2007.
- [32] C. D. Taylor, R. G. Kelly, and M. Neurock, "First-principles prediction of equilibrium potentials for water activation by a series of metals," *Journal of the Electrochemical Society*, vol. 154, no. 12, pp. F217–F221, 2007.
- [33] G. Jomard, T. Petit, A. Pasturel, L. Magaud, G. Kresse, and J. Hafner, "First-principles calculations to describe zirconia pseudopolymorphs," *Physical Review B*, vol. 59, no. 6, pp. 4044–4052, 1999.
- [34] S. K. R. S. Sankaranarayanan and S. Ramanathan, "On the low-temperature oxidation and ultrathin oxide growth on zirconium in the presence of atomic oxygen: a modeling study," *Journal of Physical Chemistry C*, vol. 112, no. 46, pp. 17877–17882, 2008.
- [35] J. Greeley, "First-principles investigations of electrocatalysis and corrosion," in *Proceedings of the 214th ECS Meeting Proton Exchange Membrane Fuel Cells (PEMFC '08)*, vol. 16, pp. 209–213, Honolulu, Hawaii, USA, October 2008.
- [36] C. D. Taylor et al., "Calculation of surface properties of selected waste-form alloy systems," Report for DOE: Fundamental Waste Form Science, Los Alamos National Laboratory, Los Alamos, NM, USA, 2011.
- [37] R. Spatschek, E. Brener, and A. Karma, "Phase field modeling of crack propagation," *Philosophical Magazine*, vol. 91, no. 1, pp. 75–95, 2011.
- [38] R. M. Martin, *Electronic Structure: Basic Theory and Practical Methods*, Cambridge University Press, Cambridge, UK, 2004.
- [39] E. Kaxiras, *Atomic and Electronic Structure of Solids*, Cambridge University Press, Cambridge, UK, 2003.
- [40] I. N. Levine, *Quantum Chemistry*, Prentice Hall, Upper Saddle River, NJ, USA, 5th edition, 2000.
- [41] P. B. Balbuena, K. P. Johnston, and P. J. Rossky, "Molecular dynamics simulation of electrolyte solutions in ambient and supercritical water. 1. Ion solvation," *Journal of Physical Chemistry*, vol. 100, no. 7, pp. 2706–2715, 1996.
- [42] D. Domínguez-Ariza, C. Hartnig, C. Sousa, and F. Illas, "Combining molecular dynamics and ab initio quantum-chemistry to describe electron transfer reactions in electrochemical environments," *Journal of Chemical Physics*, vol. 121, no. 2, pp. 1066–1073, 2004.
- [43] P. F. Weck, E. Kim, F. Poineau, and K. R. Czerwinski, "Structural evolution and properties of subnanometer Tc_n (n = 2–15) clusters," *Physical Chemistry Chemical Physics*, vol. 11, no. 43, pp. 10003–10008, 2009.
- [44] A. B. Anderson and N. C. Debnath, "Mechanism of iron dissolution and passivation in an aqueous environment: active and transition ranges," *Journal of the American Chemical Society*, vol. 105, no. 1, pp. 18–22, 1983.
- [45] A. B. Anderson and N. K. Ray, "Structures and reactions of H₃O⁺, H₂O, and OH on an Fe electrode. Potential dependence," *Journal of Physical Chemistry*, vol. 86, no. 4, pp. 488–494, 1982.
- [46] E. E. Ebenso, T. Arslan, F. Kandemirli, N. Caner, and I. Love, "Quantum chemical studies of some rhodanine azo-sulpha drugs as corrosion inhibitors for mild steel in acidic medium," *International Journal of Quantum Chemistry*, vol. 110, no. 5, pp. 1003–1018, 2010.
- [47] E. E. Ebenso, T. Arslan, F. Kandemirli et al., "Theoretical studies of some sulphonamides as corrosion inhibitors for mild steel in acidic medium," *International Journal of Quantum Chemistry*, vol. 110, no. 14, pp. 2614–2636, 2010.
- [48] M. C. Payne, M. P. Teter, D. C. Allan, T. A. Arias, and J. D. Joannopoulos, "Iterative minimization techniques for ab initio total-energy calculations: molecular dynamics and conjugate gradients," *Reviews of Modern Physics*, vol. 64, no. 4, pp. 1045–1097, 1992.
- [49] I. Milas, B. Hinnemann, and E. A. Carter, "Diffusion of Al, O, Pt, Hf, and Y atoms on α -Al₂O₃(0001): implications for the role of alloying elements in thermal barrier coatings," *Journal of Materials Chemistry*, vol. 21, no. 5, pp. 1447–1456, 2011.
- [50] O. Runevall and N. Sandberg, "Self-diffusion in MgO—a density functional study," *Journal of Physics*, vol. 23, no. 34, pp. 345–402, 2011.
- [51] D. A. Andersson, B. P. Uberuaga, P. V. Nerikar et al., "U and Xe transport in UO_{2+x}: density functional theory calculations," *Journal of Chemical Physics*, vol. 84, no. 5, Article ID 054105, 12 pages, 2011.
- [52] C. D. Taylor, T. Lookman, and R. S. Lillard, "Ab initio calculations of the uranium-hydrogen system: thermodynamics, hydrogen saturation of α -U and phase-transformation to UH₃," *Acta Materialia*, vol. 58, no. 3, pp. 1045–1055, 2010.
- [53] G. Lu and E. Kaxiras, "Hydrogen embrittlement of aluminum: the crucial role of vacancies," *Physical Review Letters*, vol. 94, no. 15, Article ID 155501, 4 pages, 2005.
- [54] G. Lu, D. Orlikowski, I. Park, O. Politano, and E. Kaxiras, "Energetics of hydrogen impurities in aluminum and their effect on mechanical properties," *Physical Review B*, vol. 65, no. 6, Article ID 064102, pp. 641021–641028, 2002.
- [55] G. Lu, Q. Zhang, N. Kioussis, and E. Kaxiras, "Hydrogen-enhanced local plasticity in aluminum: an ab initio study," *Physical Review Letters*, vol. 87, no. 9, Article ID 095501, 4 pages, 2001.
- [56] J. Greeley and J. K. Nørskov, "Electrochemical dissolution of surface alloys in acids: thermodynamic trends from first-principles calculations," *Electrochimica Acta*, vol. 52, no. 19, pp. 5829–5836, 2007.
- [57] A. Bouzoubaa, D. Costa, B. Diawara, N. Audiffren, and P. Marcus, "Insight of DFT and atomistic thermodynamics on the adsorption and insertion of halides onto the hydroxylated NiO(111) surface," *Corrosion Science*, vol. 52, no. 8, pp. 2643–2652, 2010.

- [58] M. I. Baskes and R. A. Johnson, "Modified embedded atom potentials for HCP metals," *Modelling and Simulation in Materials Science and Engineering*, vol. 2, no. 1, article 011, pp. 147–163, 1994.
- [59] S. M. Foiles, M. I. Baskes, and M. S. Daw, "Embedded-atom-method functions for the fcc metals Cu, Ag, Au, Ni, Pd, Pt, and their alloys," *Physical Review B*, vol. 33, no. 12, pp. 7983–7991, 1986.
- [60] B. J. Lee and M. I. Baskes, "Second nearest-neighbor modified embedded-atom-method potential," *Physical Review B*, vol. 62, no. 13, pp. 8564–8567, 2000.
- [61] J. W. Halley, A. Mazzolo, Y. Zhou, and D. Price, "First-principles simulations of the electrode—electrolyte interface," *Journal of Electroanalytical Chemistry*, vol. 450, no. 2, pp. 273–280, 1998.
- [62] J. W. Halley, B. B. Smith, S. Walbran et al., "Theory and experiment on the cuprous-cupric electron transfer rate at a copper electrode," *Journal of Chemical Physics*, vol. 110, no. 13, pp. 6538–6552, 1999.
- [63] D. L. Price and J. W. Halley, "Molecular dynamics, density functional theory of the metal-electrolyte interface," *The Journal of Chemical Physics*, vol. 102, no. 16, pp. 6603–6612, 1995.
- [64] B. B. Smith and J. W. Halley, "Simulation study of the ferrous ferric electron transfer at a metal-aqueous electrolyte interface," *The Journal of Chemical Physics*, vol. 101, no. 12, pp. 10915–10924, 1994.
- [65] E. Spohr, "Computer simulation of the water/platinum interface. Dynamical results," *Chemical Physics*, vol. 141, no. 1, pp. 87–94, 1990.
- [66] E. Spohr, "Molecular dynamics simulations of water and ion dynamics in the electrochemical double layer," *Solid State Ionics*, vol. 150, no. 1-2, pp. 1–12, 2002.
- [67] E. Spohr, "Some recent trends in computer simulations of aqueous double layers," *Electrochimica Acta*, vol. 49, no. 1, pp. 23–27, 2003.
- [68] E. Spohr and K. Heinzinger, "Molecular dynamics simulation of a water/metal interface," *Chemical Physics Letters*, vol. 123, no. 3, pp. 218–221, 1986.
- [69] E. Spohr, G. Tóth, and K. Heinzinger, "Structure and dynamics of water and hydrated ions near platinum and mercury surfaces as studied by MD simulations," *Electrochimica Acta*, vol. 41, no. 14, pp. 2131–2144, 1996.
- [70] X. M. Bai, A. F. Voter, R. G. Hoagland, M. Nastasi, and B. P. Uberuaga, "Efficient annealing of radiation damage near grain boundaries via interstitial emission," *Science*, vol. 327, no. 5973, pp. 1631–1634, 2010.
- [71] T. P. Schulze, "Efficient kinetic Monte Carlo simulation," *Journal of Computational Physics*, vol. 227, no. 4, pp. 2455–2462, 2008.
- [72] A. F. Voter, "Introduction to the kinetic monte carlo method," in *Radiation Effects in Solids*, K. E. Sickafus and E. A. Kotomin, Eds., Springer, NATO Publishing Unit, Dordrecht, The Netherlands, 2005.
- [73] B. Temel, H. Meskine, K. Reuter, M. Scheffler, and H. Metiu, "Does phenomenological kinetics provide an adequate description of heterogeneous catalytic reactions?" *Journal of Chemical Physics*, vol. 126, no. 20, Article ID 204711, 2007.
- [74] B. Diawara, M. Legrand, J. J. Legendre, and P. Marcus, "Use of quantum chemistry results in 3D modeling of corrosion of iron-chromium alloys," *Journal of the Electrochemical Society*, vol. 151, no. 3, pp. B172–B178, 2004.
- [75] D. M. Artymowicz, J. Erlebacher, and R. C. Newman, "Relationship between the parting limit for de-alloying and a particular geometric high-density site percolation threshold," *Philosophical Magazine*, vol. 89, no. 21, pp. 1663–1693, 2009.
- [76] J. Erlebacher, "An atomistic description of dealloying porosity evolution, the critical potential, and rate-limiting behavior," *Journal of the Electrochemical Society*, vol. 151, no. 10, pp. C614–C626, 2004.
- [77] S. A. Policastro, J. C. Carnahan, G. Zangari et al., "Surface diffusion and dissolution kinetics in the electrolyte-metal interface," *Journal of the Electrochemical Society*, vol. 157, no. 10, pp. C328–C337, 2010.
- [78] W. M. Young and E. W. Elcock, "Monte Carlo studies of vacancy migration in binary ordered alloys: I," *Proceedings of the Physical Society*, vol. 89, no. 3, article 329, pp. 735–746, 1966.
- [79] R. S. Lillard, G. F. Wang, and M. I. Baskes, "The role of metallic bonding in the crystallographic pitting of magnesium," *Journal of the Electrochemical Society*, vol. 153, no. 9, pp. B358–B364, 2006.
- [80] C. D. Taylor and M. Neurock, "Theoretical insights into the structure and reactivity of the aqueous/metal interface," *Current Opinion in Solid State and Materials Science*, vol. 9, no. 1-2, pp. 49–65, 2005.
- [81] M. A. Henderson, "The interaction of water with solid surfaces: fundamental aspects revisited," *Surface Science Reports*, vol. 46, no. 1–8, pp. 1–308, 2002.
- [82] S. Izvekov, A. Mazzolo, K. VanOpdorp, and G. A. Voth, "Ab initio molecular dynamics simulation of the Cu(110)-water interface," *Journal of Chemical Physics*, vol. 114, no. 7, pp. 3248–3257, 2001.
- [83] M. F. Toney, J. N. Howard, J. Richer et al., "Voltage-dependent ordering of water molecules at an electrode-electrolyte interface," *Nature*, vol. 368, no. 6470, pp. 444–446, 1994.
- [84] A. Michaelides, A. Alavi, and D. A. King, "Insight into H₂O-ice adsorption and dissociation on metal surfaces from first-principles simulations," *Physical Review B*, vol. 69, no. 11, Article ID 113404, 4 pages, 2004.
- [85] A. Michaelides, V. A. Ranea, P. L. De Andres, and D. A. King, "General model for water monomer adsorption on close-packed transition and noble metal surfaces," *Physical Review Letters*, vol. 90, no. 21, Article ID 216102, 4 pages, 2003.
- [86] A. Michaelides, A. Alavi, and D. A. King, "Different surface chemistries of water on Ru{0001}: from monomer adsorption to partially dissociated bilayers," *Journal of the American Chemical Society*, vol. 125, no. 9, pp. 2746–2755, 2003.
- [87] S. M. Bruemmer and L. E. Thomas, "High-resolution analytical electron microscopy characterization of corrosion and cracking at buried interfaces," *Surface and Interface Analysis*, vol. 31, no. 7, pp. 571–581, 2001.
- [88] C. D. Taylor and M. Rossi, "A mechanistic approach to iodine induced stress corrosion cracking of zircaloy cladding: introductory assessment and preliminary results," Report prepared for the Consortium for the Advanced Simulation of LWRs—Materials Performance and Optimization (C.R. Stanek), Los Alamos National Laboratory, Los Alamos, NM, USA, 2011.
- [89] G. Kresse and J. Hafner, "Ab initio molecular dynamics for liquid metals," *Physical Review B*, vol. 47, no. 1, pp. 558–561, 1993.
- [90] G. Kresse and J. Hafner, "Ab initio molecular-dynamics simulation of the liquid-metalamorphous- semiconductor transition in germanium," *Physical Review B*, vol. 49, no. 20, pp. 14251–14269, 1994.

- [91] G. Kresse and J. Furthmüller, "Efficiency of ab-initio total energy calculations for metals and semiconductors using a plane-wave basis set," *Computational Materials Science*, vol. 6, no. 1, pp. 15–50, 1996.
- [92] G. Kresse and J. Furthmüller, "Efficient iterative schemes for ab initio total-energy calculations using a plane-wave basis set," *Physical Review B*, vol. 54, no. 16, pp. 11169–11186, 1996.
- [93] G. Kresse and D. Joubert, "From ultrasoft pseudopotentials to the projector augmented-wave method," *Physical Review B*, vol. 59, no. 3, pp. 1758–1775, 1999.
- [94] S. Walbran, A. Mazzolo, J. W. Halley, and D. L. Price, "Model for the electrostatic response of the copper-water interface," *Journal of Chemical Physics*, vol. 109, no. 18, pp. 8076–8080, 1998.
- [95] J. Weissenrieder, A. Mikkelsen, J. N. Andersen, P. J. Feibelman, and G. Held, "Experimental evidence for a partially dissociated water bilayer on Ru{0001}," *Physical Review Letters*, vol. 93, no. 19, pp. 1–196102, 2004.
- [96] C. D. Taylor, S. A. Wasileski, J. S. Filhol, and M. Neurock, "First principles reaction modeling of the electrochemical interface: consideration and calculation of a tunable surface potential from atomic and electronic structure," *Physical Review B*, vol. 73, Article ID 165402, 16 pages, 2006.
- [97] A. Seyeux, V. Maurice, L. H. Klein, and P. Marcus, "In situ scanning tunnelling microscopic study of the initial stages of growth and of the structure of the passive film on Ni(111) in 1 mM NaOH(aq)," *Journal of Solid State Electrochemistry*, vol. 9, no. 5, pp. 337–346, 2005.
- [98] C. D. Taylor, R. G. Kelly, and M. Neurock, "A first-principles analysis of the chemisorption of hydroxide on copper under electrochemical conditions: a probe of the electronic interactions that control chemisorption at the electrochemical interface," *Journal of Electroanalytical Chemistry*, vol. 607, no. 1–2, pp. 167–174, 2007.
- [99] C. D. Taylor, *First principles modeling of the structure and reactivity of water at the metal/water interface*, Dissertation, University of Virginia, Charlottesville, Va, USA, 2006.
- [100] G. Niaura, "Surface-enhanced Raman spectroscopic observation of two kinds of adsorbed OH⁻ ions at copper electrode," *Electrochimica Acta*, vol. 45, no. 21, pp. 3507–3519, 2000.
- [101] J. Rossmeisl, J. K. Nørskov, C. D. Taylor, M. J. Janik, and M. Neurock, "Calculated phase diagrams for the electrochemical oxidation and reduction of water over Pt(111)," *Journal of Physical Chemistry B*, vol. 110, no. 43, pp. 21833–21839, 2006.
- [102] E. Gileadi, "Can an electrode reaction occur without electron transfer across the metal/solution interface?" *Chemical Physics Letters*, vol. 393, no. 4–6, pp. 421–424, 2004.
- [103] E. Gileadi, "Charge and mass transfer across the metal/solution interface," *Israel Journal of Chemistry*, vol. 48, no. 3–4, pp. 121–131, 2008.
- [104] A. Michaelides, V. A. Ranea, P. L. De Andres, and D. A. King, "General model for water monomer adsorption on close-packed transition and noble metal surfaces," *Physical Review Letters*, vol. 90, no. 21, Article ID 216102, 4 pages, 2003.
- [105] C. D. Taylor, M. Neurock, and J. R. Scully, "First-principles investigation of the fundamental corrosion properties of a model Cu₃₈ nanoparticle and the (111), (113) surfaces," *Journal of the Electrochemical Society*, vol. 155, no. 8, pp. C407–C414, 2008.
- [106] R. S. Lillard, G. F. Wang, and M. I. Baskes, "The role of metallic bonding in the crystallographic pitting of magnesium," *Journal of the Electrochemical Society*, vol. 153, no. 9, pp. B358–B364, 2006.
- [107] W. Schmickler, K. Pötting, and M. Mariscal, "A new simulation model for electrochemical metal deposition," *Chemical Physics*, vol. 320, no. 2–3, pp. 149–154, 2006.
- [108] M. I. Baskes, S. G. Srinivasan, S. M. Valone, and R. G. Hoagland, "Multistate modified embedded atom method," *Physical Review B*, vol. 75, no. 9, Article ID 094113, 2007.
- [109] P. Biedermann, E. Torres, and A. Blumenau, "Oxygen reduction at thiol/Au(111) SAMs, atomistic modelling and experiment," in *Proceedings of the 212th Meeting of the Electrochemical Society on Modeling and Simulation of Dissolution and Corrosion Processes*, The Electrochemical Society, Washington, DC, USA, 2007.
- [110] S. M. Valone and S. R. Atlas, "Electron correlation, reference states and empirical potentials," *Philosophical Magazine*, vol. 86, no. 17–18, pp. 2683–2711, 2006.
- [111] C. D. Taylor, "The transition from metal-metal bonding to metal-solvent interactions during a dissolution event as assessed from electronic structure," *Chemical Physics Letters*, vol. 469, no. 1–3, pp. 99–103, 2009.
- [112] American Petroleum Institute, *Damage Mechanisms Affecting Fixed Equipment in the Refining Industry*, American Petroleum Institute, Washington, DC, USA, 2003.
- [113] C. D. Taylor, "Predictions of surface electrochemistry of saturated and alkaline NH₄Cl solutions interacting with Fe(110) from ab initio calculations," *Corrosion*. In press.
- [114] R. A. White, *Materials Selection for Petroleum Refineries and Gathering Facilities*, NACE International, Houston, Tex, USA, 1998.
- [115] O. Forsén, J. Aromaa, and M. Tavi, "Corrosion resistance of different materials in dilute ammonium chloride-bearing environments," *Corrosion Science*, vol. 35, no. 1–4, pp. 297–301, 1993.
- [116] V. A. Shimbarevich and K. L. Tseitlin, "Influence of ammonia concentration and temperature on corrosion of carbon steel in ammonium chloride solutions," *Protection of Metals*, vol. 15, no. 5, pp. 455–458, 1979.
- [117] V. A. Shimbarevich and K. L. Tseitlin, "Influence of ammonia on corrosion of stainless steels and titanium in ammonium chloride solutions at 200°C," *Protection of Metals*, vol. 17, no. 2, pp. 144–148, 1981.
- [118] M. G. Alvarez and J. R. Galvele, "The mechanism of pitting of high purity iron in NaCl solutions," *Corrosion Science*, vol. 24, no. 1, pp. 27–48, 1984.
- [119] A. C. T. Van Duin, S. Dasgupta, F. Lorant, and W. A. Goddard, "ReaxFF: a reactive force field for hydrocarbons," *Journal of Physical Chemistry A*, vol. 105, no. 41, pp. 9396–9409, 2001.

Research Article

Preliminary Study of Corrosion Status on Bronzes Excavated from Qin Dynasty Tombs at Xinfeng Town in China

Qian-li Fu,¹ Pu-jun Jin,² Xue Ling,³ Shang-xin Zhang,¹ Wei-gang Sun,⁴ and Yin Xia¹

¹ Emperor Qin's Terra-Cotta Warriors & Horses Museum, Lin Tong, Shaanxi Province, Xi'an 710600, China

² School of Materials Science and Engineering, Shaanxi Normal University, Chang An South Road 199#, Shaanxi Province, Xi'an 710062, China

³ School of Cultural Heritage, Northwest University, Tai Bai North Road 229#, Shaanxi Province, Xi'an 710069, China

⁴ Institute of Archaeology of Shaanxi, Yan Ta Region, Shaanxi Province, Xi'an 710043, China

Correspondence should be addressed to Pu-jun Jin, jinpj@snnu.edu.cn

Received 10 August 2011; Revised 22 January 2012; Accepted 24 January 2012

Academic Editor: Rokuro Nishimura

Copyright © 2012 Qian-li Fu et al. This is an open access article distributed under the Creative Commons Attribution License, which permits unrestricted use, distribution, and reproduction in any medium, provided the original work is properly cited.

From 2007 to 2008, many bronze wares of Qin Dynasty were excavated from tombs at Xinfeng town. Being an important finding, these bronze wares attracted people's attention, especially for their conservation. Therefore, the corrosive products were explored by using Scanning Electron Microscope with Energy Dispersive X-ray Detector (SEM/EDS), X-Ray diffraction (XRD), and Raman spectroscopy (RM), which provided much valuable information on the conservation of these bronze wares. According to tested results, the corrosive products of bronzes were found to be comprised of cuprite (Cu_2O), covellite (CuS), lead carbonate (PbCO_3), and malachite ($\text{CuCO}_3 \cdot \text{Cu}(\text{OH})_2$). Meantime, the multilayer corrosive structure was found in some samples due to the cracks in Cu_2O layer which had formed many microchannels to promote the material migration.

1. Introduction

From 2007 to 2008, about six hundred Qin Dynasty tombs were unearthed by archaeologists at Xinfeng town in Xi'an city, Shanxi province, China. It was reported as a significant archaeological excavation to dig out the largest number and scale of the Qin tombs in the central Shaanxi plain [1].

The site located south shore secondary tableland of Wei He River which was a domicile named as "Xiyi" where ceramics craftsman had once lived to build Qin Shi Huang Mausoleum [2].

A lot of bronzes were unearthed from these tombs, such as bronze ding tripod, bronze dou, bronze hu, and arrow, many of which were broken and in severe corrosion [2]. The bronzes are ternary alloy with the element of Cu, Sn, and Pb that would be in different corrosive situation after a long buried time [3]. In general, people had always research the corrosive mechanism of ancient bronze by analyzing on corrosive products or doing the simulated experiments [4, 5]. The analysis of corrosive products will supply important information to protect them and also provide important

reference to research their corrosive mechanism. This paper studied the corrosive products from the bronze fragments by Scanning electron microscope with energy dispersive X-ray detector (SEM/EDAX), X-Ray diffraction (XRD), and Raman spectroscopy (RM) and revealed the corrosive situation and mechanism on them.

2. Samples and Methods

2.1. Test Samples. In this paper, eight samples from different bronzes were studied, as shown in Table 1. All of them were collected from bronze fragile pieces, whose section was dealt with coarse grinding and polishing before the experiment.

2.2. Instrumentation. The cross-section morphologies were examined by a digital optical microscope (Keyence, VHX-600K, Japan), which has large depth of field and was equipped with a 3CCD camera about 54 million pixels. X-ray diffraction (XRD) was obtained in a Rigaku D/Max-3C X-ray diffractometer, equipped with a $\text{Cu K}\alpha$ radiation

TABLE 1: The record of test samples collected from bronze fragile piece at Xinfeng town.

Number	Tombs/Implements	Sample site	Time	Location
Sample 1	M274/bronze <i>hu</i>	Abdomen	Qin	Xinfeng town
Sample 2	M83/bronze <i>ding</i>	Bottom	Qin	Xinfeng town
Sample 3	M691/bronze <i>ding</i>	Bottom	Qin	Xinfeng town
Sample 4	M301/bronze <i>ding</i>	Bottom	Qin	Xinfeng town
Sample 5	M55/bronze <i>ding</i>	Bottom	Qin	Xinfeng town
Sample 6	M268/bronze <i>hu</i>	Abdomen	Qin	Xinfeng town
Sample 7	M04/bronze <i>hu</i>	Abdomen	Qin	Xinfeng town
Sample 8	M256/bronze <i>pen</i>	Edge	Qin	Xinfeng town

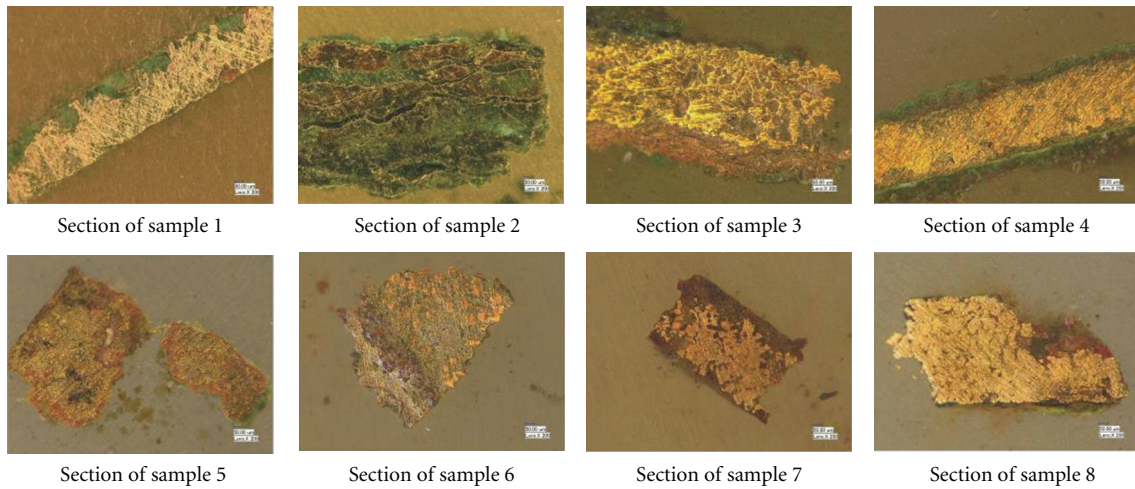


FIGURE 1: Section photomicrograph of bronze samples.

source ($\lambda = 0.154056 \text{ nm}$) in the 2θ range from 10° to 70° , tube voltage 40 KV, current 40 mA. A FEI-Quanta 200 environment scanning electron microscopy (SEM) equipped with an X-ray energy dispersive spectroscopy (EDS) was used to research samples, which were examined in the high-vacuum mode and low high-vacuum mode at an accelerating voltage about 20 kV. Roman spectra were attained by a microscopic confocal Raman Spectrometer (Renishaw in via Plus, England) employing a 514 nm laser beam excited by argon ion laser with information collection time about 10 s and accumulation time about 3~5 s.

3. Results

3.1. Optical Microscope Analysis. The cross section of samples indicated that these bronze fragile pieces were a serious corrosion, as shown in Figure 1. Many samples had similarly corrosive situation, such as sample 1, 3, 4, 5, 6, 7, and 8, which had outer green rust layer and inner red rust layer [6]. Specially, the section of sample 2 demonstrated a multilayer dust, which had the existence of alternate red and green corrosive product layer.

3.2. Backscattered Electron Phase and Component Analysis. After samples were inlaid into Acrylic resin, they were dealt with surface grinding and polishing. Then sample 1, 2, 3, and

6 were analyzed by SEM/EDS, whose electron images were attained by backscattered electron and elementary content were detected by X-ray energy dispersive spectroscopy (EDS), data as shown in Table 2.

There are four scanning area of sample 1, such as Area-1 to Area-4, as shown in Figure 2. The result indicates that Area-1 and Area-2 were outer layer of corrosion with complex component, especially with high content of C and O element, which revealed that the surface layer of sample had been corroded. Meantime, the backscattered electron images of Area-3 take on a white look which due to PbCO_3 according to the high content of some element as 20.53% C 12.4% O and 67.07% Pb. The analyzed Area-4 revealed that a significant amount of 83.63% Cu and 16.37% Sn, which should be remnant α -phase in bronze alloy.

For sample 2, four areas were analyzed about Area-5 to Area-8, as shown in Figure 2. The analyzed Area-5 is middle area of red corrosive product layer whose component is complex with 36.46% C, 43.55% O, 14.13% Cu, 5.29% Pb and 0.57% Si, which mean that the red corrosive product layer (Cu_2O) contains impurities. The complex composition of 27.48% C, 26.67% O, 3.74% Cu, and 42.11% Pb indicates that lead carbonate is main corrosive product in the other analyzed Area-6.

Five areas of sample 3 were analyzed, Area-7 is α -phase in bronze alloy with 86.61% Cu and 13.39% Sn; Area-8 is

TABLE 2: The content of composite element of samples (wt%).

Area	Element																
	C	O	Cu	Sn	Pb	Ca	Si	Al	S	As	K	Fe	Mg	Ni	Cl	Na	P
Area-1	18	52.79	26.08		2.67	0.46											
Area-2	19.17	31.19	18.46	22.35	7.15		1.25	0.42									
Area-3	20.53	12.4			67.07												
Area-4			83.63	16.37													
Area-5	36.46	43.55	14.13		5.29		0.57										
Area-6	27.48	26.67	3.74		42.11												
Area-7			86.61	13.39													
Area-8	8.69	5.86	54.28	31.17													
Area-9		20.07	79.93														
Area-10	16.61	6.08	57.82						19.5								
Area-11	11.34	22.08	27.26	16.55	16.66					2.42					3.69		
Area-12	26.07	4.77	69.16														
Area-13	15.82	45.55			2.04		21.79	7.94			5.89						0.97
Area-14	23.24	34.74	5.99		24.49	1.47	4.43	2.11				1.57	0.63	1.34			

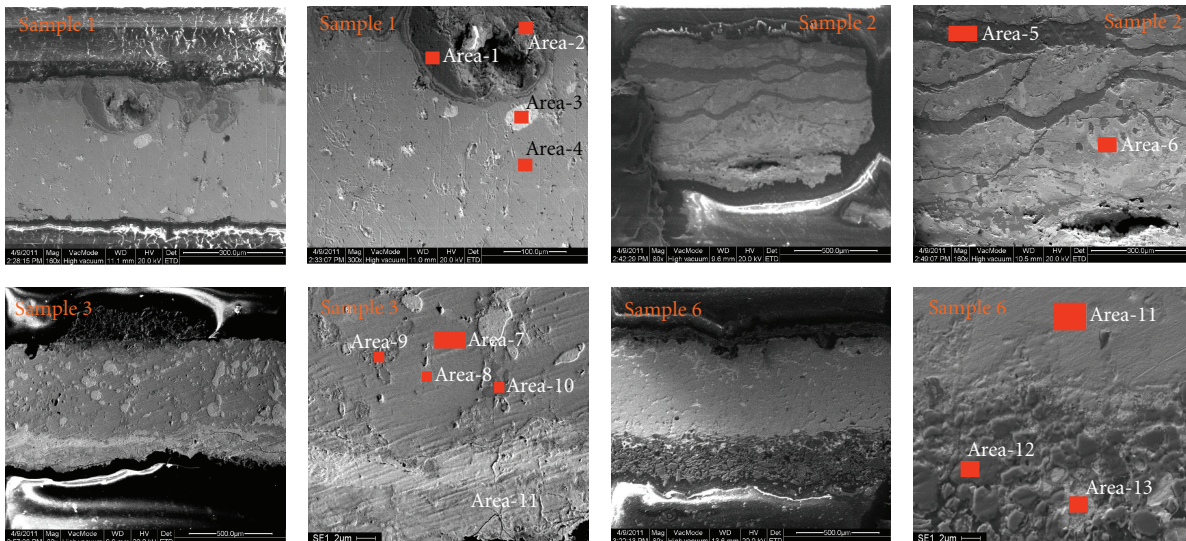


FIGURE 2: SEM photograph of sample cross section and drawing of site of energy spectrum analysis area.

the remnant α - δ -phase with 8.69% C, 5.86% O, 54.28% Cu, and 31.17% Sn; Area-9 is dull color area where is composed of 20.07% O and 79.93% Cu, which suggest the existence of copper oxide [7]; Area-10 is dark area with 19.5% S in which there are some copper sulfide; Area-11 shows white with complex composition and 16.66% Pb.

Sample 6 was analyzed in three areas from Area-12 to Area-14, as seen in Figure 2. In the Area-14, the high content of 24.49% Pb element was detected by EDS which is more than that in Area-13. In fact, Area-13 has complex component of 15.82% C, 45.55% O, 2.04% Pb, 21.79% Si, 7.94% Al, 5.89% K, and 0.97% Na which means this area is soil. On the other hand, Pb element wasn't found in the analyzed Area-12. It could draw a conclusion that element Pb has the trend of migration from the bronze alloy to the circumambient soil.

3.3. *Secondary Electron Image of Sample 2.* The secondary electron image of sample 2 showed obviously multilayer structure about corrosive layer, as seen in Figure 3. The zonal cuprite could be seen in the SEM image in which many cracks also were observed clearly.

3.4. *Analysis of XRD.* The XRD pattern of sample (Figure 4) showed that the peaks at 29.6°, 36.5°, 42.4°, and 61.5° can be indexed to Cu_2O (JCPDS Card No. 77-0199). Other diffraction peaks at 23.4°, 25.5°, 29.7°, 34.5°, 36.7°, 43.3°, and 49.7° can be indexed to PbCO_3 (JCPDS Card No. 03-0358).

3.5. *Raman Spectrum.* Different color corrosive product of cross section of sample 2 and sample 6 was analyzed by Micro-Raman spectroscopy. Figures 5(a) and 6(a) show

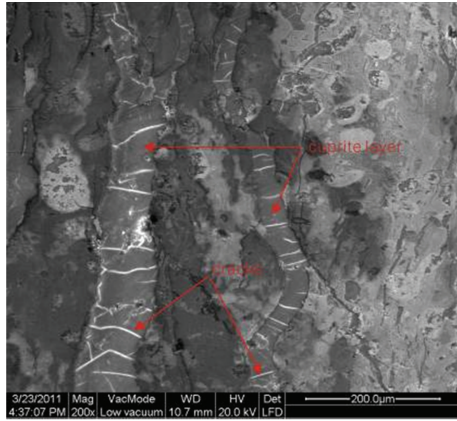


FIGURE 3: Morphology photograph of cross section of sample no. 2.

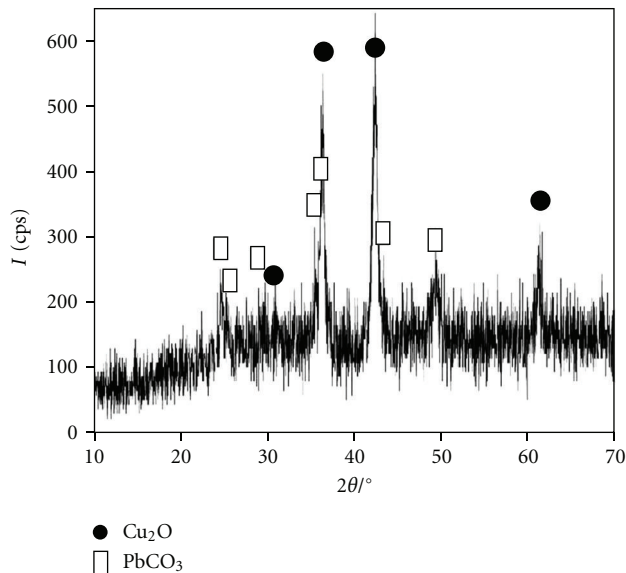
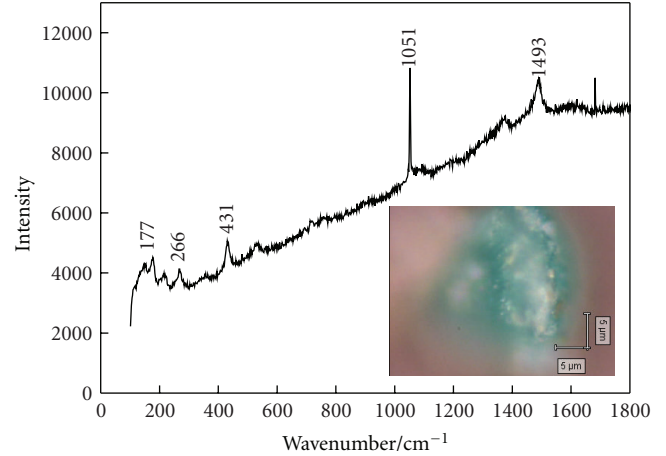


FIGURE 4: X-ray diffraction pattern of sample 1.

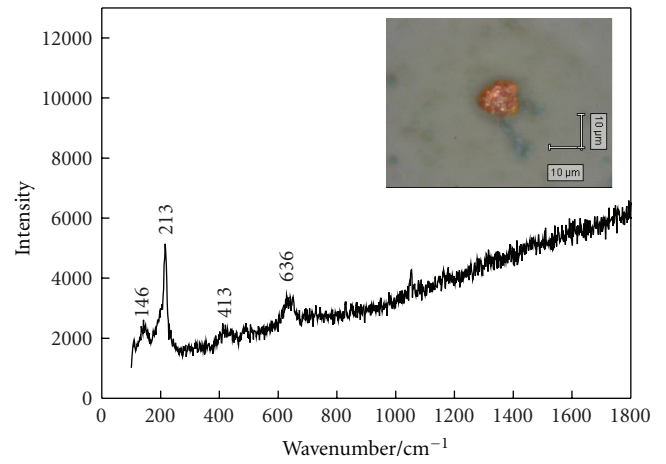
Raman pattern of patina from two samples which displayed vibration peaks at 1493 cm^{-1} (vs), 1051 cm^{-1} (vs), 431 cm^{-1} (vs), 266 cm^{-1} (m), and 177 cm^{-1} (s) due to malachite ($\text{CuCO}_3 \cdot \text{Cu}(\text{OH})_2$) [8]. The red corrosive product demonstrates Raman vibration peaks at 636 cm^{-1} (s), 413 cm^{-1} (m), 213 cm^{-1} (vs), and 146 cm^{-1} (m) corresponding to cuprous oxide (Cu_2O) [9], as shown in Figures 5(b) and 6(b). Figure 5(c) shows Raman pattern of blue corrosive product from sample 2 with a vibration peak at 472 cm^{-1} (vs) due to copper sulphide (CuS) [10, 11].

4. Discussion

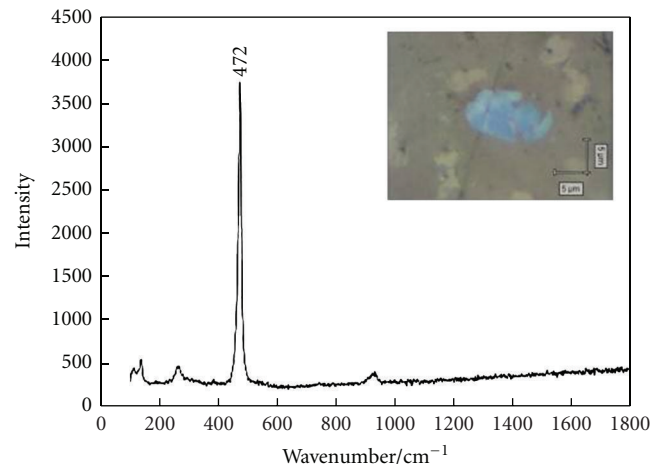
The analytical result of XRD indicates that two kinds of corrosive products existed in most collected test samples, which are Cu_2O and PbCO_3 . Actually, the signal of patina was not detected by XRD, which was confirmed by Raman spectroscopy as malachite ($\text{CuCO}_3 \cdot \text{Cu}(\text{OH})_2$).



(a)



(b)



(c)

FIGURE 5: Raman spectrum of corrosion of sample 2: (a) green particle; (b) red particle; (c) blue particle.

Cuprite (Cu_2O) is one kind of common corrosive products of bronze wares that underground burial environment [12, 13] that would form a tough red layer on the surface of

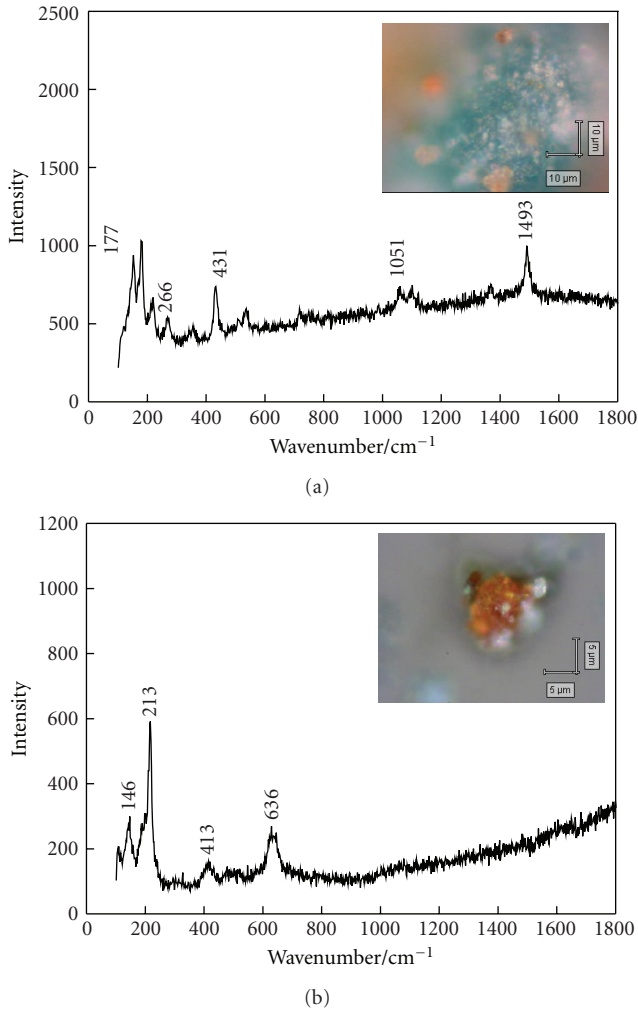


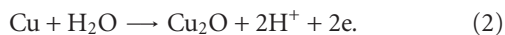
FIGURE 6: Raman spectrum of corrosion of sample 6: (a) green particle; (b) red particle.

bronze wares, which is regarded to delay corrosion of bronze alloy by keeping the harmful ion out [6, 14] and primary electrochemical reaction as follow.

Negative pole:



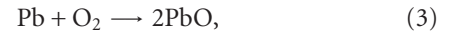
Positive pole:



Actually, transverse cracks observed in Cu_2O layer of cross section of sample 2 formed a free migrating pathway between the bronze alloy and the burial circumstance. The cracks in Cu_2O layer are likely to be a lot to produce along with the gradual corrosion of bronzes, its mechanism required further study.

Lead carbonate (PbCO_3) was confirmed by XRD that was a common lead corrosive phase in bronze wares [15].

Generally, the reaction of Pb to PbCO_3 will occur in burial environment as follow [16]:



By the result of SEM image and chemical element distribution, the sample 6 showed the migration out of Pb element from bronze alloy.

5. Conclusion

Photograph of cross section and component element data indicates that bronze substrate has been corroded severely, which must be consolidated before its restoration. The SEM image revealed transverse cracks in Cu_2O layer in sample 2 which had provided the pathway for element diffusion between the bronze alloy and the burial circumstance.

Acknowledgments

This work has been partially supported by the Sci. & Tech. Key Projects of Shaanxi Province of China under Grant no. 2009k01-43, by the Fundamental Research Funds for the Central Universities, by social science Fund of Shaanxi Normal University no. 09SYB05, by Scientific Research Project from Education Department of Shaanxi Provincial Government (2010JZ31), and by Cultural Relics Research Project of Chinese State Administration of Cultural Heritage (20090106).

References

- [1] S. Wei-gang, "Xi, Li Yi and Li mountain park—concurrently discuss function of Li Yi of emperor Qin Shihuang mausoleum," *Archaeology and Cultural Relics*, no. 4, pp. 67–71, 2009.
- [2] S. Wei-gang, *Study on Qin tombs unearthed from Xin feng*, M.S. thesis, Northwest University, 2009.
- [3] R. F. Tylecote, "The effect of soil conditions on the long-term corrosion of buried tin-bronzes and copper," *Journal of Archaeological Science*, vol. 6, no. 4, pp. 345–368, 1979.
- [4] L. Yu, Y. Si-xun, and Z. Xiao-mei, "Study on bronze corrosion from Jin State tombs of Zhou dynasty, Tian ma-Qu village," *Sciences of Conservation and Archeology*, vol. 2, pp. 9–18, 2000.
- [5] L. Yan-ping, C. Xiao-lin, C. Yu-bin, and W. Zhi-qiang, "Bronze sample corrosion experiment in soil in archaeological site," *Archaeology and Cultural Relics*, no. 6, pp. 95–98, 2006.
- [6] J. Pu-Jun, Q. Ying, H. Ya-Li, H. Si-Ping, and H. Wen-Hu, "Analysis of bronze corrosion product from No.1,2 tombs of Jiu lian dun tombs," *Jian Han Archaeology*, no. 1, pp. 112–119, 2009.
- [7] P. Valério Pedro, R. J. C. Silva, A. M. Monge Soares et al., "Technological continuity in early iron age bronze metallurgy at the South-Western Iberian Peninsula—a sight from Castro dos Ratinhos," *Journal of Archaeological Science*, vol. 37, no. 8, pp. 1811–1819, 2010.
- [8] L. I. McCann, K. Trentelman, T. Possley, and B. Golding, "Corrosion of ancient Chinese bronze money trees studied by

- Raman microscopy,” *Journal of Raman Spectroscopy*, vol. 30, no. 2, pp. 121–132, 1999.
- [9] M. C. Bernard and S. Joiret, “Understanding corrosion of ancient metals for the conservation of cultural heritage,” *Electrochimica Acta*, vol. 54, no. 22, pp. 5199–5205, 2009.
- [10] S. Xu, Q. Wang, J. H. Cheng, Q. H. Meng, and Y. Jiao, “Preparation and characteristics of porous CuS microspheres consisted of polycrystalline nanoslices,” *Powder Technology*, vol. 199, no. 2, pp. 139–143, 2010.
- [11] P. J. Jin, Z. Q. Yao, M. L. Zhang, Y. H. Li, and H. P. Xing, “A pigment (CuS) identified by micro-raman spectroscopy on a chinese funerary lacquer ware of West Han Dynasty,” *Journal of Raman Spectroscopy*, vol. 41, no. 2, pp. 222–225, 2010.
- [12] F. J. R. de Oliveira, D. C. B. Lago, L. F. Senna, L. R. M. de Miranda, and E. D’Elia, “Study of patina formation on bronze specimens,” *Materials Chemistry and Physics*, vol. 115, no. 2-3, pp. 761–770, 2009.
- [13] W. Hui-Zhen, W. Guo-Feng, Z. Hong, and J. Pu-Jun, “Corrosion mechanism and conservation study of bronze ge of Shang dynasty,” *Archaeology and Cultural Relics*, no. 3, pp. 93–96, 2001.
- [14] J. J. Shim and J. G. Kim, “Copper corrosion in potable water distribution systems: influence of copper products on the corrosion behavior,” *Materials Letters*, vol. 58, no. 14, pp. 2002–2006, 2004.
- [15] J. La-jiang, “Science and technology archaeology study of bronze of early Qin dynasty,” Northwest University, 2010.
- [16] E. Rocca, C. Rapin, and F. Mirambet, “Inhibition treatment of the corrosion of lead artefacts in atmospheric conditions and by acetic acid vapour: use of sodium decanoate,” *Corrosion Science*, vol. 46, no. 3, pp. 653–665, 2004.

Research Article

Stress-Corrosion Cracking Property of Aluminum-Magnesium Alloy Processed by Equal-Channel Angular Pressing

Hiroaki Nakano,¹ Satoshi Oue,¹ Seiji Taguchi,^{2,3} Shigeo Kobayashi,⁴ and Zenji Horita¹

¹Department of Materials Science & Engineering, Kyushu University, 744 Motoooka, Nishi-ku, Fukuoka 819-0395, Japan

²Department of Materials Process Engineering, Kyushu University, 744 Motoooka, Nishi-ku, Fukuoka 819-0395, Japan

³JFE Steel Corporation, Japan

⁴Department of Applied Chemistry and Biochemistry, Kyushu Sangyo University, 2-3-1 Matsukadai, Higashi-ku, Fukuoka 813-8503, Japan

Correspondence should be addressed to Hiroaki Nakano, nakano@zaiko.kyushu-u.ac.jp

Received 26 December 2011; Revised 19 January 2012; Accepted 19 January 2012

Academic Editor: Rokuro Nishimura

Copyright © 2012 Hiroaki Nakano et al. This is an open access article distributed under the Creative Commons Attribution License, which permits unrestricted use, distribution, and reproduction in any medium, provided the original work is properly cited.

Stress-corrosion cracking property of an aluminum-magnesium alloy processed by equal-channel angular pressing (ECAP) was investigated by a slow strain-rate tensile technique in a 3% NaCl solution of pH 4.2 at 303 K. The maximum stress and elongation of the Al-Mg alloy were lower in the NaCl solution than in air. The stress-corrosion cracking property was evaluated by the decrease ratio of maximum stress and elongation of the Al-Mg alloy with NaCl solution, $I(\delta_{\max})$ and $I(\delta)$, respectively. $I(\delta_{\max})$ and $I(\delta)$ were lower with ECAP than without it, showing that the susceptibility of stress-corrosion cracking decreased with ECAP. The polarization curve and time dependence of the anodic current density at constant potential of the Al-Mg alloy in the NaCl solution revealed that the anodic current density was lower with ECAP than without it, or the corrosion resistance of the Al-Mg alloy was improved by ECAP. The decrease in stress-corrosion crack susceptibility of the Al-Mg alloy with ECAP is attributed to an improvement in corrosion resistance afforded by ECAP.

1. Introduction

Although aluminum is an inherently active metal, it shows excellent corrosion resistance over a neutral range of pH 4–8 owing to its superficial oxide film. However, in solutions containing Cl^- , pitting corrosion occurs locally where the oxide film is attacked by Cl^- [1, 2]. When additional stress is applied, stress-corrosion cracking also occurs along the crystal grain boundary, resulting in serious damage [3–5]. On the other hand, reducing the grain size of metallic materials to the submicrometer or even the nanometer range by equal-channel angular pressing (ECAP), high-pressure torsion (HPT), or a severe torsion-straining process (STSP) is being studied increasingly with the aim of improving mechanical properties such as strength and ductility [6–11]. The effect of severe plastic deformation on the pitting corrosion resistance of Al alloys has been reported [12–15]; however, reports on the effect of stress-corrosion cracking are rare.

In this study, the stress-corrosion cracking property of an alloy of Al-3%Mg (by mass) processed by ECAP was investigated. Stress-corrosion cracking property was evaluated by a slow strain-rate tensile technique in a 3% NaCl solution. Since the stress-corrosion cracking property of the Al-Mg alloy was expected to depend on corrosion resistance, the effect of ECAP on the corrosion resistance of the Al-Mg alloy was investigated by polarization curves and the anodic current density at constant potential in the NaCl solution. The fracture area after the slow strain-rate tensile test was analyzed by scanning electron microscopy (SEM) at ultralow accelerating voltage and electron backscatter diffraction (EBSD).

2. Experimental

An Al-Mg alloy (mass %, <0.001% Cu, 0.004% Si, 0.001% Fe, <0.001% Mn, 3.0% Mg, <0.001% Zn, <0.001% Cr, and remainder Al) was used as the specimen. ECAP was

performed after annealing at 773 K for 1 h followed by air cooling. Figure 1 shows a schematic diagram of the ECAP process. ECAP was conducted for eight passes at room temperature using a die with a channel angle of 90° , which creates an equivalent strain of ~ 1 during one passage through the die. The sample was rotated 90° about the longitudinal axis in the same manner between consecutive passes, the generally designated processing route Bc [9]. In route Bc, ECAP changes the strain path by rotating the work piece 90° clockwise between two adjacent passes. The pressings were performed at a rate of $\sim 19 \text{ mm s}^{-1}$ using MoS_2 as a lubricant. The initial grain size of the Al-Mg alloy prior to ECAP was $800 \mu\text{m}$. The average grain size after the ECAP process was confirmed to be $0.5 \mu\text{m}$ by SEM observation.

Figure 2 is a schematic diagram of a specimen prepared for the slow strain-rate tensile test. The specimens were cut from a columnar ingot by electrical discharge machining. The tensile test area was 5 mm long, 4 mm wide, and 2 mm thick. The notch was $500 \mu\text{m}$ deep with a 0.3 mm radius of curvature, and a 60° angle was introduced into two spots of the tensile test area, as shown in Figure 2(b). The strain rate for the slow strain-rate tensile technique was $6.67 \times 10^{-5}/\text{s}$ and $1.67 \times 10^{-6}/\text{s}$ in air and the corrosive solution, respectively. The entire area outside the area of the tensile test was sealed by painting to prevent the specimen from contacting the NaCl solution. Alkaline cleaning in 10% NaOH solution, neutralization in 10% HNO_3 , each for 30 sec, rinsing in pure water, and drying were performed in that order. The corrosive solution was composed of a 3% NaCl solution at 303 K. The pH was adjusted to 4.2 with HCl solution.

Specimens 1.0 cm in diameter were prepared for corrosion testing as described below. Their corrosion resistance was investigated over an area 6 mm in diameter, and the remaining area was sealed with waterproof tape to prevent any corrosion from the edge. After the Al-Mg alloy was carefully polished with no. 1500 emery paper and immersed in a solution containing 0.1 mol/L of Na_2SO_4 and 8.46 mmol/L of NaCl (300 ppm Cl^-) at 303 K for 30 min in an air atmosphere, the polarization curves were measured by polarizing from -0.7 V versus NHE in the anodic potential direction by the potential sweep method at 0.5 mV s^{-1} . The time dependence of anodic current density was measured at a constant potential of -0.2 V after immersion for 30 min in the previous solution. The electrode potentials were measured during potential sweep using a saturated Ag/AgCl reference electrode (0.199 V versus NHE, 298 K). In the presentation of polarization curves, the potentials were plotted with reference to NHE.

The fracture surface after the slow strain-rate tensile test was observed by SEM and confocal laser scanning microscopy. The specimen was cut perpendicularly to a fracture surface and embedded in a conductive resin to investigate the internal texture after the tensile test. The specimen was analyzed by an ultralow accelerating voltage SEM (Carl Zeiss Ultra 55) and EBSD to generate electron backscatter patterns (EBSPs) after mirror polishing and Ar sputtering.

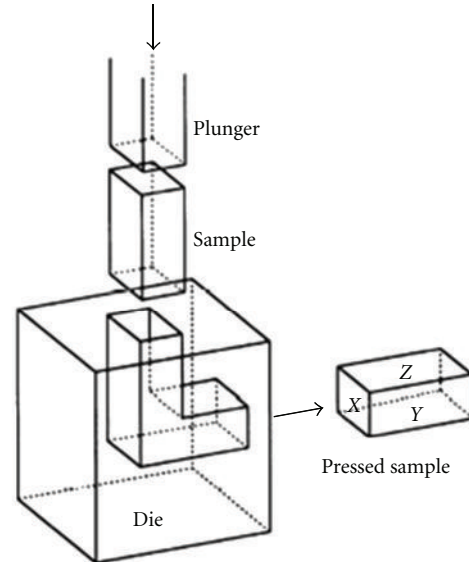


FIGURE 1: Schematic diagram of ECAP.

3. Results and Discussion

3.1. Effect of ECAP on Stress-Corrosion Cracking of Al-Mg Alloy. Figure 3 shows confocal laser scanning microscope images of the fracture surface of Al-Mg alloy after a slow strain-rate tensile test in air and NaCl solution. The Al-Mg alloy without ECAP shows evident necking (Figures 3(a) and 3(b)), while with ECAP hardly any necking is visible (Figures 3(c), 3(d)). In the Al-Mg alloy without ECAP, the cracks were observed to advance from the notch to the center in NaCl solution (Figure 3(b)).

Figure 4 shows SEM images of the fracture surface of the Al-Mg alloy after a slow strain-rate tensile test in air and NaCl solution. Pitting corrosion was observed tensioned in NaCl solution (Figure 4(b)). This pitting corrosion seems to promote the cracking. Dimples were observed with ECAP tensioned in air and NaCl solution (Figures 4(c) and 4(d)), showing ductile fracture. Even in the NaCl solution, clear pitting corrosion was barely visible in the Al-Mg alloy with ECAP (Figure 4(c)). As mentioned above, the fracture surface of the Al-Mg alloys with and without ECAP showed the ductile one even in NaCl solution, not clear the stress-corrosion cracking. However, since the pitting corrosion was observed and seems to promote the cracking after a slow strain-rate tensile test in NaCl solution, the cracking was assumed to be caused by both the stress and corrosion. Therefore, the cracking after a slow strain-rate tensile test in NaCl solution was expressed by the stress-corrosion cracking in this study.

Figure 5 shows the stress-strain diagram of the Al-Mg alloy obtained by a slow strain-rate tensile test in air and a 3% NaCl solution. As seen from the stress-strain diagram in air (grey and blue), the maximum stress increased from approximately 150 to 370 MPa by ECAP, while the total elongation decreased from approximately 0.6 to 0.15. This trend agrees with the properties of ultrafine-grained Al alloy

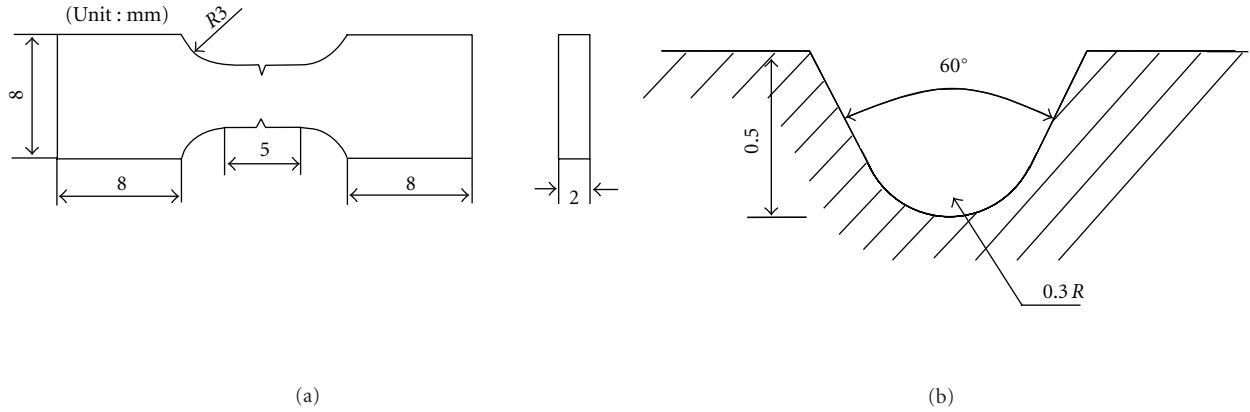


FIGURE 2: Tensile specimen (a) and magnification of notch (b) for slow strain-rate tensile test.

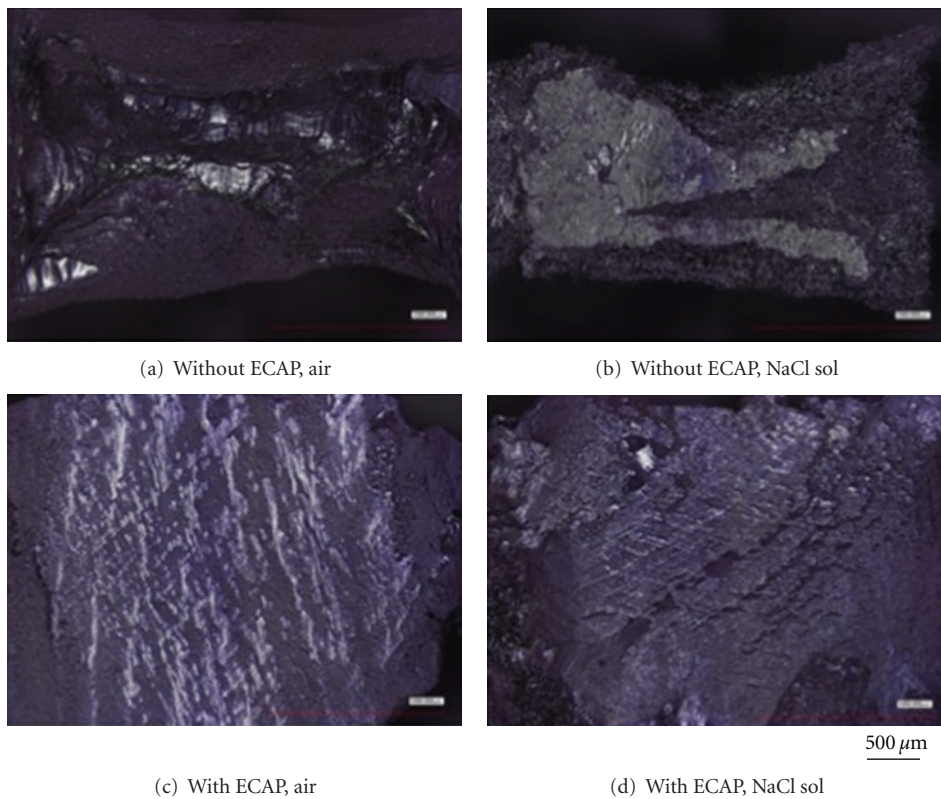


FIGURE 3: Confocal laser scanning microscope images of fracture surface of Al-Mg alloy with and without ECAP after slow strain-rate tensile test.

processed by ECAP [9–11]. The strength and elongation of the Al-Mg alloy without ECAP were significantly lower in the NaCl solution than in air (blue and red). The reason that specimens without the ECAP process showed different tensile stress and fracture strain on depending on the tensile circumstance seems to be due to stress-corrosion cracking. In both air and NaCl solution, the strength of the Al-Mg alloy was higher with ECAP (grey and pink) than without it (blue and red), while the elongation was lower with ECAP than without it. In the Al-Mg alloy with ECAP, as seen from the comparison of stress-strain curves in air (grey) and the NaCl

solution (pink), the strength was lower in the NaCl solution than in air, while the elongation in the NaCl solution was almost identical to that in air

$$I(\sigma_{\max}) = \frac{\sigma_{\text{air}} - \sigma_{\text{sol}}}{\sigma_{\text{air}}}, \quad (1)$$

$$I(\delta) = \frac{\delta_{\text{air}} - \delta_{\text{sol}}}{\delta_{\text{air}}}.$$

Stress-corrosion crack susceptibility was evaluated by $I(\sigma_{\max})$ and $I(\delta)$, which express the decrease ratio of maximum

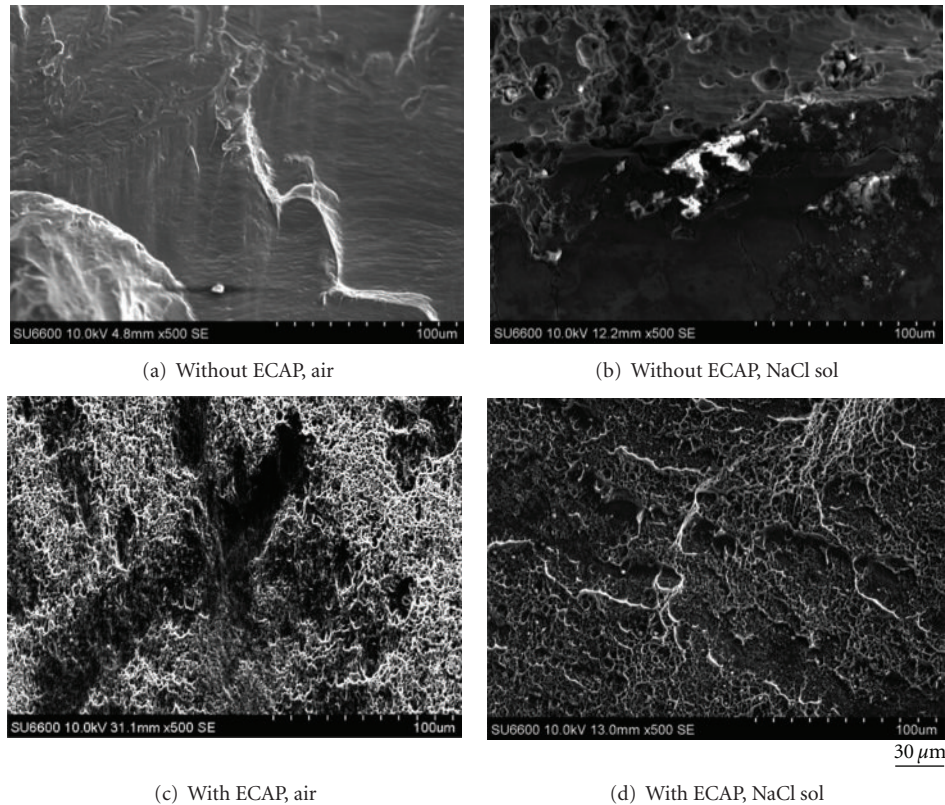


FIGURE 4: SEM images of fracture surface of Al-Mg alloy with and without ECAP after slow strain-rate tensile test.

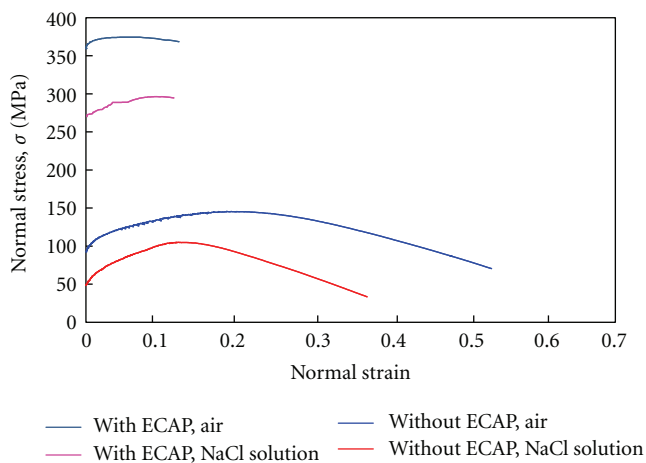


FIGURE 5: Stress-strain curves of Al-Mg alloy obtained by slow strain-rate tensile test.

stress and total elongation in the NaCl solution to those in air (1), where σ_{air} and σ_{sol} are the maximum stress in air and NaCl solution, respectively, and δ_{air} and δ_{sol} are the total elongation in air and NaCl solution, respectively [3, 4]. $I(\delta)$ seems to be more suitable for stress-corrosion crack susceptibility than $I(\sigma_{\text{max}})$ [4]. Table 1 shows the $I(\sigma_{\text{max}})$ and $I(\delta)$ calculated by the maximum stress and total elongation obtained from the stress-strain curves in Figure 5. $I(\sigma_{\text{max}})$

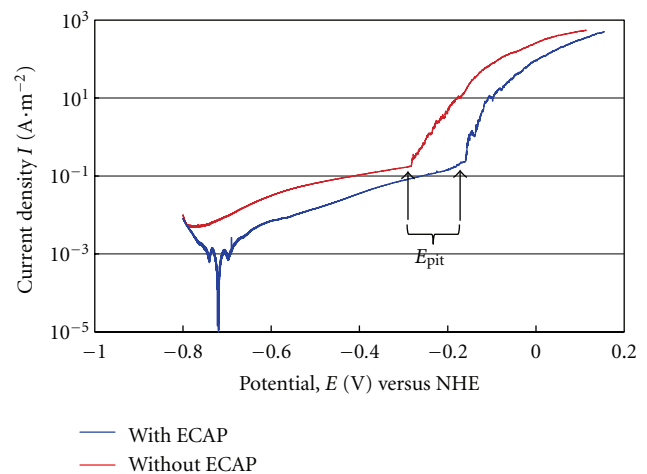


FIGURE 6: Polarization curves of Al-Mg alloy with and without ECAP in a solution containing $0.1 \text{ mol} \cdot \text{L}^{-1}$ of Na_2SO_4 and 300 ppm Cl^- .

and $I(\delta)$ were decreased by ECAP. $I(\delta)$ was significantly lower with ECAP than without it. $I(\sigma_{\text{max}})$ and $I(\delta)$ show that the stress-corrosion crack susceptibility of the Al-Mg alloy is smaller with ECAP than without it.

The corrosion resistance of the Al-Mg alloy was investigated to elucidate why $I(\sigma_{\text{max}})$ and $I(\delta)$ were decreased by ECAP. Figure 6 shows the effect of ECAP on the polarization

TABLE 1: Susceptibility of stress-corrosion cracking of Al-Mg alloy with and without ECAP.

Alloy	Environment	σ_{\max} (Mpa)	δ	$I(\sigma_{\max})$	$I(\delta)$
Without ECAP	Air	145	0.613	0.28	0.31
	NaCl solution	105	0.425		
With ECAP	Air	374	0.141	0.21	0.06
	NaCl solution	296	0.133		

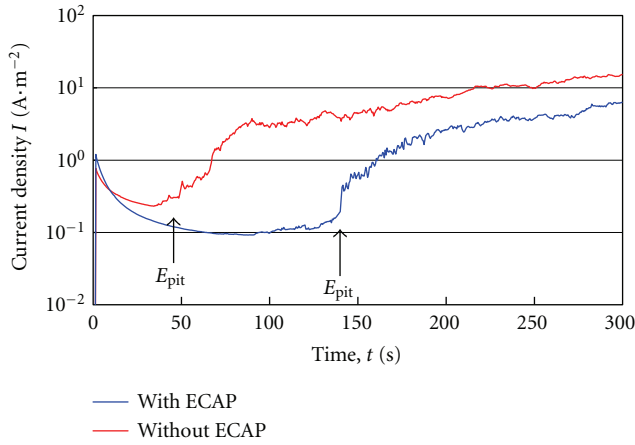


FIGURE 7: Time dependence of anodic current density of Al-Mg alloy with and without ECAP while kept at constant potential of -0.2 V in a solution containing $0.1 \text{ mol}\cdot\text{L}^{-1}$ of Na_2SO_4 and 300 ppm Cl^- .

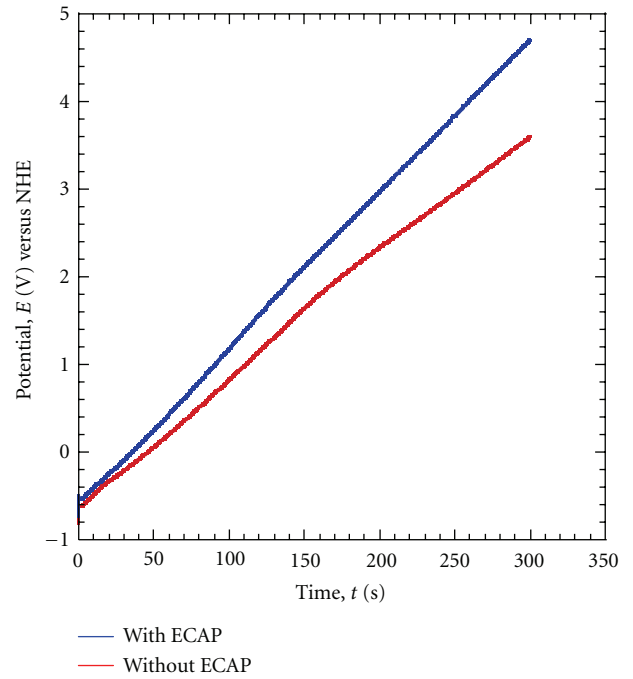


FIGURE 9: Time dependence of anodic potential of AA5052 Al-Mg alloy with and without ECAP at $1 \text{ A}\cdot\text{m}^{-2}$ in a solution containing $0.5 \text{ mol}\cdot\text{L}^{-1}$ of H_3BO_3 and $0.05 \text{ mol}\cdot\text{L}^{-1}$ of $\text{Na}_2\text{B}_4\text{O}_7$.

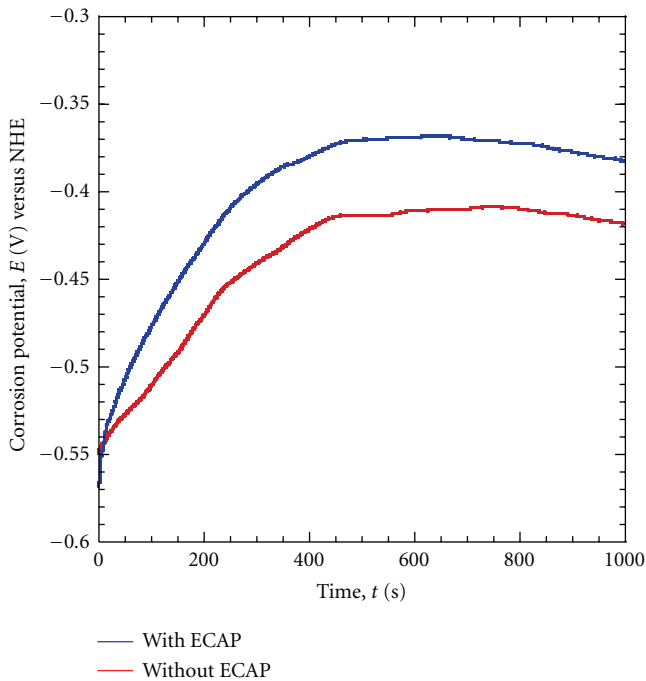


FIGURE 8: Time dependence of corrosion potential of AA5052 Al-Mg alloy with and without ECAP in a solution containing $0.1 \text{ mol}\cdot\text{L}^{-1}$ of Na_2SO_4 and 300 ppm Cl^- at 298 K .

curve of the Al-Mg alloy. The anodic current densities rapidly increased at certain potentials when the anode potentials were shifted from -0.8 V in the noble direction. This rapid increase in current density is caused by the initiation of pitting corrosion. The pitting corrosion potentials, at which pitting corrosion is initiated, were evidently shifted in the noble direction by ECAP, indicating improvement in the pitting corrosion resistance by application of ECAP. At a potential region more noble than the pitting corrosion potentials, the anodic current density was smaller with ECAP than without it, demonstrating that the corrosion resistance of the Al-Mg alloy was better with ECAP than without it.

Figure 7 shows the time dependence of the anodic current density of the Al-Mg alloy, while a constant potential of -0.2 V was maintained around the pitting corrosion potential. The anodic current densities of the Al-Mg alloy increased sharply after certain periods of time owing to the initiation of pitting corrosion. The time required before initiating the pitting corrosion of the Al-Mg alloy was longer with ECAP than without it. The anodic current density after pitting corrosion, or the growth rate of pitting corrosion,

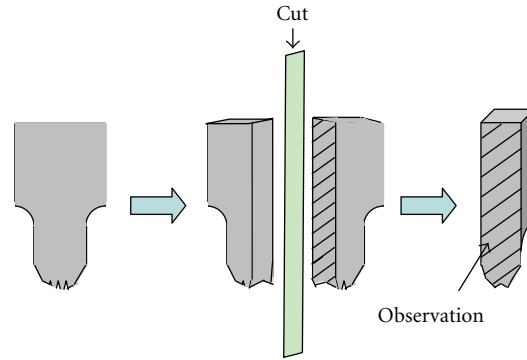


FIGURE 10: Observation area shown in Figures 11 and 12 by SEM and EBSP.

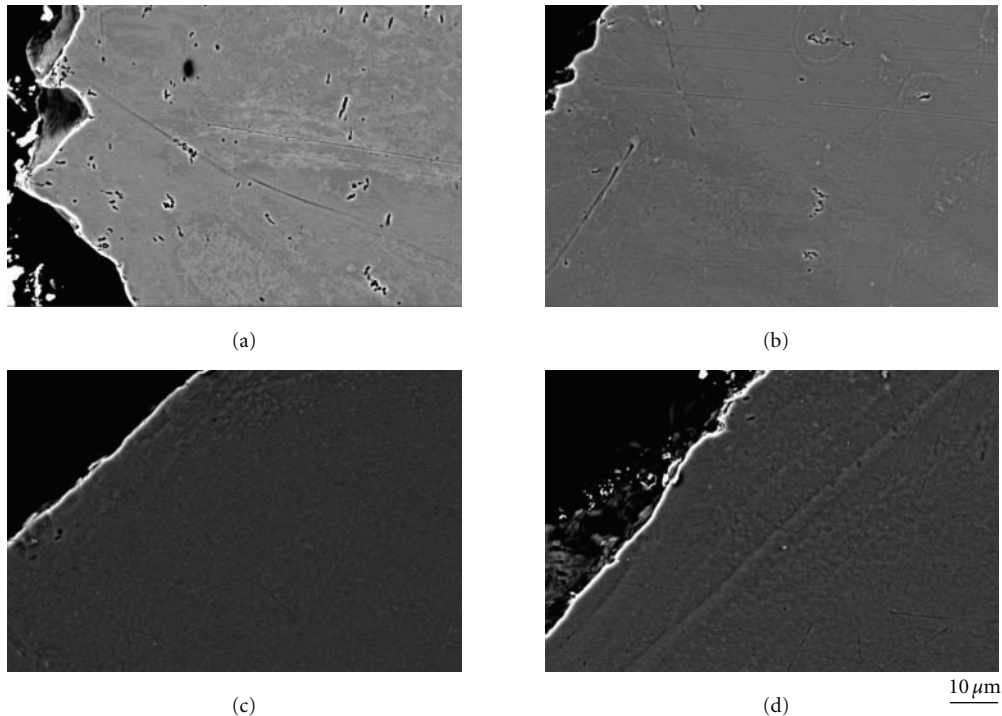
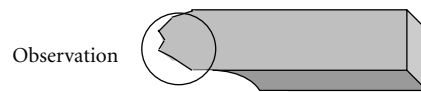


FIGURE 11: Angle-selective backscattered electron images of fracture area of Al-Mg alloy with and without ECAP after slow strain-rate tensile test. (a) Without ECAP, air (b) without ECAP, NaCl sol (c) with ECAP, air (d) with ECAP, NaCl sol.

was smaller with ECAP than without it. Further, the anodic current density before pitting corrosion was also smaller with ECAP than without it, demonstrating that the corrosion resistance of the Al-Mg alloy was better with ECAP than without it.

It has been reported that the corrosion potential of the AA5052 Al-Mg alloy in a solution containing 0.1 mol/L of Na_2SO_4 and 300 ppm of Cl^- at 298 K shifted in the noble direction faster with ECAP than without it (Figure 8)

[12, 13]. Further, the time dependence of anode potentials of the AA5052 Al-Mg alloy at 1 A/m^2 in a solution containing 0.5 mol/L of H_3BO_3 and 0.05 mol/L of $\text{Na}_2\text{B}_4\text{O}_7$ to form the barrier type of Al oxide film has been reported to show a faster shift of anode potential in the noble direction with ECAP (Figure 9) [12, 13]. Figures 8 and 9 suggest that the rate of formation of Al oxide films increases with ECAP. Since the Mg content of Al-Mg alloy used in this study is relatively close to AA5052, Al-Mg alloy in this study seems to show

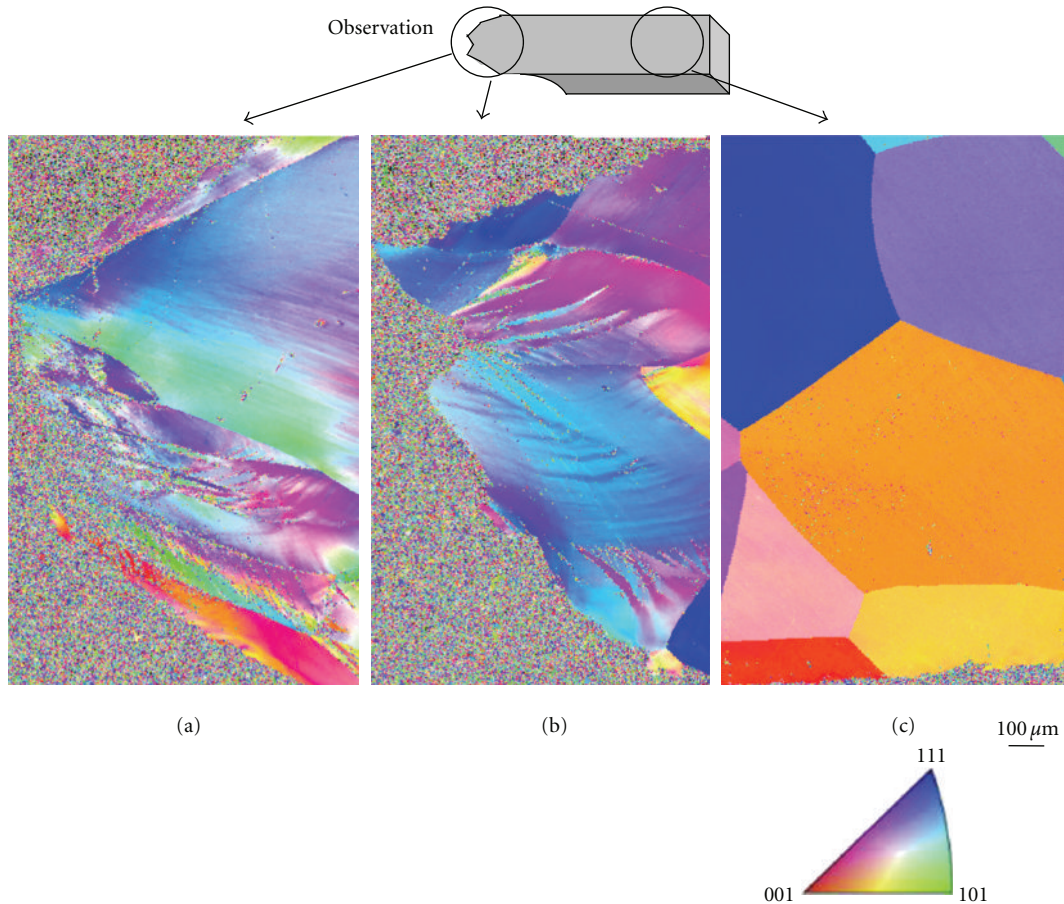


FIGURE 12: Crystal orientation mapping images of fracture area of Al-Mg alloy without ECAP after slow strain-rate tensile test. (a), (c) air (b) NaCl sol.

identical trend concerning the formation of Al oxide films with AA5052. It is well known that the oxidation reaction of metal occurs more quickly at crystalline lattice defects, such as grain boundaries and dislocations [1, 2]. The ECAP process markedly increases the number of grain boundaries and the dislocation density in Al. The oxidation rate of Al appears to increase as a result of the increase in the grain boundary and dislocation density caused by ECAP. It has been reported from electron microscope observations that multiple pitting corrosion occurred at the initial stage, but only pits that grow readily at the initial stage ultimately develop into macropits, since most pits are unstable and are immediately repassivated [2]. The specimen that quickly forms oxide films seems to be immediately repassivated, resulting in no growth of pitting corrosion, even when pitting corrosion occurs at the initial stage. In this study, the improvement of corrosion resistance with ECAP can be ascribed to the increase in the oxidation rate due to the decreased grain size of Al. The decrease in $I(\sigma_{\max})$ and $I(\delta)$ of the Al-Mg alloy with ECAP can be attributed to improvement of corrosion resistance with ECAP.

3.2. Observation of Fracture Area after Slow Strain-Rate Tensile Test. The specimen was cut at the center, as shown in

Figure 10, and was embedded in a conductive resin followed by mirror polishing and Ar sputtering to investigate the internal texture after tensile test. Figure 11 shows angle-selective backscattered electron images of the fracture area of the Al-Mg alloy with and without ECAP after a slow strain-rate tensile test in a 3% NaCl solution. Many voids were present in the vicinity of the fracture area without ECAP (Figures 11(a) and 11(b)), suggesting a void connection-type fracture. The number of voids was larger after the tensile test in air than in NaCl solution. Since elongation is higher in air, the voids seem to form with increasing strain. The Al-Mg alloy with ECAP showed a straight fracture at an angle of inclination of approximately 45° and rarely showed necking (Figures 11(c), 11(d)). In the Al-Mg alloy with ECAP, there was little difference in morphology between air and NaCl solution, and voids were rarely observed without ECAP.

Figure 12 shows crystal orientation mapping images of the fracture area of the Al-Mg alloy without ECAP after a slow strain-rate tensile test in air and NaCl solution. The tip of the fracture area showed a nonuniform crystal plane due to the introduction of a dislocation with deformation after a tensile test in air and NaCl solution (Figures 12(a) and 12(b)). The crystal grain deformed in air, while in the NaCl solution, the deformation was small and the fracture seemed

to originate from the grain boundary. In the Al-Mg alloy with ECAP, the crystal grain cannot be identified by EBSD because of the small grain size.

4. Conclusion

Stress-corrosion cracking property of the Al-Mg alloy processed by equal-channel angular pressing was investigated by a slow strain-rate tensile test in the NaCl solution. The susceptibility of stress-corrosion cracking was evaluated by $I(\sigma_{\max})$ and $I(\delta)$, which express the decrease ratio of maximum stress and total elongation in the NaCl solution to those in air. $I(\sigma_{\max})$ and $I(\delta)$ decreased with ECAP, showing that the susceptibility of stress-corrosion cracking was smaller with ECAP than without it. The polarization curves and the anodic current density of the Al-Mg alloy at constant potential in the NaCl solution revealed a decrease in the anodic current density with ECAP, or an improvement in corrosion resistance with ECAP. The decrease in $I(\sigma_{\max})$ and $I(\delta)$ of the Al-Mg alloy with ECAP shows that corrosion resistance is improved by ECAP.

Acknowledgment

This study was supported by the Grant-in-Aid for Scientific Research on Innovation Areas (research in a proposed research area no. 23102505) of the Ministry of Education, Culture, Sports, Science & Technology of Japan in 2011.

References

- [1] H. H. Uhlig, *Corrosion and Corrosion Control*, Sangyo Tosho, Tokyo, Japan, 1968.
- [2] G. Ito, *Corrosion Science and Engineering*, Corona, Tokyo, Japan, 1973.
- [3] S. Osaki, H. Kondo, and K. Kinoshita, "Effect of Cr addition on SCC property of Al-Mg-Si alloys," *Journal of Japan Institute of Light Metals*, vol. 55, no. 8, pp. 350–356, 2005.
- [4] S. Osaki, S. Horie, K. Kinoshita, S. Sato, M. Adachi, and T. Maeda, "Mechanical and SCC properties of rheocast 7075 based aluminum alloys," *Journal of Japan Institute of Light Metals*, vol. 55, no. 1, pp. 27–32, 2005.
- [5] H. Adachi, K. Osamura, and J. Kusui, "Relationship between stress corrosion resistance and microstructure of rapidly solidified Al-Zn-Mg alloys," *Journal of Japan Institute of Light Metals*, vol. 54, no. 2, pp. 69–74, 2004.
- [6] R. Z. Valiev, N. A. Krasilnikov, and N. K. Tsenev, "Plastic deformation of alloys with submicron-grained structure," *Materials Science and Engineering A*, vol. 137, pp. 35–40, 1991.
- [7] R. Z. Valiev, R. K. Islamgaliev, and I. V. Alexandrov, "Bulk nanostructured materials from severe plastic deformation," *Progress in Materials Science*, vol. 45, no. 2, pp. 103–189, 2000.
- [8] Y. T. Zhu, T. G. Langdon, R. S. Mishra, S. L. Semiatin, M. J. Saran, and T. C. Lowe, *Ultrafine Grained Materials. II*, The Minerals, Metals & Materials Society, Warrendale, Pa, USA, 2002.
- [9] Z. Horita, M. Furukawa, M. Nemoto, and T. G. Langdon, "Development of fine grained structures using severe plastic deformation," *Materials Science and Technology*, vol. 16, no. 11-12, pp. 1239–1245, 2000.
- [10] Z. Horita, "Production of ultrafine-grained structures using equal-channel angular pressing," *Journal of the Japan Welding Society*, vol. 74, no. 2, pp. 88–91, 2005.
- [11] K. Ohishi, K. Kaneko, and Z. Horita, *Materia Japan*, vol. 41, no. 6, pp. 422–426, 2002.
- [12] I. J. Son, H. Nakano, S. Oue, S. Kobayashi, H. Fukushima, and Z. Horita, "Pitting Corrosion Resistance of Ultrafine-Grained Aluminum Processed by Severe Plastic Deformation," *Journal of the Japan Institute of Metals*, vol. 69, no. 10, pp. 892–898, 2005.
- [13] I. J. Son, H. Nakano, S. Oue, S. Kobayashi, H. Fukushima, and Z. Horita, "Pitting corrosion resistance of ultrafine-grained aluminum processed by severe plastic deformation," *Materials Transactions*, vol. 47, no. 4, pp. 1163–1169, 2006.
- [14] I. J. Son, H. Nakano, S. Oue, S. Kobayashi, H. Fukushima, and Z. Horita, "Pitting corrosion resistance of anodized aluminum alloy processed by severe plastic deformation," *Journal of the Japan Institute of Metals*, vol. 70, no. 7, pp. 534–540, 2006.
- [15] I. J. Son, H. Nakano, S. Oue, S. Kobayashi, H. Fukushima, and Z. Horita, "Pitting corrosion resistance of anodized aluminum alloy processed by severe plastic deformation," *Materials Transactions*, vol. 48, no. 1, pp. 21–28, 2007.

Research Article

Determination of Susceptibility to Intergranular Corrosion of UNS 31803 Type Duplex Stainless Steel by Electrochemical Reactivation Method

Mehmet Emin Arıkan,¹ Rafet Arıkan,² and Mustafa Doruk¹

¹ Department of Metallurgical & Materials Engineering, METU, 06531 Ankara, Turkey

² Department of Mechanical Engineering, Atılım University, Incek, 06836 Ankara, Turkey

Correspondence should be addressed to Rafet Arıkan, rarikan@atilim.edu.tr

Received 25 September 2011; Revised 10 December 2011; Accepted 19 December 2011

Academic Editor: Rokuro Nishimura

Copyright © 2012 Mehmet Emin Arıkan et al. This is an open access article distributed under the Creative Commons Attribution License, which permits unrestricted use, distribution, and reproduction in any medium, provided the original work is properly cited.

Specimens taken from a hot-rolled cylindrical duplex stainless steel (DSS) bar with 22% Cr grade were solution annealed at 1050°C and then aged at 725°C from 100 to 31622 min for sensitization treatment. Double loop electrochemical potentiodynamic reactivation and standard weight loss immersion acid tests were conducted. The solution-annealed samples were found unsensitized. Those samples aged for 100 and 316 min were less sensitized whereas samples aged for 1000 min and especially those aged for 3162, 10000, and 31622 min were heavily sensitized. The degree of sensitization (DOS) can be attributed to higher contribution of chromium- and molybdenum-depleted areas resulting from intermetallic phases.

1. Introduction

Generally, duplex stainless steels (DSS) are Fe-Cr-Ni alloys having an approximately volumetric fraction of 50% ferrite and 50% austenite in their microstructures. Their main feature is that they compromise the favorable corrosion resistance of austenitic stainless steels with good mechanical properties [1–4].

In duplex stainless steels undesirable phases such as intermetallic phases (sigma and chi), carbides, and nitrides may exist if the manufacturing processes are not carefully controlled. High levels of elements stabilizing ferrite, such as chromium, molybdenum, and silicon, can promote the formation of sigma phase (σ). Sigma phase (σ) is a hard and brittle intermetallic phase, which is generally formed between 600 and 950°C with rapid formation kinetics [5–7]. Additional phases found in duplex stainless steels can include chi (χ), laves (η), and α' [8]. The nucleation sites for σ and χ phases are grain boundaries, incoherent twin boundaries, and dislocations. Duplex stainless steels are susceptible to sensitization due to the precipitation of additional phases when heated in a temperature range of 600–950°C. These

phases have a reverse effect on the corrosion and mechanical properties [6, 7]. A substantial depletion of Cr and Mo due to a copious precipitation of σ and χ phases results in a decrease of the corrosion properties [9].

There are several test methods for determining the sensitization to intergranular corrosion. Weight loss acid test was first standardized, and the test procedure was presented in ASTM A262-91 [10]. Corrosion rate is determined by measuring the weight loss of the sample. Another test method of measuring the degree of sensitization to intergranular corrosion involves electrochemical reactivation of the steel samples as defined in ASTM G108-94 [11]. This reactivation process is named as electrochemical potentiodynamic reactivation (EPR) and has been developed in single-loop (SLEPR) or in double-loop (DLEPR) types. The latter was first used for austenitic stainless steels. The best advantage of this technique is that it obtains a quantitative value of the degree of sensitization instead of an only qualitative appreciation as metallographic etchings. The EPR test provides the degree of sensitization of the material which is proportional to the amount of chromium-depleted areas adjacent to the Cr-rich phases.

In this study, DLEPR was applied for the determination of susceptibility to sensitization of duplex stainless steel type UNS S31803 with 22% Cr grade. It is designated by X2CrNiMo 22-5-3 with the trade name SAF2205. The summary of technical literature related to austenitic-ferritic duplex stainless steels shows that the test solution for DLEPR often consists of sulphuric acid (H_2SO_4) solution with the addition of KSCN as depassivator.

The purpose of the present work was to investigate intergranular corrosion behavior of DSS in relation to the influence of the microstructure produced by different heat treatments. This is performed by solution annealing and ageing for different times up to 22 days in order to provide different microstructure and sensitization levels. Electrochemical measurements were used to determine the degree of sensitization (DOS) to intergranular corrosion. Light optical microscopy (LOM) was used to identify the different phases that form in bulk material after the heat treatments. X-ray diffraction (XRD) technique and energy dispersive system (EDS) analysis were used for microstructural evolution. Surfaces obtained after the DLEPR test and the weight loss immersion test were also observed to check the attack locations and the relationship with the chromium-depleted areas.

A similar work was performed by Arikan and Doruk [12] on the same type duplex stainless steel aged at 650°C for various periods of time. The results will be compared in Section 3.6.

2. Experimental Method

2.1. Materials and Heat Treatments. The material used in this research was a commercial type hot-rolled bar of UNS S31803 duplex stainless steel (DSS) (trade name SAF2205). The chemical composition of the steel is given in Table 1.

The specimens were cut from a wrought cylindrical bar of 100 mm in diameter and 200 mm in length. The specimens were also in a cylindrical shape of 10 mm in diameter and 20 mm in length. They were taken from the bar in an orientation parallel to the rolling direction. In order to homogenize the structure, all specimens were subjected to a solution heat treatment at 1050°C for 1 hour and then quenched in water, followed by ageing heat treatments at 725°C for various periods of time.

2.2. Metallography. After heat treatments, the surfaces of the specimens were ground from 400 to 2000 grit emery paper. For microstructure examination, the surfaces of the specimens were polished with 9 and $1\ \mu\text{m}$ diamond paste. For metallographic examination, they were etched in NaOH solution as described in ASTM A923 [13]. It colors the phases in duplex stainless steel such as austenite in white, ferrite in light brown, sigma in dark brown, and carbides in black.

2.3. Weight Loss Test. The weight loss test was done according to ASTM A923-03 Test Method C standard. The test solution was prepared by dissolving 100 g of reagent grade ferric

TABLE 1: Chemical composition of 2205 DSS (wt.%).

C	Cr	Ni	Mo	Mn	Fe
0.026	22.04	4.45	2.69	1.49	Ret.

chloride ($\text{FeCl}_3 \cdot 6\text{H}_2\text{O}$) in 900 mL of distilled water (6% FeCl_3 by weight). The pH of the solution was adjusted to approximately 1.3 by addition of HCl or NaOH. The corrosion rate was evaluated as the rate of weight loss in mg per $\text{sq}\cdot\text{dm}$ per day (mdd).

2.4. X-Ray Diffraction Analysis. The chemical composition and the profile line analysis of the phases were carried out by EDS with SEM. The presence of different phases was also identified by X-ray diffraction patterns by means of Rigaku diffractometer with $\text{Cu } K_\alpha$ radiation.

2.5. DLEPR Tests. The susceptibility of the aged DSS to intergranular corrosion was evaluated using DLEPR test according to ASTM G108 standard [11]. The test was performed according to the recommendations of Majidi and Streicher [14, 15]. The standard solution is modified to suit duplex stainless steels and consisted of 2 M H_2SO_4 + 0.5 M NaCl + 0.01 M KSCN at $30 \pm 1^\circ\text{C}$. The test cell consisted of a 1 litre flask with necks for electrodes. A cylindrical working electrode was centrally located, and two counter electrodes were placed next to specimen to improve the current distribution. The specimen was mounted according to Stern-Makrides arrangement [11].

The potential was scanned with a rate of 15 V/hour in the anodic direction from a potential lower than E_{corr} in the cathodic region to a point of 0.250 V in middle of the passive region. The scanning direction was then reversed, and hence two loops are generated. The peak activation current (I_a) and the peak reactivation current (I_r) were measured during the forward and backward scans, respectively. The degree of sensitization (DOS) was thus measured as the ratio of the maximum current densities, $(I_r/I_a) \times 100$ [14, 15].

The activation or critical current density (I_a) or (I_{crit}) is proportional to the corrosion rate of a metal. The rate of corrosion rises rapidly in the activation range up to the activation peak current density. The potential corresponding to this is called activation peak potential E_a or passivation potential E_{pass} . If the potential is raised further, the anodic current will drop to a lower value called passivation current density (I_{pass}), and then it will remain constant over a wide potential range. This is the passive range in which a thin invisible film of oxide covers the metal surface. This protective film acts as a barrier between the metal and its environment and reduces the rate of dissolution.

During the anodic sweep, the entire surface is active and contributes to the peak current. But during the reactivation sweep, only the sensitized regions contribute to the passive-active transition. The unsensitized specimens show a small I_r and results in a small (I_r/I_a) ratio. On the other hand, in heavily sensitized specimens, I_r approaches I_a resulting in a high (I_r/I_a) ratio.

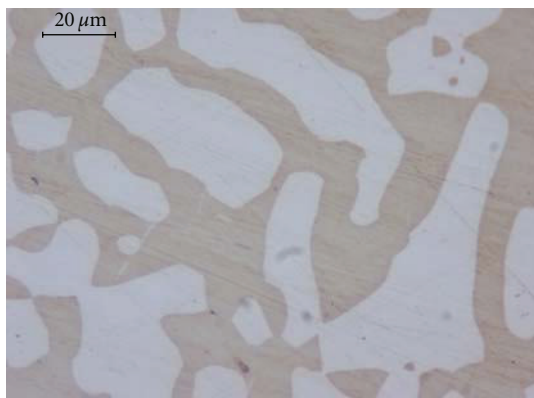


FIGURE 1: Microstructure of DSS, solution annealed at 1050°C for 1 hour (austenite in white, ferrite in gray).

3. Results and Discussion

3.1. Metallographic Examination. The optical micrographs obtained by etching with NaOH reagent are given in Figures 1 and 2. Figure 1 represents the microstructure of solution-annealed parent alloy in which white phase is austenite (γ) and the dark phase is ferrite (α). The volume fractions of α and γ were 0.54 and 0.46, respectively. The microstructure does not reveal any visible precipitates of other phases.

To study the influence of the microstructure on degree of sensitization (DOS), the specimens were aged at 725°C for times 100, 316, 1000, 3162, 10000 and 31622 min. The ageing heat treatments induced a marked change in the ferrite/austenite ratio caused by the transformation [16]



where γ_2 is the so-called secondary austenite. The nucleation rate [17, 18] and the growth kinetics of this reaction have been studied extensively [19]. It is well known that the controlling step is the nucleation rate. The growth of sigma phase causes a decrease in chromium and molybdenum content of the neighboring ferrite which becomes unstable and transforms into new austenite. This austenite, in turn, is rich in chromium and molybdenum and has a lower content of nickel if compared with the neighboring primary austenite. These changes in chemical composition promote the formation of an additional sigma phase. The overall result is the coprecipitation of secondary austenite and sigma.

For specimens aged at 725°C, microstructural changes are shown in Figures 2(a) and 2(f). For ageing from 100 to 316 min, the first tiny precipitates of sigma phase appear at α/γ and α/α boundaries. Incoherent twin boundaries and dislocations inside the ferrite matrix may also be the nucleation sites for precipitation [20]. The precipitations of σ -phase were first encountered after ageing for 316 min and the size and amount of σ phase increased with ageing time. Nucleation and growth of σ -phase are thermally activated processes involving diffusion. Therefore, temperature will have a significant effect on the kinetics of the transformation. After 1000 min, a lot of sigma precipitates have developed at

α/γ , α/α , and inside the ferrite phase as shown in Figures 2(c) and 2(f). Longer ageing treatment leads to the increase and coarsening of the σ phase in an irregular shape.

3.2. Phase Volume Fraction by Light Optical Microscopy. Microanalysis reveals that the solution-annealed material consists of ferrite and austenite phases. The main microstructural change during ageing is the formation of σ -phase and secondary austenite (γ_2) from the ferrite phase due to the eutectoid reaction ($\alpha \rightarrow \sigma + \gamma_2$). The amounts of phases were estimated by measuring the fractions of colored area on polished and etched specimens by light optical microscopy (LOM). The measured volume fractions of ferrite, austenite, and sigma phases for different ageing times are given in Table 2 and Figure 3. Since the ferrite transforms into σ and γ_2 , the ferrite phase decreases as the volume percentages of sigma and secondary austenite increase with ageing time until the whole ferrite is totally consumed. Ferrite continuously decreases throughout each of the isothermal holds and reaches zero at the end of the 31622 min. The total austenite is considered as the sum of the primary and secondary austenite ($\gamma + \gamma_2$) and increases to the value of 57% by time.

During the early stages of the transformation, sigma forms preferentially at the α/γ and α/α grain boundaries and inside the α -grain and grows into the ferrite phase via a transformation mechanism involving diffusion. Because both nucleation and diffusional growth of σ are thermally activated processes, the ageing time and temperature will have a significant effect on the kinetics of the transformation. The time at which sigma was first observed was 316 min at 725°C.

3.3. Weight Loss Test Results. The degree of sensitization is also given by the loss of weight due to the dissolution of chromium-depleted areas and is expressed as the rate of weight loss in mdd. The results of standard weight loss immersion test are given in Table 3 and plotted in Figure 4. Corrosion rate of the specimens aged at 725°C is low up to 1000 min and then increases rapidly up to 31622 min. Moreover, the lower chromium and molybdenum content is not the only factor responsible for the increase in the rate of corrosion. The neighborhood of more noble phases (sigma phase) will enhance the anodic dissolution of secondary austenite extensively.

The surfaces of the corroded specimens were examined using LOM. The localized attack in black points is initiated in the secondary austenite phase adjacent to the sigma phase as shown in Figure 5. The austenite and the sigma phase resist the ferric chloride solution more than the ferrite and the secondary austenite. Once a pit is formed it rapidly propagates within the initial ferrite region. As a result, it is observed that the sigma and austenite phases are almost intact, while the secondary austenite (γ_2) and some iron rich ferrite phases are attacked.

3.4. EDS Analysis of Phases. The precipitation of the intermetallic sigma phase is accomplished by the formation

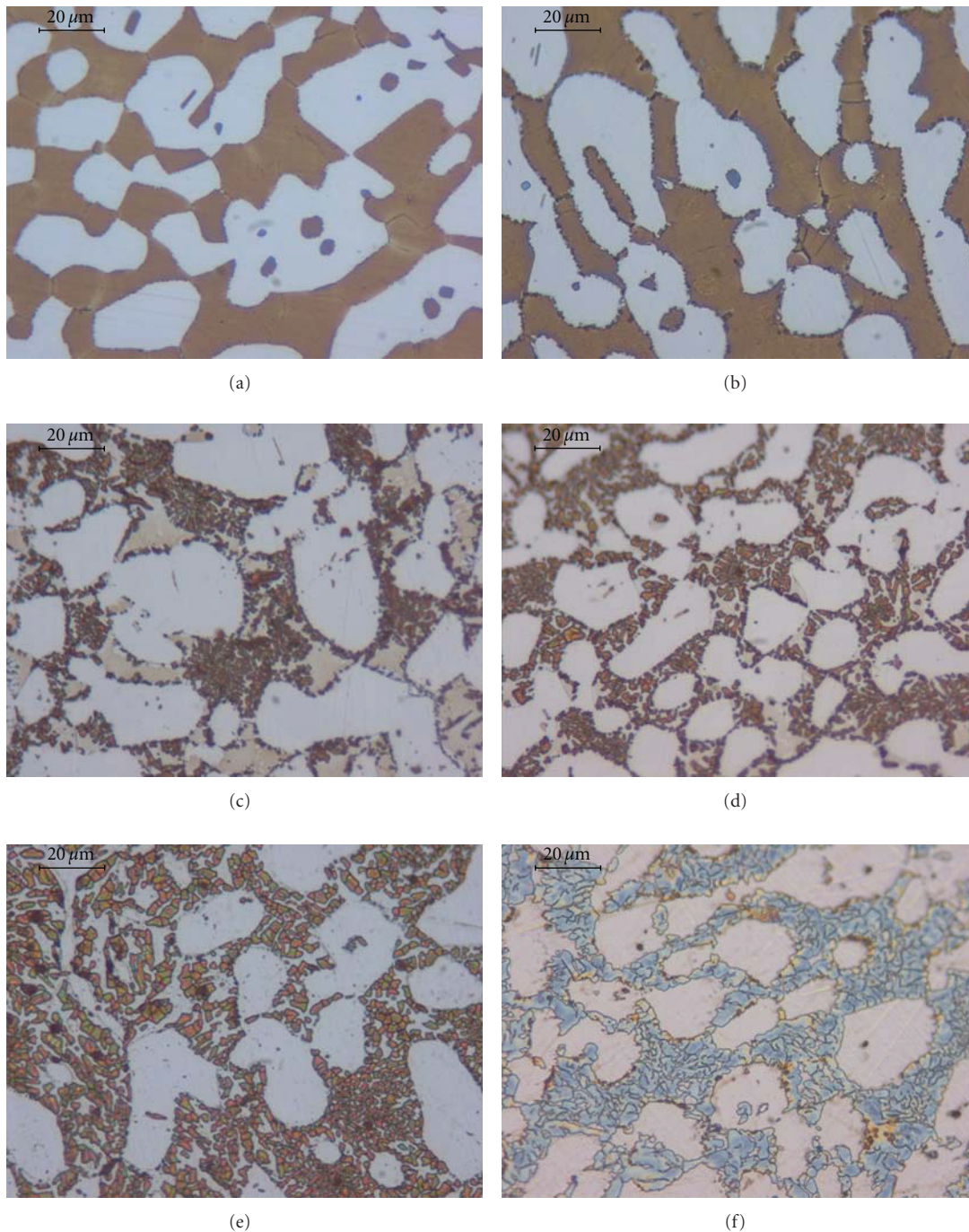


FIGURE 2: Optical micrographs obtained after ageing at 725°C by etching with NaOH reagent (a) 100 min, (b) 316 min, (c) 1000 min, (d) 3162 min, (e) 10000 min, (f) 31622 min (austenite in white, ferrite in gray, sigma precipitates in black).

of secondary austenite (γ_2). As the sigma phase grows, chromium and molybdenum are enriched in these precipitates, and, simultaneously, nickel diffuses into the ferrite. The enrichment of γ -stabilizing elements (such as Ni) in the ferrite and the loss of ferrite stabilizing elements (such as Cr and Mo) lead to an unstable ferrite transforming into secondary austenite depleted in chromium and molybdenum [20].

The EDS measurements of Cr, Mo, Ni, Mn, and Fe content of the α , γ , σ , and γ_2 phases present in samples of solution annealed and aged for 31622 min are given in Table 4. During the growth of sigma phase, these elements diffuse from the surrounding ferrite matrix to the sigma phase, and this causes depletion in these elements. The depletion in chromium and molybdenum leads to the transformation of the region to secondary austenite (γ_2).

TABLE 2: The phase volume percentages obtained from digital image analysis.

Heat treatment	Ageing time (min)	Ferrite phase (vol. %)	Austenite phase ($\gamma + \gamma_2$) (vol. %)	Sigma phase (vol. %)
Solution annealed at 1050°C, 1 h		54.55	45.45	0
Solution annealed at 1050°C, 1 hr + aged at 725°C	100	54	46	0
	316	53.2	46.2	0.6
	1000	32	49	19
	3162	15	52	33
	10000	6	54	40
	31622	0	57	43

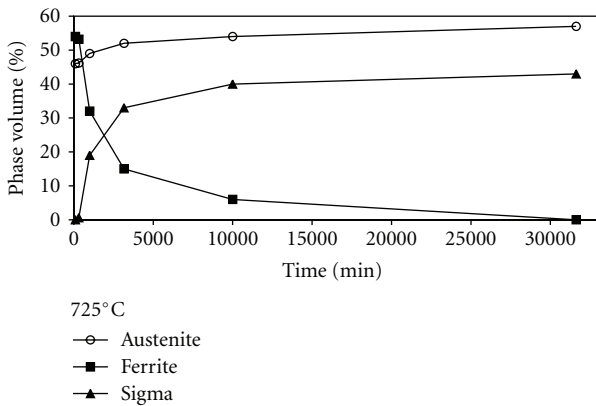


FIGURE 3: Changes in volume % of austenite, ferrite, and sigma phases with ageing time at 725°C.

TABLE 3: Weight loss immersion acid test results according to ASTM A 923-03.

Ageing time (min)	Weight loss (mdd)
100	0.49451
316	2.37328
1000	5.38945
3162	5.16104
10000	5.28002
31622	6.04718

3.5. X-Ray Diffraction Pattern. The results of the X-ray diffraction analysis consist of a series of diffraction patterns given in Figure 6. The diffraction pattern of the solution-annealed parent alloy presents ferrite and austenite phase peaks only. Samples aged at 725°C for different ageing times show the peaks of phases developed.

Although the precipitations at grain boundaries are evident for 316 min of ageing as shown in light optical micrograph of Figure 2(b), the X-ray spectra of the sample do not reveal any sigma peak. This may be attributed, as given in Table 2, to the very low volume fraction of the sigma phase (0.6%).

Samples aged at 725°C show sigma peaks first in 1000 min of ageing. With increased holding time, the intensity of sigma peaks increases as the volume fraction of sigma phase increases (Table 2), and also additional sigma

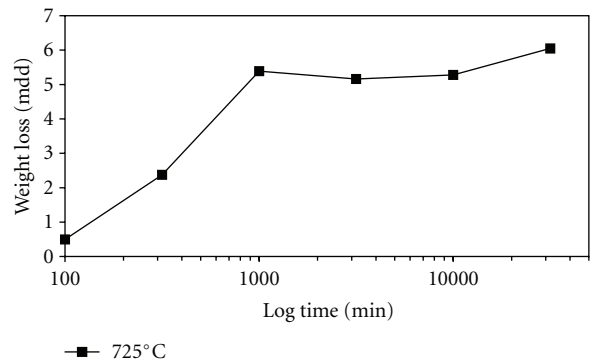


FIGURE 4: The change in weight loss with ageing time.

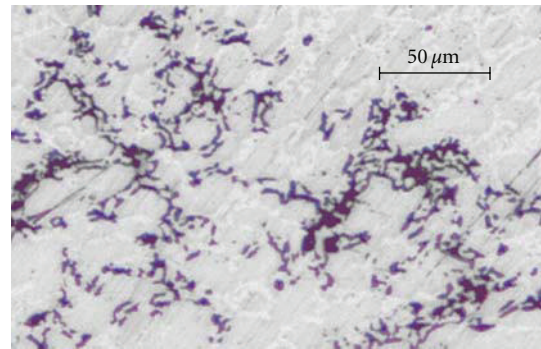


FIGURE 5: Dissolution of the secondary austenite in weight loss test (black: attacked region in the secondary austenite phase adjacent to the sigma phase, gray: austenite, and white: sigma).

peaks appear. After 3162 min of ageing, one of the ferrite phase peaks decreases to nearly zero but the other peak does not disappear; it overlaps with a sigma phase peak. After longer periods of time such as 10000 min, the treatments promote the transformation of ferrite phase. This results in a noticeable decrease in the intensity of the α and an increase of γ peaks. The decrease of the ferrite peak intensity indicates that the major fraction of ferrite is transformed into sigma. Consequently several sigma peaks are observed. All the changes observed in the diffraction peak intensity do correlate well with the changes in volume fraction of each phase during the isothermal hold as given in Table 2.

TABLE 4: EDS analysis of phases present in solution-annealed and aged condition of DSS.

Heat treatment	Phase	Cr (wt. %)	Ni (wt. %)	Mo (wt. %)	Mn (wt. %)	Si (wt. %)	S (wt. %)	Fe (wt. %)
Solutionannealed	General composition	22.04	4.45	2.69	1.49	0.45	0.003	68.29
Solution annealed	α	26.32	4.87	4.15	1.59	0.74	—	62.32
	γ	23.55	7.08	—	1.85	—	1.19	66.33
725° C/31622 min	γ	23.81	6.43	—	—	—	—	69.76
	σ	35.21	—	7.21	—	—	—	57.58
	γ_2	23.03	6.91	—	—	1.04	1.26	67.75
	γ_2	18.65	5.21	—	—	—	—	76.14

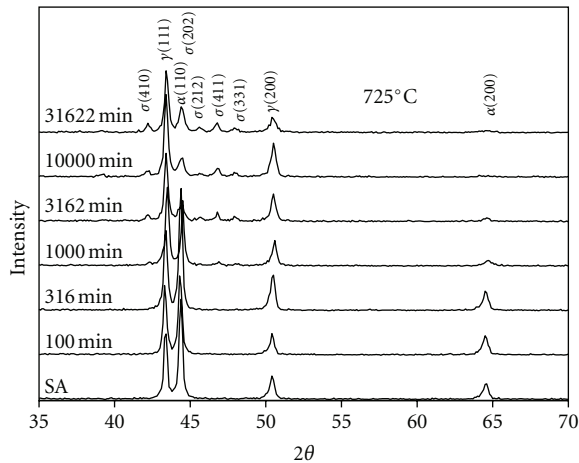


FIGURE 6: X-Ray diffraction patterns of samples aged at 725°C.

3.6. DLEPR Results. Figure 7 shows the polarization curves for samples in solution-annealed and aged condition. The curve obtained from the solution-annealed sample is treated as a reference and compared with the others. The activation peak current density of the reference curve is 23.13 mA/cm², and the corresponding activation peak potential (E_a) or passivation potential (E_{pass}) is -212.78 mV with respect to saturated calomel reference electrode (SCE). This peak reaches a maximum and then fall, to a low passive current density (I_{pass}) of 0.001448 mA/cm² before reaching the chosen reverse potential of +250 mV. The sample is thus passivated in a wide range between -212.78 mV and +250 mV. In this passive range, a thin invisible film of oxide may cover the metal surface. The protective film acts as a barrier between the metal and its environment and reduces its rate of dissolution. And hence, the I_r/I_a ratio is very low (0.027634%). This may be considered as unsensitized material (Table 5).

From the samples aged for 100 min, any visible precipitate is not observed either optically (Figure 2(a)), or in XRD analysis (Figure 6). After ageing for 316 min, sigma phase nucleation starts at α/γ phase boundaries as shown in Figure 2(b), but the diffraction pattern (Figure 6) does not reveal any evidence due to very small amount of the sigma phase (0.6%), (Table 2). The samples aged for 100 and 316 min present very small reactivation currents (Table 5), and hence the I_r/I_a ratios are 5.76 and 6.48%, and accordingly the corrosion rates become 0.49451 and 2.37328 mdd,

respectively. This means slight chromium depletion resulting in a less sensitization.

After 1000 min, the σ precipitates have grown at the boundaries and within the ferrite grains. Next to the growing σ -phase, the secondary austenite (γ_2) forms from the decomposition of ferrite into σ and γ_2 (Table 2). Dissolution of the secondary austenite results in greater weight loss (5.38 mdd) (Table 3) and accordingly a high ratio of I_r/I_a (53.42%) (Table 5). This means that the sample has been highly sensitized.

After 3162 min of ageing, a substantial decrease in chromium content of the interfaces and around the precipitates reduces the corrosion resistance and makes the alloy more susceptible to localized attacks. This leads to the highest grade of sensitization, and thus the DOS value reaches 93.189% (Table 5), and dissolution of the secondary austenite (γ_2) results in a corrosion rate of 5.161 mdd (Table 3).

Similar results were obtained for the same reasons after ageing for 10000 and 31622 min. The corresponding DOS are 90.4 and 92.39%, and the mdd values are 5.28 and 6.04 respectively, showing the samples being heavily sensitized (see Table 5 for comparison).

When the polarization curves of the samples aged at 725°C from 100 to 31622 min are compared with the reference curve, it is seen that the activation peak current density increases with increasing ageing times (Table 5). And also the passive current density increases from 0.033688 mA/cm² up to 0.059391 mA/cm², and the passivation potential (E_{pass}) decreases from -212.78 mV to -172.23 mV.

From the results discussed so far considering weight loss acid test and DLEPR test, it can be concluded that both the sensitization and the corrosion rate have increased with respect to the depletion of chromium and molybdenum in the ferrite region.

Chromium diffusion is much faster in ferrite than in austenite. The chromium concentrates in the neighboring sigma phase [21] and causes the sigma phase to grow fast within the ferrite region. As a result, the formation of the secondary austenite can degrade the stability of the passive film [22].

After the DLEPR test, a sample aged for 31622 min was slightly polished and examined with LOM (Figure 8(a)) to check the attack locations and the relationship with the chromium-depleted areas.

Observation of the surface indicates that the sigma and austenite phases are almost intact, while the secondary

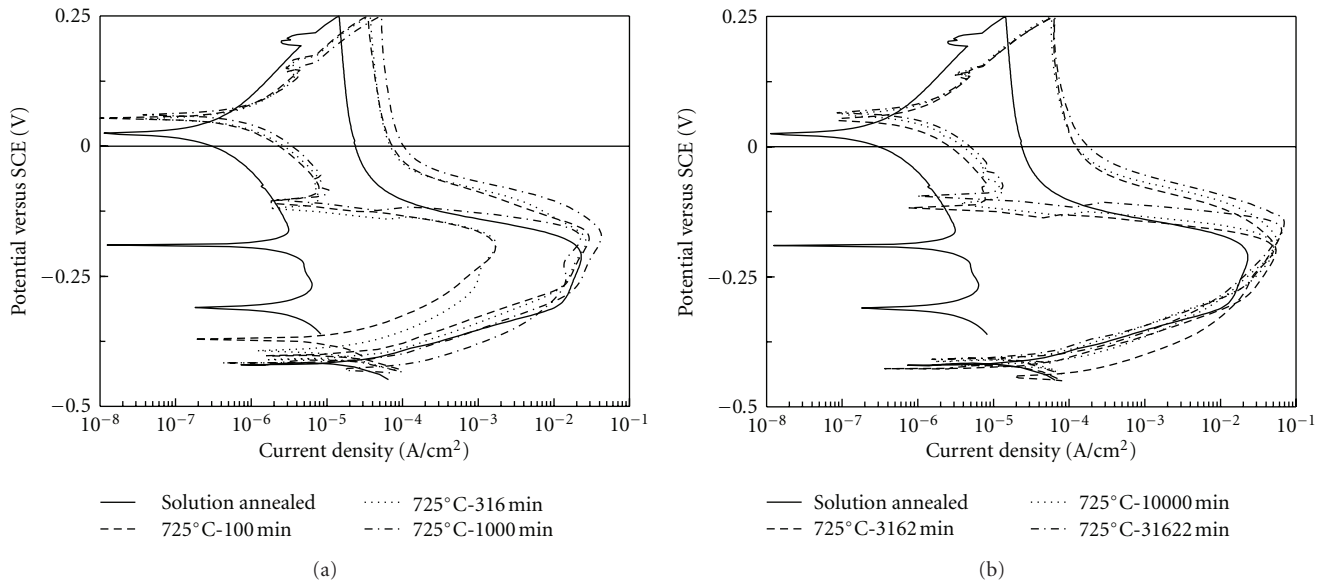


FIGURE 7: DLEPR curves plotted for DSS after solution and sensitization heat treatments at 725°C between 100 and 31622 min (scan rate: 15 V/hr).

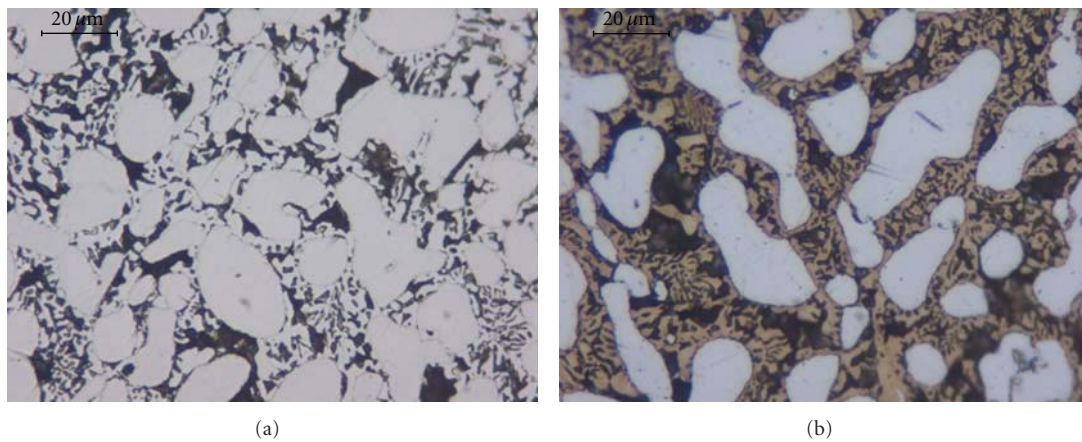


FIGURE 8: Optical micrographs after DLEPR test for sample aged at 725°C for 31622 min (a) after slightly polished (large austenite in white, attacked regions in black, sigma: small white regions) (b) electrolytically etched with NaOH (austenite in white, sigma in brown, attacked regions in black).

TABLE 5: DLEPR Test results of 2205 type duplex stainless steel.

Temperature (°C)	Time (min)	Activation peak potential, E_a (mV)	Activation peak current density, I_a (mA/cm ²)	Reactivation peak potential, E_r (mV)	Reactivation peak current density, I_r (mA/cm ²)	Passivation current density, I_{pass} (mA/cm ²)	DOS ($I_r/I_a \times 100$)
Solution annealed at 1050°C, 1 hr		-212.78	23.1304849	-267.33	0.0063918	0.001448	0.027634
Solution annealed at 1050°C, 1 hr + aged at 725°C	100	-178.33	29.2261754	-196.13	1.6857088	0.033688	5.767805
	316	-185.25	26.5737074	-189.43	1.7231466	0.037542	6.484404
	1000	-172.22	42.2727750	-177.35	22.5825614	0.052615	53.421053
	3162	-199.68	54.2137581	-195.70	50.5214698	0.062409	93.189389
	10000	-183.47	55.7856777	-191.11	50.4425582	0.057675	90.422059
	31622	-147.94	69.6430296	-160.30	64.3463484	0.059391	92.394528

austenite and some iron rich ferrite phase are attacked. The corroded secondary austenite regions appear in black, and the isolated sigma precipitates in white. Large primary austenite grains remain in white as usual. To distinguish sigma and primary austenite phases in color, the samples were electrolytically etched with NaOH reagent. The sigma phase is colored reddish brown and distinguished from the primary austenite which was not affected from the etchant (Figure 8(b)).

When compared to the acid test samples (Figure 5), the DLEPR specimens showed a similar behavior, because the same areas were affected in both cases. In other words the attacks have occurred at sensitized areas. The appearance of the localized attack after immersion testing shows large number of black points clearly. This shows that local corrosion is initiated in the secondary austenite phase as happened in the DLEPR test samples. Once a pit is formed, it rapidly propagates within the initial ferrite region. After a long time of exposure, the corroded area extended and covered a large area including many sigma and austenite phases. As a result large cavities were developed. This type of corrosion is known as localized corrosion.

As mentioned before, Arikian and Doruk presented a study [12] dealing with DLEPR and standard weight loss acid tests for the same type of duplex stainless steel annealed at 1050°C for 1 hour and aged at 650°C for various periods of time.

Comparison of the results obtained from samples aged at 650 and 725°C indicates that the minimum time where sigma was first observed is less than 316 min at 725°C and longer as 1000 min at 650°C. Both DLEPR and acid tests expose continuous chromium-depleted zones leading to intergranular corrosion at α/γ phase boundaries and local corrosion around sigma phases precipitated inside the ferrite region.

Corrosion rate of samples aged at 650°C is very low up to 1000 min and then increases up to 31622 min, whereas the rate for samples aged at 725°C is very low only for 100 min of ageing and then rapidly increases with ageing time (Table 3).

A similar trend for DOS values was observed at 650 and 725°C, but since ferrite decomposition occurs faster at 725°C, accordingly sensitization begins in shorter time of ageing than that at 650°C. This indicates that The DLEPR test provides results proportional to σ -phase content.

As a result, in both cases, the sensitization and corrosion rate depend strongly on the extent of chromium and molybdenum depletion. The important difference is the depletion to be delayed at 650°C.

Only the solution-annealed samples and the samples aged at 650°C for 100 and 316 min are unsensitized but samples aged at 650°C for 10000 and 31622 min are heavily sensitized. Similarly, samples after 1000 min of ageing at 725°C are sensitized as well.

3.7. Analysis of Polarization Curves in Reverse Scanning. At the beginning of the reverse scanning, the anodic current density decreases, and the anodic curve moves to the left (Figure 7). This is an indication of thickening of the oxide film. On decreasing the potential, the anodic current density

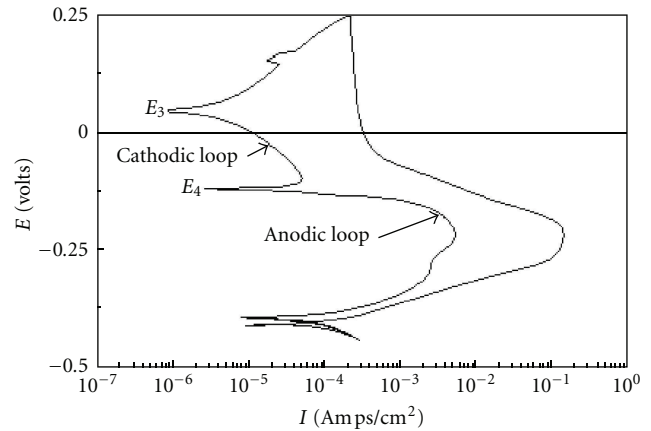


FIGURE 9: Cathodic and anodic loops in DLEPR curve.

is reduced nearly to zero. This is due to the slowing of the anodic dissolution kinetics caused by thickening of the passive film. The sample has thus continued to passivate from E_{pass} through E_{rev} , back to potential E_3 . Further reducing the potential, the direction of the current density has changed between E_3 and E_4 as shown in Figure 9. It shows a loop consisting of cathodic current [23]. The origin of the cathodic current can be attributed to the fact that at potentials between E_3 and E_4 , the rate of the cathodic reaction is greater than the anodic current density, and hence the net current is cathodic over the potential range, $\Delta E (= E_3 - E_4)$ (Table 6). If the potential is further reduced on the reverse scan, the direction of the current density changes back, and an anodic reactivation loop is generated. This indicates that the oxide has dissolved, and metal dissolution reaction has occurred. The development of the reactivation peak current density (I_r) can be attributed to metal dissolution. The lowered reactivation peak current density I_r (on the reverse scan) is due to incomplete reactivation of the metal surface.

If no cathodic loop was generated on the reverse scan, the anodic reactivation would begin at a higher potential and would likely reach a high value of I_r in a short time, and thus the metal dissolution would take place.

The same cathodic loop behavior is observed on the reverse scans of polarization curves obtained from the solution annealed and aged samples by DLEPR test (Table 6).

The potential ranges (ΔE) of samples aged at 725°C from 100 and 31622 min where the cathodic loops are obtained, are different from that of the solution-annealed sample. In general, their reactivation curves look like that of the solution-annealed sample. A similar cathodic loop behavior has been observed for all cases but the anodic loops do not resemble that of the solution-annealed sample. This indicates that the precipitates developed in the microstructure influence the polarization behavior.

For all cases, the potential ranges (ΔE) for the cathodic loops change disorderly from 0.159 to 0.171 and are less than that of the solution-annealed sample. This means that the formation of the cathodic loop delays the occurrence of the anodic reactivation current loop for a short time. Then, the direction of the current density changes back quickly, and

TABLE 6: DLEPR test results on the reverse scans of polarization curves.

Temperature (°C)	Time (min)	E_3 (volt)	E_4 (volt)	$\Delta E (= E_3 - E_4)$ (volt)	I_r (mA/cm ²)	DOS ($I_r/I_a \times 100$)
Solution annealed at 1050°C, 1 hr		0.02521	-0.190090	0,215300	0.0063918	0.027634
	100	0.053818	-0.110000	0.163818	1.6857088	5.767805
Solution annealed at 1050°C, 1 hr + aged at 725°C	316	0.052163	-0.119650	0.171813	1.7231466	6.484404
	1000	0.060101	-0.103310	0.163411	22.5825614	53.421053
	3162	0.050114	-0.117800	0.167914	50.5214698	93.189389
	10000	0.063035	-0.108430	0,171465	50.4425582	90.422059
	31622	0.064701	-0.095247	0.159948	64.3463484	92.394528

the anodic reactivation current density begins to be generated at a potential of $E_4 = -0.110000$ V for ageing 100 min and at $E_4 = -0.119650$ V for ageing 316 min. It then reaches the peak value of $I_r = 1.6857088$ A/cm² with the DOS value of 5.76% for ageing 100 min, and $I_r = 1.7231466$ A/cm² with the DOS value 6.48% for ageing 316 minutes.

For the sample aged for 1000 min, the potential range for the cathodic loop is 0.163411 V. This is lower than the value measured for the solution-annealed one. The dissolution of oxide begins at a high potential such as $E_4 = -0.103310$ V. After a short delay, the reactivation current density increases to $I_r = 22.5825614$ A/cm². The DOS value is 53.42%.

For the sample aged for 3162 min, the range of the potential for the cathodic loop is 0.167914 V. This is higher than the value obtained for 1000 min of ageing. The E_4 ($= -0.117800$ V) has been found higher and E_3 ($= 0.050114$) lower with increasing ageing time. The reactivation peak current density (I_r) has reached 50.52146 mA/cm² corresponding to a high DOS value (93.18%).

For ageing time of 10000 and 31622 min, cathodic loops on the reverse scan are obtained within a potential range of 0.171465 and 0.159948 V, respectively. And then the anodic reactivation loops suddenly begin at higher potentials of E_4 such as -0.108430 and -0.095247 V. The reactivation peak current densities (I_r) have reached to 50.442 and 64.346 mA/cm², and the corresponding DOS values are 90.422 and 92.394%, respectively. This is because of the change in the microstructure. Due to longer ageing treatments the whole ferrite has transformed into σ and γ_2 . Dissolution of the secondary austenite results in greater weight losses and higher ratios of I_r/I_a . The higher anodic peak reactivation current density is the result of complete activation of the metal surface as evident by the high DOS values.

A similar behavior has been observed for the passive current densities (I_{pass}). The chromium depletion or dissolution of secondary austenite phase (γ_2) causes the passive current densities to shift to higher current densities as compared to that obtained from the solution-annealed sample (Figure 7, Table 5).

4. Conclusions

The effect of isothermal treatment at 725°C on the microstructures and consequent corrosion behavior of a duplex

stainless steel UNS S31803 was investigated. The important findings are summarized as follows.

(a) Only the solution-annealed sample was found unsensitized. The structure is free of precipitations, and consequently it presented a very small reactivation current. From the DOS values of specimens aged for 100 and 316 min., it may be concluded that these samples became less sensitized than those aged for longer ageing time. The degree of sensitization increases rapidly with increasing ageing time and this can be attributed to a higher contribution of chromium- and molybdenum-depleted areas resulting in the formation of the intermetallic phases.

(b) In a comparison to previous results [12], the sensitization of DSS was affected much by long-term ageing heat treatment at 725°C than that at 625°C.

(c) The DLEPR test showed that fine precipitates were insufficient to induce a significant susceptibility to intergranular corrosion. The role of chromium nitrides was less harmful because of the low amount of these precipitates.

(d) The intermetallic σ -phase has first precipitated at the interface of α/γ , α/α , and inside the α -ferrite grains up to 316 min ageing time. The σ -phase has then grown into coarse particles due to high diffusivity of chromium and molybdenum atoms in the ferrite matrix leaving behind a chromium-depleted zone named secondary austenite. The exposure of aged samples to iron-chloride acid media leads to a localized and selective attack on the secondary austenite.

(e) From the observations of the polarization curves it may also be concluded that cathodic loops do not affect metal dissolution. They merely delay the occurrence of anodic loops for a short time in a small potential range. These potential ranges (ΔE) over that cathodic loops are obtained depend on the protective film thickness, ageing temperature, time, and microstructural changes in the material. Actually, during the anodic sweep, the entire surface is active and contributes to the peak current. But during the reactivation sweep, only the sensitized areas contribute to the passive-active transition. So the oxide dissolves first, and then soon metal dissolution takes place.

References

- [1] A. Wensley and C. Reid, "Duplex stainless steels in the pulp and paper industry," in *Proceedings of the Duplex Stainless Steels*, J. Charles and S. Bernhardtsson, Eds., vol. 1, pp. 1099–1110, Les Editions de Physique, 1992.

- [2] J. Husbands and P. K. Whitkraft, "High-Cr Duplex Alloy in Nitric Acid Production," CORROSION/91, Paper 171, NACE, Houston, Tex, USA, 1991.
- [3] D. J. A. Fruytier, "Industrial experiences with duplex stainless steel related to their specific properties," in *Proceedings of the Duplex Stainless Steels*, J. Charles and S. Bernhardsson, Eds., pp. 497–509, Les Editions de Physique, 1992.
- [4] P. Jolly, *Bulletin du Cercle d'Etudes des Metaux*, vol. 12, no. 5, p. 317, 1973.
- [5] J. S. Kim and H. S. Kwon, "Effects of tungsten on corrosion and kinetics of sigma phase formation of 25% chromium duplex stainless steels," *Corrosion*, vol. 55, no. 5, pp. 512–521, 1999.
- [6] M. E. Wilms, V. J. Gadgil, J. M. Krougman, and B. H. Kolster, "Effect of σ -phase precipitation at 800°C on the mechanical properties of a high alloyed duplex stainless steel," *Materials at High Temperatures*, vol. 9, no. 3, pp. 160–166, 1991.
- [7] T. H. Chen and J. R. Yang, "Effects of solution treatment and continuous cooling on σ -phase precipitation in a 2205 duplex stainless steel," *Materials Science & Engineering A*, vol. 311, no. 1-2, pp. 28–40, 2001.
- [8] T. A. Debold, "Duplex stainless steel—microstructure and properties," *Journal of Metals*, vol. 41, no. 3, pp. 12–15, 1989.
- [9] N. Lopez, M. Cid, and M. Puiggali, "Influence of σ -phase on mechanical properties and corrosion resistance of duplex stainless steels," *Corrosion Science*, vol. 41, no. 8, pp. 1615–1631, 1999.
- [10] ASTM A262-02: *Standard Practices for Detecting Susceptibility to Intergranular Attack in Austenitic Stainless Steels*.
- [11] ASTM G108-94: *Standard Test Method for Electrochemical Reactivation (EPR) for Detecting Sensitization of AISI Type 304 and 304L Stainless Steels*.
- [12] M. E. Arikian and M. Doruk, "Determination of susceptibility to intergranular corrosion of UNS 31803 type duplex stainless steel by electrochemical reactivation method," *Turkish Journal of Engineering and Environmental Sciences*, vol. 32, no. 6, pp. 323–335, 2008.
- [13] ASTM A923-03: *Standard Test Methods for Detecting Detritmental Intermetallic Phase in Duplex Austenitic/Ferritic Stainless Steels*.
- [14] A. P. Majidi and M. A. Streicher, "Potentiodynamic reactivation method for detecting sensitization in AISI 304 and 304L stainless steels," *Corrosion*, vol. 40, no. 8, pp. 393–408, 1984.
- [15] A. P. Majidi and M. A. Streicher, *paper presented at NACE, CORROSION/84*, no. 261, 1984.
- [16] P. Jolly and J. Hochmann, *Mémoires Scientifiques de la Revue de Metallurgie*, vol. 20, p. 117, 1993.
- [17] J. M. Vitek and S. A. David, "The sigma phase transformation in austenitic stainless steels," *Welding Journal*, vol. 63, no. 4, pp. 106–111, 1986.
- [18] "Duplex stainless steel: a tale of two phases," in *Proceedings of the Duplex Stainless Steels*, H. D. Solomon, T. M. Devine, and R. A. Lula, Eds., p. 693, ASM, Metals Park, Ohio, USA, 1986.
- [19] C. H. Shek, K. W. Wong, and J. K. Lai, "Review of temperature indicators and the use of duplex stainless steels for life assessments," *Materials Science and Engineering*, vol. 5-6, p. 153, 1997.
- [20] T. A. Debold, "Duplex stainless steel—microstructure and properties," *Journal of Metals*, vol. 41, no. 3, pp. 12–15, 1989.
- [21] R. N. Wright and R. A. Rula, "Toughness of ferritic stainless steels," *ASTM International*, vol. 706, p. 2, 1979.
- [22] C. J. Park and H. S. Kwon, "Effects of aging at 475°C on corrosion properties of tungsten-containing duplex stainless steels," *Corrosion Science*, vol. 44, no. 12, pp. 2817–2830, 2002.
- [23] A. Legat and V. Dolecek, "Chaotic analysis of electrochemical noise measured on stainless steel," *Journal of the Electrochemical Society*, vol. 142, no. 6, pp. 1851–1858, 1995.

Research Article

Corrosion Behaviour of Heat-Treated Aluminum-Magnesium Alloy in Chloride and EXCO Environments

S. O. Adeosun, O. I. Sekunowo, S. A. Balogun, and V. D. Obiekea

Department of Metallurgical & Materials Engineering, University of Lagos, Nigeria

Correspondence should be addressed to S. O. Adeosun, samsonoluropo@yahoo.com

Received 12 September 2011; Revised 24 November 2011; Accepted 5 December 2011

Academic Editor: Rokuro Nishimura

Copyright © 2012 S. O. Adeosun et al. This is an open access article distributed under the Creative Commons Attribution License, which permits unrestricted use, distribution, and reproduction in any medium, provided the original work is properly cited.

Machines designed to operate in marine environment are generally vulnerable to failure by corrosion. It is therefore imperative that the corrosion susceptibility of such facilities is evaluated with a view to establishing mechanism for its mitigation. In this study, the corrosion behaviour of as-cast and retrogression-reaction (RRA) specimens of aluminum alloy containing 0.4–2.0 percent magnesium additions in NaCl, FeCl₃, and EXCO solutions was investigated. The corrosion simulation processes involved gravimetric and electrochemical techniques. Results show substantial inducement of Mg₂Si precipitates at a relatively higher magnesium addition, 1.2–2.0 percent, giving rise to increased attack. This phenomenon is predicated on the nature of the Mg₂Si crystals being anodic relative to the alloy matrix which easily dissolved under attack by chemical constituents. Formation of Mg₂Si intermetallic without corresponding appropriate oxides like SiO₂ and MgO, which protect the precipitates from galvanic coupling with the matrix, accentuates susceptibility to corrosion.

1. Introduction

Aluminum and its alloys are widely used in industry because of their light weight, high strength, and good corrosion resistance which is due to the formation of a protective oxide layer. However, under saline conditions such as those encountered in marine environments, aluminum alloys are vulnerable to localised degradation in forms of pitting and crevice corrosion. This type of corrosion involves the adsorption of an anion in particular chloride ion, Cl⁻, at the oxide-solution interface.

In conventional metallic materials, the strong oxidizing power of the environment is required to establish spontaneous passivity; hence, to be of practical use, metallic materials must exhibit significant level of passivity in a given environment.

The passive stable surface film acts as a barrier for the transfer of cations from the metal to the environment and for the counter diffusion of oxygen and other anions. The air-formed film must be stable without damage to the underlying alloy surface in a given environment. Chemically homogenous, single-phase amorphous alloys free from crystalline defects such as precipitates, segregates,

grain boundaries, and dislocations often create conducive environment for the formation of uniform passive film without any weak points [1].

Aluminum forms a protective oxide film in the pH range 4.0–8.5, but this depends on temperature, form of oxide present, and the presence of substances that form soluble complexes or insoluble salts with aluminum. This implies that the oxide film is soluble at pH values below 4.0 and above 8.5. However, Sziklarska and Smialowska [2] has reported the pitting potential of aluminum in chloride solutions to be relatively independent of pH in the range 4–9. This was further advanced by Godard [3] to demonstrate that a deviation from neutrality, PH 7, on both acid and alkaline sides increases the pitting rate in neutral fresh waters.

Corrosion behaviour of aluminum alloys is significantly affected by the presence of particles in the matrix [4]. Particles that contain Cu and Mg tend to be anodic relative to the alloy matrix, while those that contain Fe and Mn behave in cathodic manner relative to the matrix [5]. Previous works [6–8] show that Mg₂Si particles tend to be anodic in relation to the matrix and can act as initiation sites for corrosion. Most often the Mg₂Si phase dissolves leaving behind a cavity, which acts as a nucleation site for pitting

TABLE 1: Al-Mg alloy chemical composition.

No. of cast	% Composition										Si/Mg ratio
	Fe	Si	Mn	Cu	Zn	Ti	Mg	Pb	Sn	Al	
As-received	0.296	0.446	0.073	0.013	0.016	0.020	0.34	0.007	0.009	98.78	1.312
Alloy 1	0.269	0.584	0.024	0.096	0.021	0.013	0.42	0.009	0.004	98.56	1.390
Alloy 2	0.276	0.572	0.023	0.071	0.018	0.012	0.91	0.008	0.005	98.56	0.629
Alloy 3	0.219	0.403	0.021	0.002	0.003	0.014	1.23	0.001	0.007	98.10	0.328
Alloy 4	0.253	0.530	0.088	0.012	0.017	0.015	1.52	0.006	0.005	97.59	0.349
Alloy 5	0.414	0.599	0.025	0.019	0.015	0.013	1.81	0.005	0.004	97.10	0.331
Alloy 6	0.319	0.771	0.024	0.037	0.019	0.013	2.02	0.001	0.006	96.79	0.382

[9, 10]. These observations were made during investigations that were carried out on commercial aluminum alloys having low Si/Mg molar ratios [11–14].

Crevice corrosion is a highly localized form of corrosion which occurs by infiltration of water into closely fitted surfaces. The presence of aggressive ions such as chloride often creates extensive localized attack [4]. Chloride ions are drawn into the crevice as metal dissolution occurs and the conditions inside the crevice become acidic. Metals like aluminum that depend on oxide films or passive layers for corrosion resistance are particularly susceptible to crevice corrosion. Attack from this phenomenon can be aggravated when combined with the presence of crystalline defect such as Mg_2Si precipitates. Possibility exists for reducing drastically the alloy susceptibility to corrosion if its microstructure is modified by appropriate heat treatment prior to usage. In this study, the chemical response of heat-treated aluminium-magnesium alloy in chloride and acidic media was investigated.

2. Experimental Procedure

2.1. Materials. Ingots of 6063 aluminum alloy and magnesium used for this study were obtained from the Nigerian Aluminum Extrusion Company (NIGALEX). Six different compositions of Al-Mg alloy with chemical compositions shown in Table 1 were produced. The Mg in the alloy was varied between 0.40 and 2.0 percent.

The aluminum and magnesium alloy ingots were charged together into a crucible pot, heated to molten state, and then poured into a metal mould. Sufficient time was allowed for the cooling of cast samples prior to removal. Each cast sample was divided into sets A (a_1 – a_1) and B (b_1 – b_1) with set A samples left untreated while set B samples were retrogressed and aged (RRA). The samples in solution were heat treated at 475°C and aged for 24 hrs (T6 condition) after which the samples were retrogressed at 200°C, held for forty minutes, and quenched in water. The RRA samples were then tempered at 120°C for 24 hrs and allowed to cool in air.

Standard electrochemical corrosion coupons (Figure 1) and microstructural test specimens were prepared from both sets A and B samples. For electrochemical and gravimetric tests, $\varnothing 10\text{ mm} \times 60\text{ mm}$ cylindrical rods and circular samples with dimensions of $\varnothing 14\text{ mm} \times 4\text{ mm}$ were used, respectively.



FIGURE 1: Standard electrochemical corrosion specimen.

2.2. Corrosion Campaigns. The corrosion simulations were carried out on the RRA specimens using electrochemical polarization and gravimetric techniques in three different media, namely, salt, ferric chloride, and acid. Immersion test simulates corrosion resistance of alloy in chloride environment containing 10% salt in water saturated with oxygen at room temperature. The ferric chloride test is used to study the responses of Al-Mg alloy to crevice corrosion in a medium consisting of 5.6 mL of $FeCl_3 \cdot 6H_2O$, 2 g of NaCl, and 5 g of concentrated HCl in 300 mL of water. EXCO test studies exfoliation corrosion of Al-Mg alloy in severe industrial or marine environments containing 5 g of NaCl, 5 g of KNO_3 , and 9 mL of HNO_3 in 300 mL of water. The Jenway 350-pH device was used to determine the pH of NaCl, $FeCl_3$, and EXCO solutions and the values are 6.80, 6.20, and 6.03, respectively.

In the gravimetric corrosion test, the initial weights of the test specimens were recorded before immersion in the test media while change in weights was taken every week using a Mettler Toledo weighing scale after the test pieces were rinsed in water and air-dried. The electrochemical corrosion setup (Figure 2(a)) is similar to electrolytic process in which the aluminum-magnesium alloy coupon and copper act as anode and cathode electrodes, respectively. The electrodes were partially immersed in the media in separate containers as the anode coupon was connected to the positive terminal of a 12 V SMF 5219 battery while the copper electrode was connected to its negative terminal and a YEM 2210 variable resistor (Rheostat) was incorporated into the circuit. The drop in current flowing through the system was recorded at 20-minute interval using YEM 2011 ammeter (Figure 2(b)).



FIGURE 2: Electrochemical setup. Electrical measuring devices

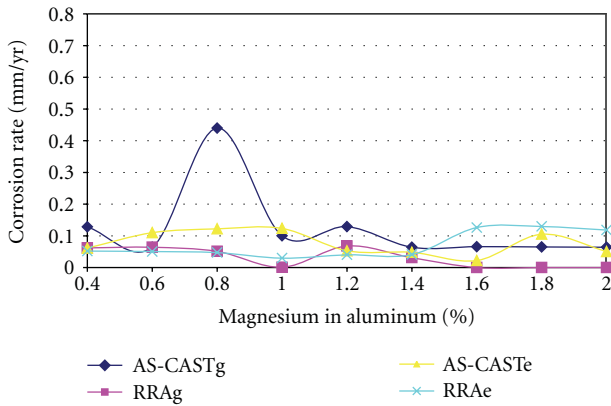


FIGURE 3: Effect of magnesium addition on the corrosion resistance of aluminum alloy in NaCl solution. Note: RRAg and AS-CASTg curves indicate the corrosion responses of heat-treated as-cast Al-Mg alloy specimens, respectively, in saline medium as evaluated through the gravimetric technique while RRAe and AS-CASTe curves illustrate the corrosion behaviors of heat-treated and as-cast Al-Mg alloy specimens, respectively, in saline environment as evaluated through the electrochemical polarization technique.

This electrochemical corrosion process lasted for six hours for each test piece studied.

2.3. Microstructure Analysis. Test specimens were prepared from the alloy samples and ground using emery grades of 40, 32, 10, and 8 in succession. The ground surfaces were polished using alumina paste to obtain a mirror-like surface. The polished test pieces were etched using dilute hydrochloric acid for 10s. The etched surfaces were carefully washed and dried. A digital Metallurgical Microscope at magnification of $\times 100$ was used to obtain the morphology of the sample matrix, while the photomicrographs produced from these test specimens are shown in Figures 6–11.

3. Results and Discussion

3.1. Corrosion Rate Measurements. The corrosion susceptibility of test specimens in the various media (NaCl, FeCl_3 , and EXCO solution) simulated was evaluated through both the gravimetric and electrochemical polarization techniques. This was carried out for the purposes of comparing which method can quickly provide information on the extent of

corrosion on one hand and reliability of the data obtained on the other. Gravimetric corrosion measurement technique basically bothered on weight-loss regime of test specimens. In applying this method, the weights of test specimens were obtained before and at the end of time specified for each monitoring phase. Before the next phase of monitoring, the test specimens were thoroughly washed with water, air-dried, and weighed. The weight-loss data (Appendix A.1) obtained was used to compute the corrosion rate making use of the following relation:

$$\text{corrosion rate (mm/yr)} = \frac{87.6W}{\rho At}, \quad (1)$$

where W is weight-loss (mg), ρ density of test specimen (gcm^{-3}), A area of test specimen (cm^2), and t exposure time (hr).

Electrochemical corrosion evaluation technique makes use of the electrical resistance property of test alloy by measuring the electrical polarization when current is impressed. In this study, standard test coupons of Al-Mg alloy of varying compositions were used as anode while copper was used as cathode. The set-up was partially immersed in each medium separately, and the drop in current flowing in through the system was recorded at 20-minutes interval. The corrosion rates as evaluated through (2) were presented in Appendix A.2.

$$\text{corrosion rate (mm/yr)} = \frac{3272W I_{\text{corr}}}{\rho A}, \quad (2)$$

where W is weight loss (g), ρ density of test specimen (gcm^{-3}), A exposure surface area of test specimen (cm^2), and I_{corr} current flowing in the test specimen (anode coupon).

The analyses of corrosion behaviour of test specimens by both gravimetric and electrochemical polarization show that the as-cast samples exhibited higher corrosion susceptibility than RRA specimens after immersion in NaCl solution (Figure 3). This trend subsists up to about 1.7% Mg addition in the aluminum alloy. The peak corrosion response of AS-CASTg: 0.13 mm/yr occurred at 0.4% and 1.2% Mg by gravimetric method while the electrochemical polarization technique recorded RRAe: 0.12 mm/yr at 0.91% and 1.81% Mg, respectively. In contrast to this observation, the RRA sample did not experience any appreciable corrosion within the period monitored (42 days) as computed using gravimetric technique. Through electrochemical polarization,

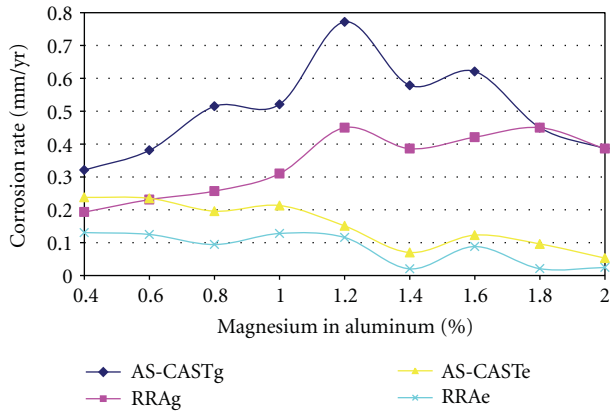


FIGURE 4: Effect of magnesium addition on the corrosion resistance of aluminum alloy in FeCl_3 solution. Note: RRAg and AS-CASTg curves indicate the corrosion responses of heat-treated and as-cast Al-Mg alloy specimens, respectively, in ferric chloride solution as evaluated through the gravimetric technique while RRAe and AS-CASTe curves illustrate the corrosion behaviors of heat-treated and as-cast Al-Mg alloy specimens, respectively, in ferric chloride solution as evaluated through the electrochemical polarization technique.

however, the RRA test coupons exhibited some level of corrosion at 0.13 mm/yr for 1.5–2.02% Mg. The corrosion responses of the RRA test specimens in saline environment which contrast those of as-cast specimens can be attributed to the extensive microstructure evolution that occurred during heat treatment. The grains are relieved, refined, and homogenized. However, at higher magnesium addition, 1.2–2.02%, the corresponding high volume of Mg_2Si precipitated adversely impacted the alloys corrosion resistance.

The curves in Figure 4 illustrate the corrosion behavior of test specimens in ferric chloride environment. With regard to gravimetric corrosion measurement, the as-cast specimens show increasing corrosion propensity, AS-CASTg: 0.321–0.772 mm/yr for 0.42–1.23% Mg addition. Afterwards, the corrosion rate (AS-CASTg) dropped to 0.579 mm/yr for 1.51% Mg while some level of passivity was displayed at 1.81% Mg having just 0.45 mm/yr corrosion rate.

The rather sporadic corrosion pattern of the as-cast specimens is due largely to their microstructure inhomogeneity. This is confirmed by the RRAg: 0.45 mm/yr maximum corrosion rate by the RRA specimens because their microstructures have been refined by heat treatment.

The corrosion responses of as-cast and RRA samples in ferric chloride solution using electrochemical polarization technique measurement are also presented in Figure 4. Both the as-cast and RRA test coupons demonstrated similar corrosion rate pattern. Corrosion was more prevalent, AS-CASTe: 0.151–0.238 mm/yr and RRAe: 0.094–0.131 mm/yr for as-cast and RRA specimens, respectively, at a relatively low magnesium addition, 0.42–1.23%. However, at a relatively higher magnesium addition, 1.51–2.02%, corrosion rates dropped significantly to 0.053–0.056 mm/yr for as-cast and 0.020–0.025 mm/yr for RRA test coupons. Given this scenario, the electrochemical polarization corrosion

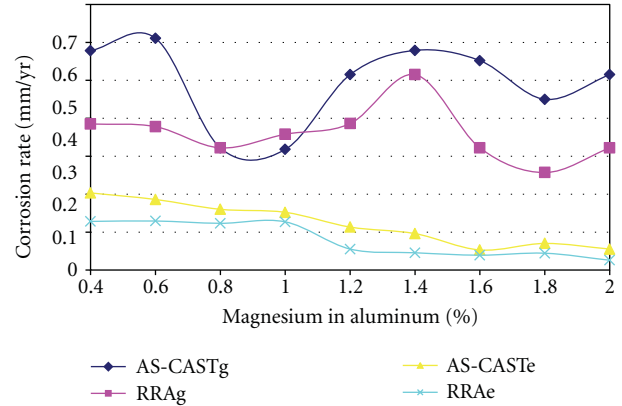


FIGURE 5: Effect of magnesium addition on the corrosion resistance of aluminum alloy in EXCO solution. Note: RRAg and AS-CASTg curves indicate the corrosion responses of heat-treated and as-cast Al-Mg alloy specimens, respectively, in EXCO solution as evaluated through the gravimetric technique while RRAe and AS-CASTe curves illustrate the corrosion behaviors of heat-treated and as-cast Al-Mg alloy specimens, respectively, in EXCO solution as evaluated through the electrochemical polarization technique.

measurement has proved that there is a strong correlation between the alloy structural integrity and corrosion susceptibility.

Figure 5 depicts the responses of test coupons to exfoliation corrosion under severe industrial and marine conditions (EXCO). Using the electrochemical polarization technique, the corrosion behaviors of both the as-cast and RRA samples are relatively low and nonuniform, AS-CASTe: 0.055–0.113 mm/yr and RRAe: 0.023–0.055 mm/yr for the as-cast and RRA specimens, respectively.

The inhomogeneity of microstructure must have been responsible for the wide range in corrosion rates exhibited by the as-cast specimens. Evaluation of the corrosion rates on the as-cast specimens through gravimetric method also shows that corrosion is nonuniform and the values are relatively high, AS-CASTg: 0.579 mm/yr and 0.322 mm/yr being the minimum. The RRA specimens, however, exhibited relatively uniform corrosion rates, RRAg: 0.257–0.386 mm/yr for the various magnesium additions. This is due to structural modifications that occurred pursuant to the heat treatment carried out on the alloy.

The microstructure of the as-cast specimens (Figure 6(a_i)) shows phases that are not evenly dispersed in the α -aluminum matrix, while there is strong clustering of Mg_2Si in certain area of the matrix. This is a potential polarization site for electrochemical attack on the alloy. The RRA specimens however have their Mg_2Si crystals fairly distributed within the matrix (Figure 6(b_i)).

Dipping of these specimens in NaCl solution gave rise to a substantial depletion of crystals of Mg_2Si and other intermetallics. This observation was more pronounced in the as-cast specimens (Figures 6(a_j), 6(b_j)) while the RRA alloy exhibited higher resistance to corrosion in NaCl solution than in FeCl_3 (Figures 6(b_j), 6(b_k)). In EXCO solution, the clustering arrangement of Mg_2Si crystals was preserved in

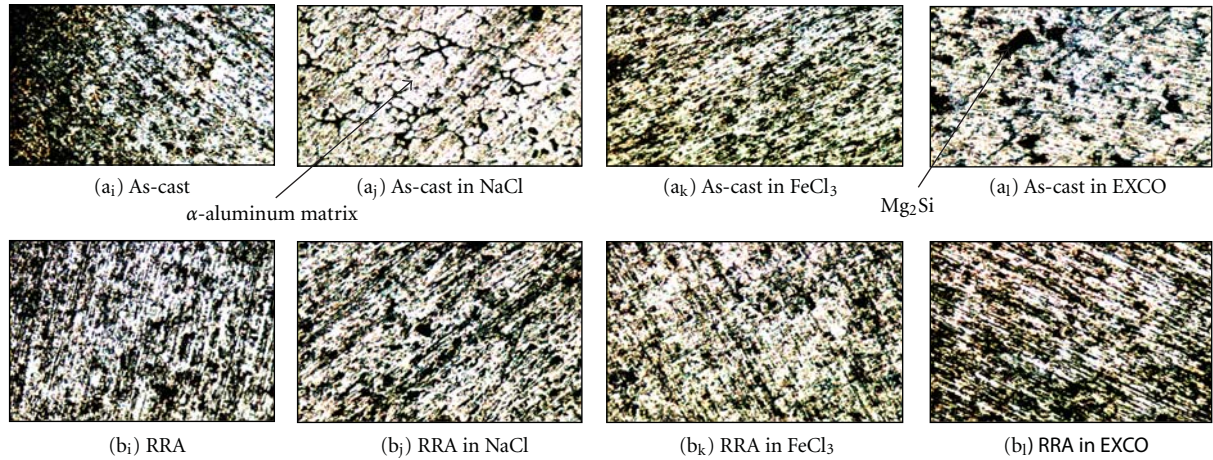


FIGURE 6: Micrographs of 0.42% Mg addition for untreated (a_i–a_l) and treated (b_i–b_l) specimens.

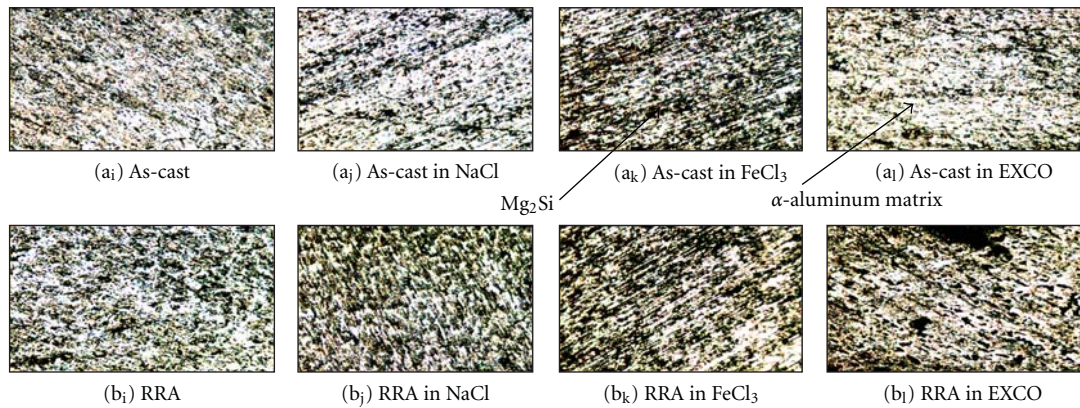


FIGURE 7: Micrographs of 0.91% Mg addition for untreated (a_i–a_l) and treated (b_i–b_l) specimens.

both alloy specimens (Figures 6(a_i), 6(b_i)) but the depletion of other intermetallics in the as-cast specimens was more than those of RRA alloy specimens. At 0.9% Mg addition, both alloy specimens have a fairly high volume fraction of Mg₂Si precipitates present in the matrices (Figures 7(a_i), 7(b_i)). On immersion in NaCl solution, the as-cast matrix is strongly attacked with significant erosion of the intermetallic phases while the RRA specimens show superior resistance to attack (Figures 7(a_k), 7(b_j)).

Both the precipitates and intermetallic phases, however, remain stable in FeCl₃ solution (Figures 7(a_k), 7(b_k)) while erosion of magnesium silicides was observed with the as-cast alloy in EXCO solution (Figures 7(a_l), 7(b_l)). Fine crystals of magnesium silicides made appearance at 1.2% Mg addition (Figures 8(a_i), 8(b_i)).

The crystals remain stable in the matrices of both alloys when dipped in NaCl solution (Figures 8(a_j), 8(b_j)). In FeCl₃ solution, however, severe erosion of the intermetallic crystals which is more pronounced in as-cast matrix was observed (Figures 8(a_k), 8(b_k)) while the response of both specimens was not quite apparent in EXCO solution (Figures 8(a_l), 8(b_l)). In Figure 9, the aluminum alloy specimens that contain

1.5% Mg have fine crystals induced in their structure (Figures 9(a_i), 9(b_i)). The intermetallic phase in the RRA alloy matrix was severely eroded in NaCl solution leaving the Mg₂Si crystals intact (Figures 9(a_j), 9(b_j)). However in FeCl₃, the corrosion behaviour of as-cast specimens is similar to that of RRA specimens, and Mg₂Si phase shows more resistance than other intermetallics (Figures 9(a_k), 9(b_k)). In Figures 9(a_l), 9(b_l) the as-cast alloy was strongly attacked in EXCO solution while substantial volume of Mg₂Si crystals induced in RRA specimens was retained.

In Figures 10(a_i), 10(b_i), higher volume fraction of intermetallics was observed in as-cast structure while clustering of Mg₂Si crystals occurred in RRA specimens. When immersed in NaCl solution, the as-cast matrix significantly corroded leaving only a few traces of the intermetallic crystals. The RRA suffered serious attack of its crystals than as-cast specimens in FeCl₃ solution with Mg₂Si crystals been washed off along with other intermetallics.

In EXCO solution, considerable corrosion occurred in the as-cast specimens thereby leaving the matrix almost bare (Figure 10(a_l)). The RRA alloy matrix, however, exhibited resistance to corrosion in EXCO solution, but, significant

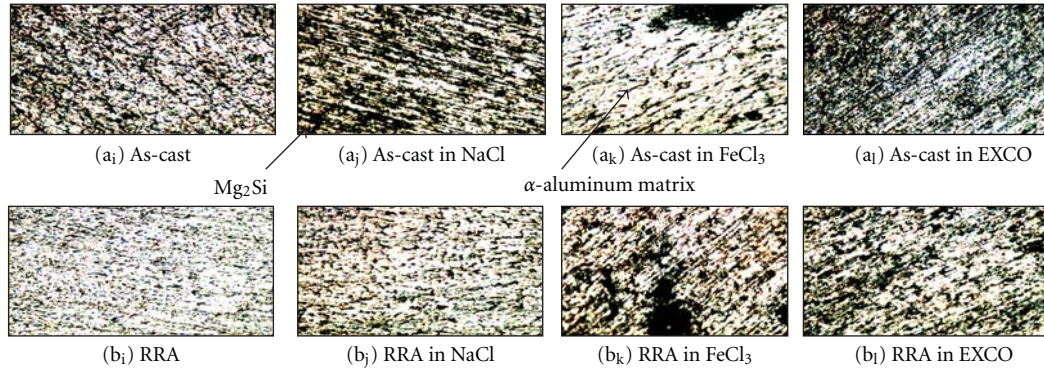


FIGURE 8: Micrographs of 1.23% Mg addition for untreated (a_i – a_l) and treated (b_i – b_l) specimens.

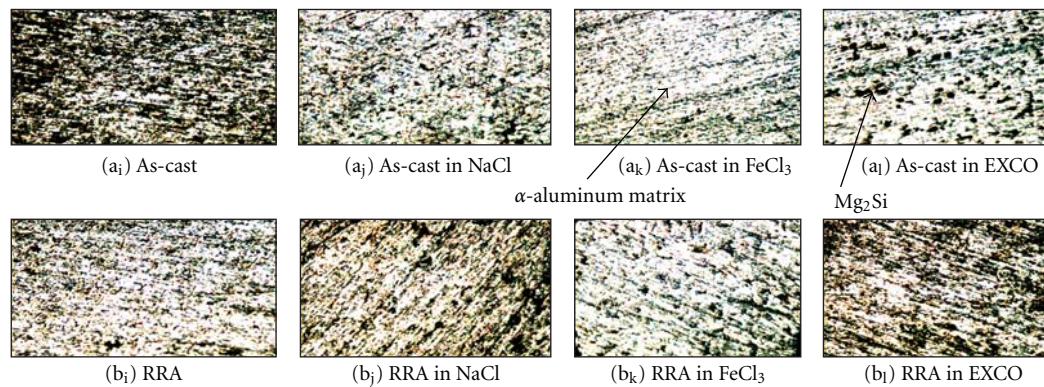


FIGURE 9: Micrographs of 1.51% Mg addition for untreated (a_i – a_l) and treated (b_i – b_l) specimens.

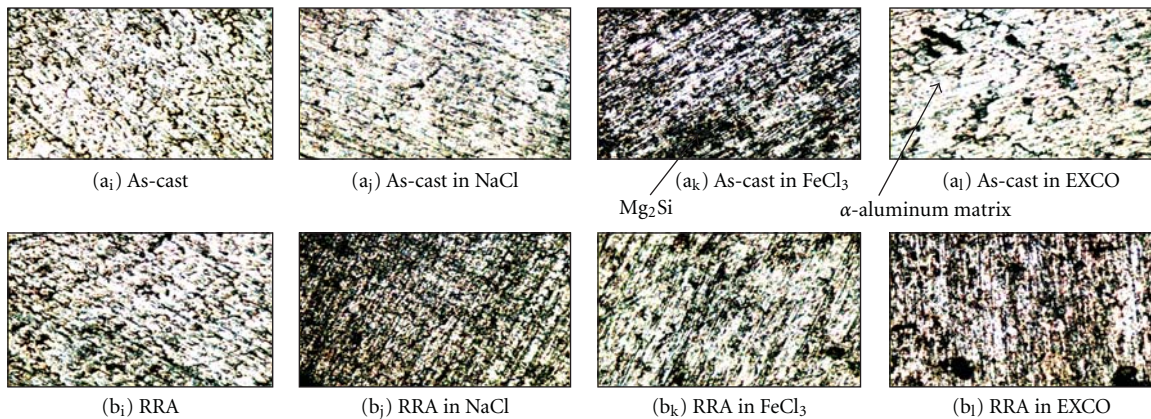


FIGURE 10: Micrographs of 1.81% Mg addition for untreated (a_i – a_l) and treated (b_i – b_l) specimens.

amount of Mg_2Si crystals was eroded leaving pit-like features in the matrix. (Figure 10(b_l)).

Figure 11 shows low volume fractions of Mg_2Si crystals in the RRA specimens at 2.0% Mg addition (Figure 11(b_l)). Strong erosion of the Mg_2Si crystals occurred in the as-cast matrix when dipped in NaCl solution but the other intermetallics were resistant in this medium (Figures 11(a_j), 11(b_j)). In $FeCl_3$ solution, the intermetallics show resistance to attack in both as-cast and RRA matrices but suffered the loss of crystals of α -aluminum to corrosion (Figures 11(a_k),

11(b_k)). Immersion of the alloy specimens in EXCO solution resulted in severe attack on the crystals of RRA matrix while the intermetallics in as-cast show superior resistance to the crystals of α -aluminum in this medium (Figures 11(a_l), 11(b_l)).

4. Conclusion

Corrosion responses of the as-cast and RRA alloy specimens differ significantly based on the microstructure induced in

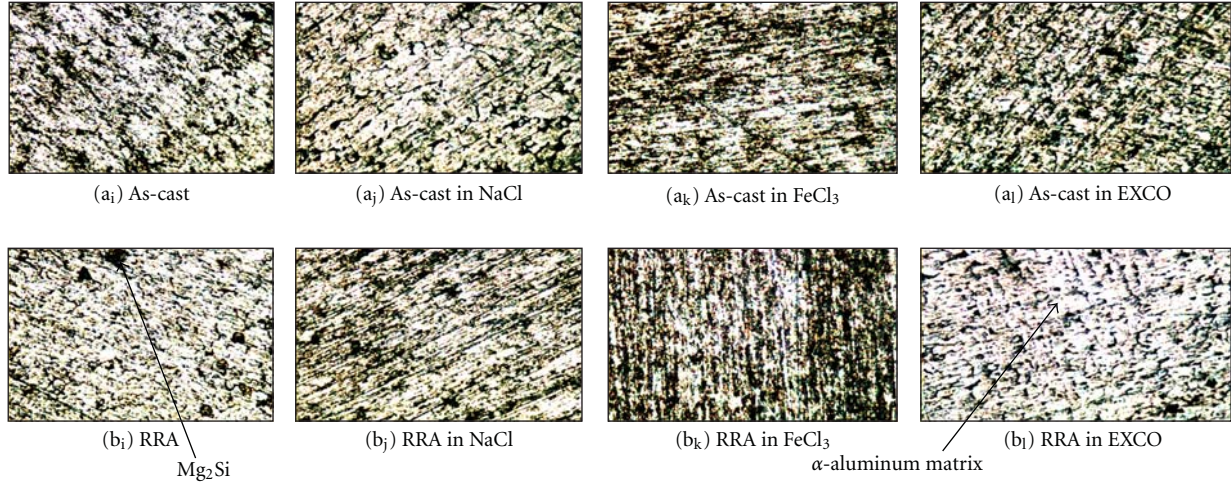


FIGURE 11: Micrographs of 2.02% Mg addition for untreated (a₁–a₄) and treated (b₁–b₄) specimens.

TABLE 2: Gravimetric corrosion rate (mm/yr) for the 0.42% Mg specimen.

Days	NaCl solution		FeCl ₃		EXCO solution	
	As-cast	RRA	As-cast	RRA	As-cast	RRA
0	0	0	0	0	0	0
7	0	0	0.385	0	0.381	0.385
14	0	0	0.385	0.193	0.578	0.193
21	0	0	0.385	0.128	0.514	0.257
28	0.096	0	0.289	0.193	0.578	0.385
35	0.077	0	0.308	0.231	0.617	0.385
42	0.128	0.064	0.321	0.193	0.578	0.385

TABLE 4: Gravimetric corrosion rate (mm/yr) for the 1.23% Mg specimen.

Days	NaCl solution		FeCl ₃		EXCO Solution	
	As-cast	RRA	As-cast	RRA	As-cast	RRA
0	0.000	0.000	0.000	0.000	0.000	0.000
7	0.000	0.000	1.542	0.771	0.000	0.385
14	0.000	0.000	1.156	0.771	0.385	0.385
21	0.128	0.000	1.028	0.514	0.514	0.514
28	0.096	0.000	0.963	0.482	0.482	0.482
35	0.154	0.000	0.848	0.463	0.540	0.463
42	0.129	0.064	0.772	0.450	0.515	0.386

TABLE 3: Gravimetric corrosion rate (mm/yr) for the 0.91% Mg specimen.

Days	NaCl solution		FeCl ₃		EXCO solution	
	As-cast	RRA	As-cast	RRA	As-cast	RRA
0	0.000	0.000	0.000	0.000	0.000	0.000
1200	0.000	0.000	0.771	0.000	0.000	0.000
2400	0.000	0.000	0.771	0.193	0.193	0.193
3600	0.000	0.000	0.642	0.257	0.128	0.257
4800	0.000	0.000	0.578	0.289	0.193	0.385
6000	0.077	0.000	0.54	0.231	0.231	0.308
7200	0.064	0.000	0.515	0.257	0.322	0.322

TABLE 5: Gravimetric corrosion rate (mm/yr) for the 1.51% Mg specimen.

Days	NaCl solution		FeCl ₃		EXCO solution	
	As-cast	RRA	As-cast	RRA	As-cast	RRA
0	0.000	0.000	0.000	0.000	0.000	0.000
7	0.000	0.000	1.156	1.156	0.771	0.000
14	0.000	0.000	0.964	0.578	0.578	0.385
21	0.000	0.000	0.899	0.385	0.642	0.514
28	0.000	0.000	0.771	0.385	0.578	0.482
35	0.077	0.000	0.694	0.385	0.54	0.463
42	0.064	0.000	0.579	0.386	0.579	0.515

them. The precipitated Mg₂Si crystals are anodic relative to the alloy matrix which easily dissolved under attack by chemical. This phenomenon occurred at relatively higher magnesium content in the range of 1.2–2.0%. Within this range, the volume fraction of Mg₂Si precipitates in the alloy matrix is rather substantial thereby accentuating susceptibility to corrosion.

Heat treatment process employed in this study serves the purpose of modifying the alloy microstructure such that

inducement of soluble precipitates is suppressed in preference to strongly refractory intermetallics. This behavior was observed in the RRA specimens compared with as-cast alloy specimens thereby validating established significant role of the presence of intermetallics in an alloy matrix with respect to corrosion mitigation [15]. Intermetallics are complex compounds which do not easily dissolve thereby becoming cathodic relative to the alloy matrix. Therefore, the extent of corrosion suffered by an alloy depends on which phase

TABLE 6: Gravimetric corrosion rate (mm/yr) For the 1.81% Mg specimen.

Days	NaCl solution		FeCl ₃		EXCO solution	
	As-cast	RRA	As-cast	RRA	As-cast	RRA
0	0.000	0.000	0.000	0.000	0.000	0.000
7	0.000	0.000	0.771	0.771	0.771	0.385
14	0.000	0.000	0.771	0.771	0.771	0.385
21	0.000	0.000	0.642	0.514	0.514	0.385
28	0.000	0.000	0.578	0.578	0.482	0.289
35	0.000	0.000	0.54	0.54	0.463	0.231
42	0.000	0.000	0.45	0.45	0.45	0.257

TABLE 7: Gravimetric corrosion rate (mm/yr) for the 2.02% Mg specimen.

Days	NaCl solution		FeCl ₃		EXCO Solution	
	As-cast	RRA	As-cast	RRA	As-cast	RRA
0	0.000	0.000	0.000	0.000	0.000	0.000
7	0.000	0.000	0.771	0.771	0.385	0.000
14	0.000	0.000	0.385	0.771	0.578	0.193
21	0.000	0.000	0.514	0.514	0.514	0.578
28	0.000	0.000	0.482	0.482	0.482	0.514
35	0.077	0.000	0.463	0.385	0.54	0.308
42	0.064	0.064	0.386	0.386	0.515	0.322

TABLE 8: Gravimetric corrosion rate (mm/yr) for the control specimen.

Days	NaCl solution		FeCl ₃		EXCO solution	
	As-cast	RRA	As-cast	RRA	As-cast	RRA
0	0	0	0	0	0	0
7	0	0	0.771	0.771	0.771	0.384
14	0	0	0.771	0.771	0.771	0.385
21	0.129	0	0.642	0.514	0.642	0.385
28	0.096	0	0.578	0.482	0.674	0.289
35	0.154	0.077	0.54	0.385	0.694	0.308
42	0.193	0.192	0.45	0.386	0.643	0.322

TABLE 9: Electrochemical corrosion rate For the 0.42% Mg specimen.

T (sec)	NaCl solution		FeCl ₃		EXCO solution	
	As-cast	RRA	As-cast	RRA	As-cast	RRA
0	0.0000	0.0000	0.0000	0.0000	0.0000	0.0000
1200	0.0117	0.0123	0.0425	0.0394	0.0370	0.0238
2400	0.0224	0.0238	0.0850	0.0468	0.0727	0.0460
3600	0.0324	0.0338	0.1254	0.0690	0.1072	0.0666
4800	0.0425	0.0443	0.1643	0.0904	0.1429	0.0871
6000	0.0511	0.0544	0.1982	0.1109	0.1725	0.1089
7200	0.0614	0.0520	0.2378	0.1307	0.2033	0.1282

TABLE 10: Electrochemical corrosion rate for the 0.91% Mg specimen.

T (sec)	NaCl solution		FeCl ₃		EXCO solution	
	As-cast	RRA	As-cast	RRA	As-cast	RRA
0	0.0000	0.0000	0.0000	0.0000	0.0000	0.0000
1200	0.0242	0.0061	0.0363	0.0176	0.0308	0.0238
2400	0.0468	0.0117	0.0702	0.0345	0.0605	0.04600
3600	0.0678	0.0167	0.1035	0.0499	0.0877	0.0653
4800	0.0871	0.0214	0.1355	0.0653	0.1129	0.0855
6000	0.1027	0.0252	0.1663	0.0785	0.1360	0.01048
7200	0.1233	0.0296	0.1959	0.0943	0.1601	0.1232

TABLE 11: Electrochemical corrosion rate for the 1.23% Mg specimen.

T (sec)	NaCl solution		FeCl ₃		EXCO solution	
	As-cast	RRA	As-cast	RRA	As-cast	RRA
0	0	0	0	0	0	0
1200	0.0115	0.0057	0.0298	0.0234	0.0234	0.0119
2400	0.021	0.0105	0.0565	0.0435	0.0435	0.0222
3600	0.0302	0.0148	0.0816	0.0628	0.0616	0.0308
4800	0.0386	0.0185	0.1068	0.0805	0.0805	0.0394
6000	0.0750	0.0216	0.1283	0.0985	0.0965	0.0482
7200	0.0530	0.0401	0.1509	0.1158	0.1133	0.0554

TABLE 12: Electrochemical corrosion rate for the 1.51% Mg specimen.

T (sec)	NaCl solution		FeCl ₃		EXCO solution	
	As-cast	RRA	As-cast	RRA	As-cast	RRA
0	0	0	0	0	0	0
1200	0.0056	0.0287	0.0169	0.0055	0.0226	0.0115
2400	0.0103	0.0524	0.0308	0.0099	0.0411	0.021
3600	0.0142	0.0739	0.0425	0.0136	0.0579	0.0283
4800	0.0173	0.0924	0.053	0.0165	0.0707	0.0337
6000	0.0195	0.1103	0.0616	0.018	0.0842	0.04
7200	0.0222	0.1263	0.0702	0.0203	0.0961	0.0456

TABLE 13: Electrochemical corrosion rate for the 1.81% Mg specimen.

T (sec)	NaCl solution		FeCl ₃		EXCO solution	
	As-cast	RRA	As-cast	RRA	As-cast	RRA
0	0	0	0	0	0	0
1200	0.0172	0.0282	0.023	0.0056	0.0172	0.0113
2400	0.032	0.0524	0.0411	0.0101	0.0308	0.0201
3600	0.0434	0.0739	0.0579	0.0136	0.0425	0.0277
4800	0.0517	0.0944	0.0723	0.0165	0.053	0.0345
6000	0.0585	0.1129	0.0842	0.0185	0.0631	0.04
7200	0.105	0.1294	0.0961	0.0209	0.0702	0.0444

TABLE 14: Electrochemical corrosion rate for the 2.02% Mg specimen.

T (sec)	NaCl solution		FeCl ₃		EXCO solution	
	As-cast	RRA	As-cast	RRA	As-cast	RRA
0	0	0	0	0	0	0
1200	0.0117	0.0242	0.0119	0.0058	0.0117	0.0058
2400	0.0222	0.046	0.0226	0.0107	0.0222	0.0107
3600	0.034	0.0653	0.0314	0.0151	0.032	0.0148
4800	0.0386	0.0838	0.0402	0.0189	0.0419	0.0189
6000	0.0452	0.1027	0.0472	0.0216	0.0493	0.0226
7200	0.0505	0.1183	0.053	0.0246	0.0554	0.0259

TABLE 15: Electrochemical corrosion rate for the control specimen.

T (sec)	NaCl solution		FeCl ₃		EXCO solution	
	As-cast	RRA	As-cast	RRA	As-cast	RRA
0	0	0	0	0	0	0
1200	0.0119	0.0242	0.0119	0.0111	0.0176	0.0113
2400	0.0226	0.0468	0.023	0.021	0.0333	0.0214
3600	0.0326	0.069	0.0326	0.0302	0.049	0.0308
4800	0.0419	0.0904	0.0427	0.0386	0.0628	0.0402
6000	0.0513	0.1109	0.0523	0.047	0.0785	0.0493
7200	0.0604	0.1331	0.0616	0.0554	0.0924	0.0567

predominates, either soluble or indissoluble precipitates. The electrochemical corrosion evaluation provided a complimentary result when compared to the gravimetric method. However, the latter often takes months before any visible corrosion attack could be detected while the former takes just few minutes. This can be a crucial factor for determining the best approach to adopt in corrosion assessment where time is a constraint.

Appendices

A. Gravimetric and Electrochemical Corrosion Rates Data for Test Specimens in Various Environments

A.1. Gravimetric Corrosion Rates Data for Test Specimens in Various Media (Exposure Time: 42 Days). For more details, please see Tables 2, 3, 4, 5, 6, 7, and 8.

A.2. Electrochemical Corrosion Rates Data for Test Specimens in Various Media (Exposure Time: 2 Hours). For more details, please see Tables 9, 10, 11, 12, 13, 14, and 15.

References

- [1] K. Hashimoto, "2002 W.R. Whitney award lecture: in pursuit of new corrosion-resistant alloys," *Corrosion*, vol. 58, no. 9, pp. 715–722, 2002.
- [2] Z. Sziklarska-Smialowska, *Pitting Corrosion of Metals*, National Association of Corrosion Engineers, Houston, Tex, USA, 1986.
- [3] H. G. Godard, *The Corrosion of Light Metals*, John Wiley & Sons, New York, NY, USA, 1967.
- [4] L. Garrigues, N. Pebere, and F. Dabosi, "An investigation of the corrosion inhibition of pure aluminum in neutral and acidic chloride solutions," *Electrochimica Acta*, vol. 41, no. 7-8, pp. 1209–1215, 1996.
- [5] R. P. Wei, C. M. Liao, and M. Gao, "A transmission electron microscopy study of constituent-particle-induced corrosion in 7075-T6 and 2024-T3 aluminum alloys," *Metallurgical and Materials Transactions A*, vol. 29, no. 4, pp. 1153–1160, 1998.
- [6] K. A. Yasakau, M. L. Zheludkevich, S. V. Lamaka, and M. G. S. Ferreira, "Role of intermetallic phases in localized corrosion of AA5083," *Electrochimica Acta*, vol. 52, no. 27, pp. 7651–7659, 2007.
- [7] J. H. W. De Wit, "Local potential measurements with the SKPFM on aluminium alloys," *Electrochimica Acta*, vol. 49, no. 17-18, pp. 2841–2850, 2004.
- [8] F. Andreatta, H. Terryn, and J. H. W. de Wit, "Effect of solution heat treatment on galvanic coupling between intermetallics and matrix in AA7075-T6," *Corrosion Science*, vol. 45, no. 8, pp. 1733–1746, 2003.
- [9] N. Birbilis and R. G. Buchheit, "Electrochemical characteristics of intermetallic phases in aluminum alloys : an experimental survey and discussion," *Journal of the Electrochemical Society*, vol. 152, no. 4, pp. B140–B151, 2005.
- [10] J. Wloka, G. Bürklin, and S. Virtanen, "Influence of second phase particles on initial electrochemical properties of AA7010-T76," *Electrochimica Acta*, vol. 53, no. 4, pp. 2055–2059, 2007.
- [11] A. Pardo, M. C. Merino, S. Merino, M. D. López, F. Viejo, and M. Carboneras, "Influence of SiCp content and matrix composition on corrosion resistance in cast aluminium matrix composites in salt fog," *Corrosion Engineering Science and Technology*, vol. 39, no. 1, pp. 82–88, 2004.
- [12] S. Ren, X. He, X. Qu, I. S. Humail, and Y. Li, "Effect of Si addition to Al-8Mg alloy on the microstructure and thermophysical properties of SiCp/Al composites prepared by pressureless infiltration," *Materials Science and Engineering B*, vol. 138, no. 3, pp. 263–270, 2007.
- [13] A. Pardo, M. C. Merino, R. Arrabal, S. Merino, F. Viejo, and A. E. Coy, "Effect of la surface treatments on corrosion resistance of A3xx.x/SiC p composites in salt fog," *Applied Surface Science*, vol. 252, no. 8, pp. 2794–2805, 2006.
- [14] P. P. Trzaskoma and E. McCafferty, "Corrosion behavior of SiC/Al metal matrix composites," *Journal of the Electrochemical Society*, vol. 130, no. 9, pp. 1804–1809, 1983.
- [15] J. Datta, C. Bhattacharya, and S. Bandyopadhyay, "Influence of Cl-, Br-, NO₃ and SO₂ Ions on the Corrosion Behaviour of 6061 Aluminium Alloy," *Indian Academy of Sciences, Bulletin of Materials Science*, vol. 28, no. 3, pp. 253–258, 2005.